LENS-COUPLED X-RAY IMAGING SYSTEMS

by

Helen Xiang Fan

A Dissertation Submitted to the Faculty of the

COLLEGE OF OPTICAL SCIENCES

In Partial Fulfillment of the Requirements
For the Degree of

DOCTOR OF PHILOSOPHY

In the Graduate College

THE UNIVERSITY OF ARIZONA

2015

THE UNIVERSITY OF ARIZONA
GRADUATE COLLEGE

As members of the Dissertation Committee, we certify that we have read the dissertation prepared by Helen Xiang Fan entitled Lens-coupled X-Ray Imaging Systems and recommend that it be accepted as fulfilling the dissertation requirement for the Degree of Doctor of Philosophy.

Date: 11 May 2015

Dr. Harrison H. Barrett

Date: 11 May 2015

Dr. Lars R. Furenlid

Date: 11 May 2015

Dr. Eric Clarkson

Final approval and acceptance of this dissertation is contingent upon the candidate's submission of the final copies of the dissertation to the Graduate College.

I hereby certify that I have read this dissertation prepared under my direction and recommend that it be accepted as fulfilling the dissertation requirement.

Date: 11 May 2015

Dissertation Director: Dr. Harrison H. Barrett

STATEMENT BY AUTHOR

This dissertation has been submitted in partial fulfillment of requirements for an advanced degree at the University of Arizona and is deposited in the University Library to be made available to borrowers under rules of the Library.

Brief quotations from this dissertation are allowable without special permission, provided that an accurate acknowledgment of the source is made. Requests for permission for extended quotation from or reproduction of this manuscript in whole or in part may be granted by the head of the major department or the Dean of the Graduate College when in his or her judgment the proposed use of the material is in the interests of scholarship. In all other instances, however, permission must be obtained from the author.

SIGNED: Helen Xiang Fan

ACKNOWLEDGEMENTS

First I would like to thank my husband, Ryan, for his patience and encouragements throughout my time in graduate school. Without his support, this would have never been possible.

I would like to thank my advisor, Harry Barrett, for providing me with an opportunity to work on a very interesting project. This dissertation would not have been possible without his guidance and his tremendous knowledge in the field. I would like to express my gratitude to Lars Furenlid, for his help with many hardware challenges and providing much professional advice as well. I would like to thank Eric Clarkson for patiently answering my numerous math questions.

I would also like to thank Mike Arthur for showing me how to use the tools in the machine shop and Hans Roehrig allowing me to use his x-ray lab and equipment for all of my experiments.

I would also like to express my sincere thanks for all of my lab mates, Vaibhav Bora, Cecile Carlson, Esen Salcin, Joseph Ortiz, Jin Park, and Joy Ding. They have provided an incredible friendly environment and many interesting conversations throughout my time here. I would also like to express my gratitude to Merry Warner and Liz Hague for helping me place lots of orders and giving a lot of support throughout the years. I would like to thank Christy Barber for putting up with me while we were office mates.

I am grateful for the funding I have received. I have received support from Biomedical Imaging and Spectroscopy (BMIS) program, Achievement Reward for College Scientists (ARCS) scholarship, and NIH grants T32 EB000809, P41 EB002035, and R01 EB000803.

DEDICATION

To my father and my husband.

TABLE OF CONTENTS

TABLE OF CONTENTS – *Continued*

TABLE OF CONTENTS – *Continued*

LIST OF FIGURES

LIST OF FIGURES – *Continued*

LIST OF FIGURES – *Continued*

LIST OF FIGURES – *Continued*

LIST OF FIGURES – *Continued*

LIST OF FIGURES – *Continued*

LIST OF TABLES

ABSTRACT

Digital radiography systems are important diagnostic tools for modern medicine. The images are produced when x-ray sensitive materials are coupled directly onto the sensing element of the detector panels. As a result, the size of the detector panels is the same size as the x-ray image. An alternative to the modern DR system is to image the x-ray phosphor screen with a lens onto a digital camera. Potential advantages of this approach include rapid readout, flexible magnification and field of view depending on applications.

We have evaluated lens-coupled DR systems for the task of signal detection by analyzing the covariance matrix of the images for three cases, using a perfect detector and lens, when images are affected by blurring due to the lens and screen, and for a signal embedded in a complex random background. We compared the performance of lens-coupled DR systems using three types of digital cameras. These include a scientific CCD, a scientific CMOS, and a prosumer DSLR camera.

We found that both the prosumer DSLR and the scientific CMOS have lower noise than the scientific CCD camera by looking at their noise power spectrum. We have built two portable low-cost DR systems, which were used in the field in Nepal and Utah. We have also constructed a lens-coupled CT system, which included a calibration routine and an iterative reconstruction algorithm written in CUDA.

CHAPTER 1

INTRODUCTION

Digital radiography systems are important diagnostic tools for modern medicine. They can be divided into two general groups using two different readout processes. The first is based on storage phosphors where the x-ray image is first stored in an x-ray converter in a cassette form which later requires a separate optical readout process to record the image. Typically, this separate readout process requires human intervention to transfer the storage phosphor cassette from the patient to the laser-scanning station. Systems that acquire images using this method are commonly known as Computed Radiography (CR) systems, and they have been commercially available for almost two decades. They are used for various applications and produce images with excellent image quality; however, they are not the focus of this dissertation. For more information, see the review articles by Rowlands (Rowlands, 2002) and Kato (Kato, 1994), and the American Association of Physicists in Medicine (AAPM) Report No. 93. (AAPM, 2006).

In the second group of radiography systems, the x-ray image is detected and read out by the same device without any human intervention. These are commonly known as Digital Radiography (DR) systems and are the focus of this chapter.

1.1 Digital Radiography (DR) detectors

Modern x-ray digital radiography (DR) detectors were made possible by the considerable investment into developing active-matrix liquid-crystal flat-panel display (AMLCD) found in modern monitors and flat-screen TVs. This technology created a way of manufacturing large-area integrated circuits called active-matrix arrays

that enabled semiconductors, such as amorphous silicon, to be deposited across a large area on glass substrates. The medical device community took advantage of this technology, which formed the basis of digital radiography detectors. Sometimes called flat-panel detectors (FPD), they are built by coupling x-ray-sensitive materials with the active-matrix arrays that are created to store and read out the products of the x-ray interactions with sensitive materials, resulting in an image. There are two general approaches to creating an x-ray detector, direct and indirect. We will give a brief overview of the two approaches in the following section.

1.1.1 Direct approach

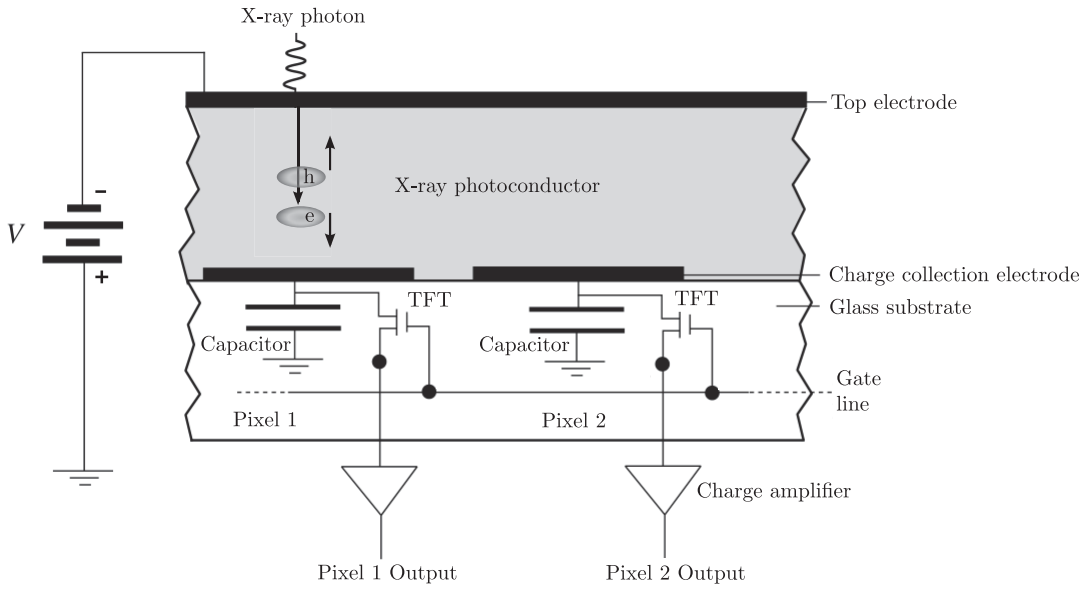

Figure 1.1: A cross-section of a photoconductor pixel[1]. The charges are first generated by an incident x-ray photon, then collected onto a capacitor. The collected charges will pass through a charge amplifier during readout when the gate line turns on the thin-film transistors (TFT) at each pixel.

[1]Reprinted from: *Curr. Appl. Phys.*, **6**, Kasap, S. O., M. Zahangir Kabir, and J. A. Rowlands, Recent advances in X-ray photoconductors for direct conversion X-ray image detectors, pp. 288-292, Copyright(2006), with permission from Elsevier.

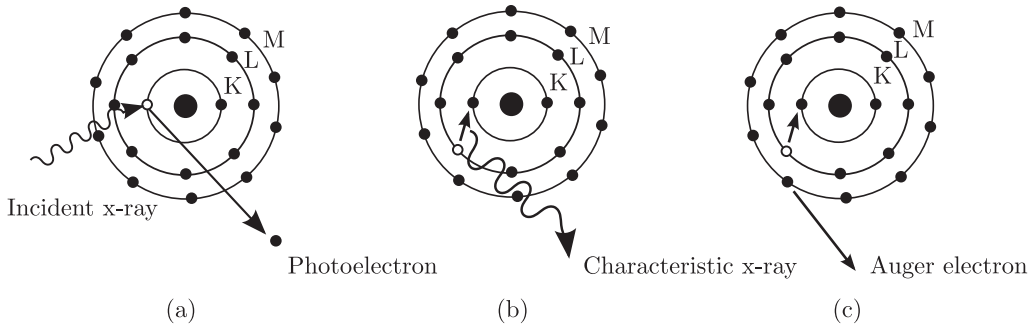

Figure 1.2: (a) A photoelectron is ejected from the K-shell by the absorption of an incident x-ray photon. (b) A characteristic x-ray photon is emitted when an electron from the L-shell is dropped down to fill the vacancy left by the photoelectron. (c) An Auger electron is ejected from its orbital shell when the energy released by the transitioning electron is absorbed (Kieranmaher, 2015).

The terms direct and indirect refer to the outputs of initial x-ray interactions with the detection material rather than the design of the active-matrix arrays. In the direct approach, an x-ray interaction with a photoconductor produces electron-hole pairs at the interaction site. The detector signal is produced directly by collecting the electrons when an electric field is applied to the photoconductor, shown in Fig 1.1. The x-ray sensitivity is the photoconductor's ability to convert incident x-rays into collectible charges, and it is affected by several properties.

The first property is the quantum efficiency of the photoconductor material. The quantum efficiency refers to the absorbed fraction of incident radiation that is useful in creating electron-hole pairs. The quantum efficiency for an x-ray photon with energy $\mathcal{E}$ is given by $\eta_Q = 1 - exp[-\alpha(\mathcal{E}, Z, \rho)T]$, where T is the material's thickness, α is the linear attenuation coefficient of the material and is a function of the x-ray energy ($\mathcal{E}$), the average atomic number of the material (Z), and the density of the material (ρ). High quantum efficiency can be achieved by increasing the material's thickness, choosing a material with high Z value, or density.

A second property that affects the photoconductor's x-ray sensitivity is the generation of electron-hole pairs. The predominant interaction of diagnostic x rays with a photoconductor medium is via the photoelectric effect, where the energy of an x-

ray photon is transferred to the photoconductor's atom, and an electron is liberated from the atom's inner shell, shown in Fig. 1.2a. The liberated electron is also called a photoelectron. This event leaves behind a vacancy at the atom's inner shell, and is quickly filled by an electron from an outer orbital shell, which is in turn filled by an electron transitioning from a more distant shell. This process of electrons cascading from one shell to another can release energies in the form of characteristic x-rays each with energy equal to the difference between the two transition shells, shown in Fig. 1.2b. This cascading process can also release energies to eject Auger electrons, where the energy released by a cascading electron is used to eject another electron from its orbital shell, shown in Fig. 1.2c. While the electrons cascade down to fill the vacancy created by the first photoelectron, the vacancy moves up through the outer shells of the atom to the photoconductor's valence band. This vacancy is also referred to as a hole. The characteristic x-rays released by the cascading electrons can also be absorbed within the photoconductor's medium to create more electron-hole pairs and more characteristic x-rays, albeit with electrons at higher orbital shells. This process will continue until all of the radiative energies have been absorbed. The Auger electrons and the original photoelectron can also travel in the photoconductor's medium to create more electron-hole pairs by ionization until they lose all of their energies and come to a stop. As a result, many electron-hole pairs are created by the absorption of one x-ray photon (Bushberg et al., 2002; Hajdok et al., 2006). The total charge generated from one absorbed photon is $e\,\mathcal{E}/W_{\pm}$, where e is the charge of an electron, $\mathcal{E}$ is the energy of the incident x-ray photon, and $W_{\pm}$, is the energy required to create one electron-hole pair. $W_{\pm}$ depends on the band-gap energy and in some cases such as a-Se, on the applied electric field (Kasap et al., 2006).

Another important property of the photoconductor is the mean distance traveled by a charge carrier. In order to read out an image, the liberated charge carriers must be collected onto an external storage element before they are lost within the photoconductor material. These charge carriers can be lost either by recombination

of electrons with holes or they can be trapped at an unoccupied energy level between the conduction and valence band. Electrodes that are placed on opposite ends of the material's surface create an electric field, which causes the free electrons and holes to drift in the opposite directions. The mean distance traveled by a charge carrier before it is trapped or lost is called Schubweg. This distance is given by $S = \mu\tau E$, which depends on the carrier's drift mobility (μ), lifetime (τ), and the applied electric field (E). It is important that this distance is much longer than the thickness of the photoconductor material. For example, at an applied field of 10 Vμm^{-1}, this distance is typically between 0.3 to 3 mm for an electron, and 6.5 to 65 mm for a hole in amorphous Selenium (a-Se). The typical thickness of a-Se used for diagnostic imaging is between 0.2 to 1 mm (Rowlands and Yorkston, 2000).

Problems that can affect x-ray detectors made with photoconductors are image lag and ghosting produced within the photoconductor material. Image lag refers to the carried-over image produced from one exposure to the next. This is caused by the trapped charges from one exposure becoming detrapped and read out in the subsequent image. Ghosting refers to the trapped charges acting as recombination centers for the generated charges. These recombination centers effectively reduce the lifetime of the charge carriers and the x-ray sensitivity. Both image lag and ghosting can be minimized by making sure the carrier's mean drift distance is larger than the material's thickness.

Various x-ray photoconductor materials are used in commercial products, such as CdTe, CdZnTe, CdSe, PbO, PbI_2, and HgI_2. However these product applications typically involve small areas, less than 10 cm^2. Large area panels that are over 30 cm $\times$ 30 cm or greater, are typically made using amorphous Selenium (a-Se). Due to its use as a photoreceptor for xerography (Mort, 1989), and it ability to be deposited over a large area, a-Se is one of the most common photoconductor used in direct commercial digital radiography systems.

The biggest disadvantage of using a-Se is that it requires an internal field of approximately 10 Vμm^{-1} to activate. So for a 500 μm layer, the activation require-

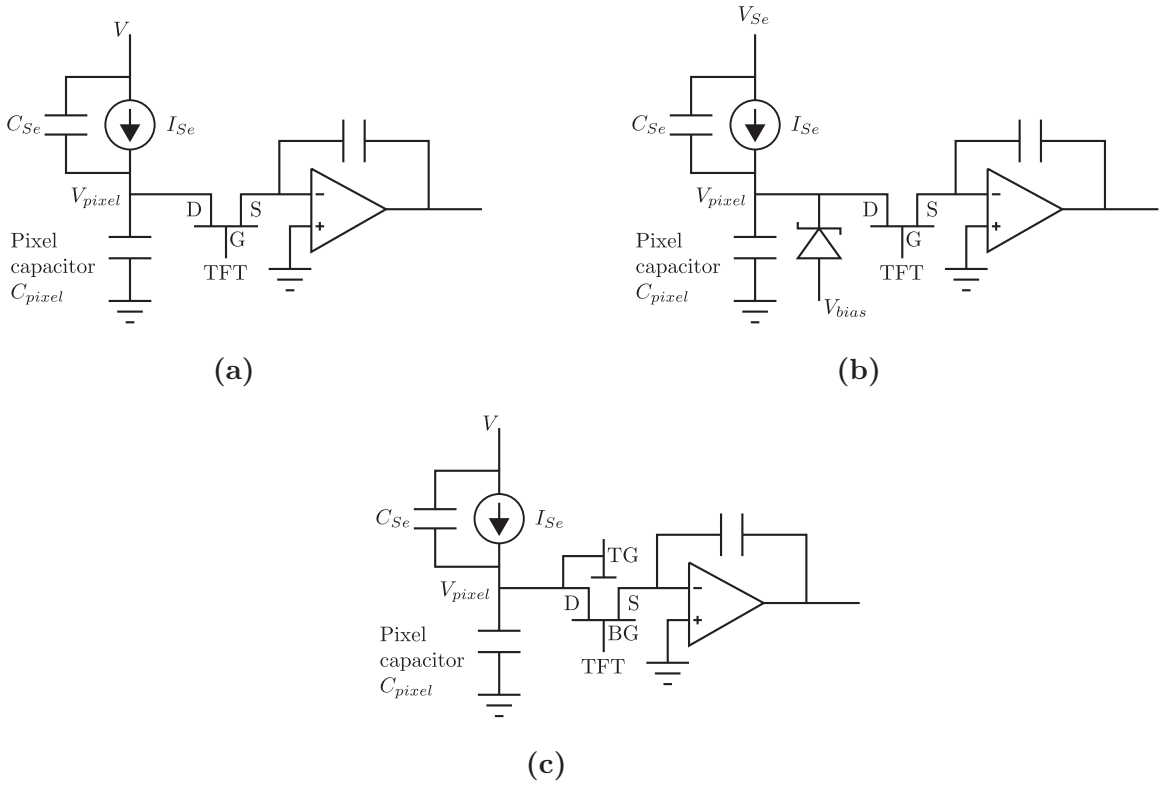

Figure 1.3: Circuit for photoconductor based DR systems using (a) Conventional system, (b) Zener diode, and (c) dual-gate TFT.

ment is ∼5,000 V. Both positive and negative bias voltage can be applied at the top electrode. Shown in Fig 1.3a, if the applied bias voltage is positive, electrons are collected at the top electrode and holes are collected at the bottom charge collection electrode. The capacitance of the a-Se layer is much smaller (∼0.002 pF) than the pixel capacitor (∼1 pF) so the majority of the applied voltage is dropped across the photoconductor layer. When the panel is left without scanning, dark or signal current will cause the potential on the pixel electrode to rise towards the applied bias voltage. A voltage of ∼50 V can cause permanent damage to the thin-film transistor (TFT). A simple method to protect the TFT is to use a negative bias at the top electrode so negative charges are collected at the pixel electrode. Eventually the charges accumulated at the storage capacitor will cause the TFT to partially turn on, and this will prevent the large potential from accumulating on the pixel

(the gate voltage is not negative enough to turn off the TFT). Other methods are also used to protect the TFT. One method is to put a Zener diode in parallel with the storage capacitor. Another method is to modify the TFT to incorporate a second gate. Shown in Fig. 1.3b-c, both methods will allow the allow the potential accumulated on the pixel to drain away if it exceeds a predetermined safe design value. However since these charges are drained out along the read-out lines, pixels sharing the same read-out lines as the over-exposed pixel can potentially contain corrupted information (Kasap and Rowlands, 2002; Rowlands and Yorkston, 2000). Another disadvantage of a-Se is that it has a relatively low atomic number, $Z = 34$, which is not suitable for higher diagnostic x-ray energies ($\sim$60 keV). As a result, a-Se is usually used in mammography devices operating at 20-30 kVp.

1.1.2 Indirect approach

In the indirect approach, detection materials such as phosphors or scintillators are placed in close contact with the active-matrix array. An x-ray interaction in the detection material produces lower-energy photons typically in the visible range. These lower-energy photons are then collected by a photosensitive element, such as a photodiode in each pixel, which in turn generates electrical charges. These charges are then stored and read out by the active-matrix array to form an image. The term indirect refers to the fact that x-ray interactions are detected indirectly using the electrical charges produced by the lower energy photons from the detection material rather than the electrical charges produced directly within the detection material.

The most common materials used in flat-panel detectors that employ the indirect approach are $Gd_2O_2S : Tb$ and $CsI : Tl$. Historically, powdered phosphors were deposited on plastic screens and were mainly used in x-ray imaging to expose photographic films; scintillators were grown as crystals and were used to detect high energy x- and gamma-rays (Nikl, 2006). Although phosphor screens and scintillators were prepared differently, the fundamental physics behind both are identical.

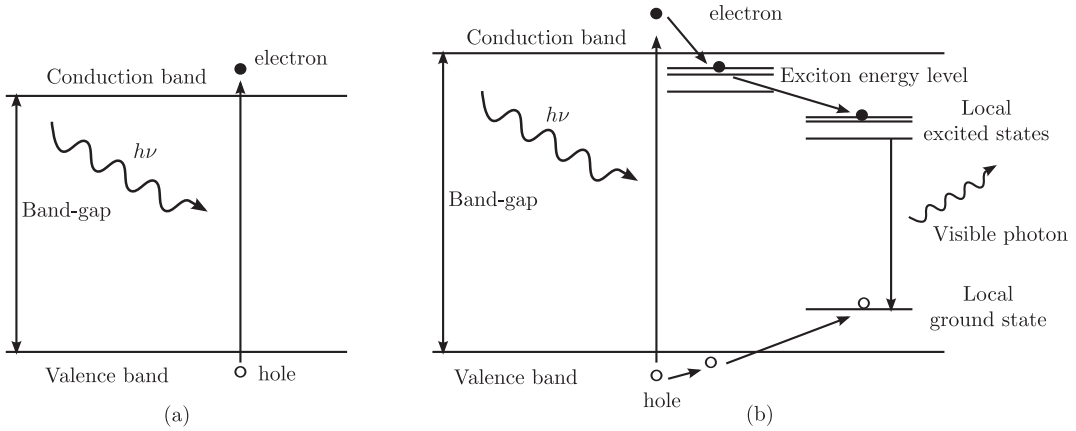

Figure 1.4: Energy band structure of (a) a semiconductor/photoconductor and (b) a scintillator/phosphor.

The initial interaction between scintillators and photoconductors is identical, where photoelectric absorption takes place and many electron-hole pairs are created from the absorption of a single x-ray photon. In an insulating crystal, the band-gap, E_g, between the valence and conduction band is large. So, less electron-hole pairs are created, and the energy released when an electron and a hole recombine is usually re-absorbed inside the material. As a result, very few secondary photons are released. In a scintillator or phosphor, we desire the radiative energy to escape the material without re-absorption and the conversion process to be more efficient.

In a scintillator or phosphor, the lattice defects and/or impurities introduce local discrete energy levels between the forbidden gap. When electrons and holes are created by the x-ray photon, the holes in the valence band will quickly move up into the ground states created by the defects and/or impurities. When an electron moving in the conduction band encounters these ionized sites, it can drop down into the local energy level and de-excite into the ground state (Knoll, 2010). A more common process is via an exciton, where the electron in the conduction band is bound to a hole in the valence band. This exciton can move freely in energy levels that are slightly below the conduction band. When the exciton encounters an unoccupied energy level inside the forbidden gap, both the hole and electron are captured simultaneously. This releases a photon with energy equal to the difference

between the local excite and ground state energy, which is smaller than the band-gap. Typically this energy is approximately 2-3 eV, which is in the visible range. This secondary photon cannot be re-absorbed to create more electron-hole pairs, so it is free to exit the material. Since many electron-hole pairs are created by the absorption of one x-ray photon, and the energy of an x-ray photon is much larger than the energy of a visible photon, many visible photons are created in the scintillator or phosphor by one x-ray photon. For example, in $Gd_2O_2S:Tb$ at ∼20% conversion efficiency, a 60 keV x-ray photon incident on the screen will produce approximately 5,000 green photons each with energy ∼2.4 eV.

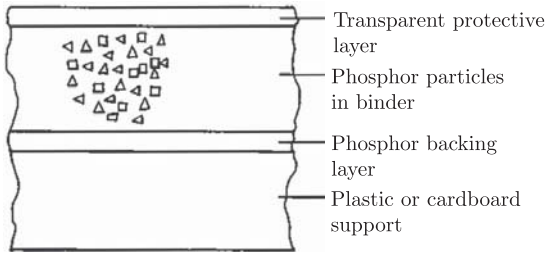

Figure 1.5: Cross section of a phosphor screen[2].

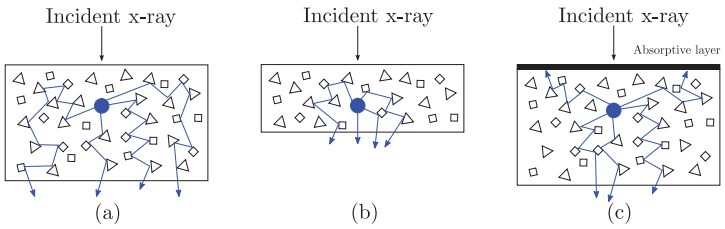

Figure 1.6: The effects of (a) a thick phosphor layer, (b) a thin phosphor layer, and (c) an absorptive backing of x-ray screens on spatial resolution.

The main issue with phosphor screens is that optical scattering within the screen affects the spatial resolution, which depends on the screen thickness. A thicker screen increases the probability of x-ray interactions, but lowers the spatial resolution. When a photon exits a phosphor grain, it will scatter off the neighboring phosphor

[2]Reprinted from Barrett, H. H. and W. Swindell(1981). *Radiological Imaging - The Theory of Image Formation, Detection, and Processing Volume 1.* Academic Press, Copyright(1981), with permission from Elsevier.

grains until it escapes the screen. The final location where the photon is detected may not be the same as the initial x-ray interaction. This spread of secondary photons lowers the spatial resolution. Shown in Fig. 1.5, phosphor screens are typically made with several layers starting with a stiff plastic support to discourage severe bending. The phosphor powders are sandwiched between a protective layer and a backing layer. The backing layer can be made with an absorptive material to discourage optical diffusion. This increases the spatial resolution at the cost of lowering the total number photons escaping the screen. The backing layer can also be made with a white diffusive material to increase the light output but at the cost of lowering spatial resolution. These effects are seen in Fig 1.6. Newer types of scintillators such as columnar CsI : Tl are grown as crystals in needle-like structures, which help to guide the emitted photons toward the exit surface. These structures allow thicker scintillators to be made, which increase the probability of x-ray absorption while limiting the spread of visible photons to within a few column structures, shown in Fig. 1.7. The result is a scintillator with higher spatial resolution than the phosphor screen even if both were made to have the same x-ray absorption and light output.

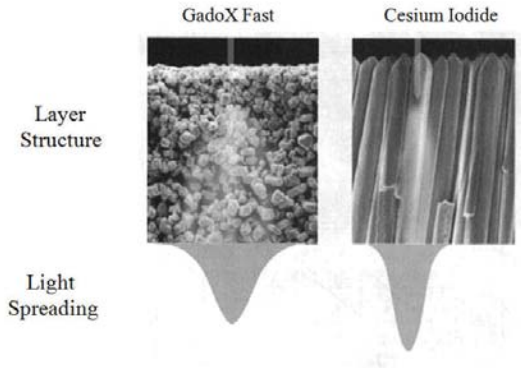

Figure 1.7: Gd_2O_2S : Tb phosphor and CsI scintillator viewed under SEM (VIDISCO, 2014).

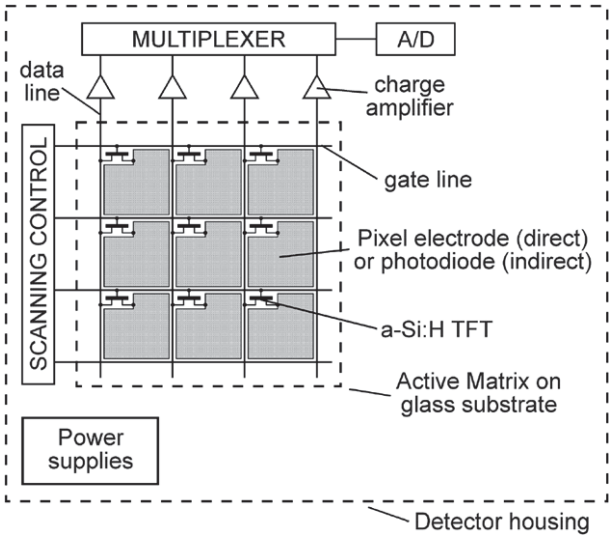

Figure 1.8: Schematic diagram of the main components of an active matrix array that are used to control the readout process © 2008 IEEE (Fahrig et al., 2008).

1.1.3 Readout arrays

Although the active-matrix arrays designed for detectors employing indirect and direct approach are slightly different, the readout schemes for both are exactly the same. This process is not like the readout method used in a charge-coupled devices (CCD), where the signals are transferred through pixels in columns and read out through a common output amplifier. Here the signal in each pixel element is transferred directly to the readout amplifier. Shown in Fig. 1.8, each row of the active-matrix array requires a separate gate line, and each column of the array pixels is connected to a separate data line each with its own charge amplifier. During readout, the gate line in the first row of the array is turned on while all other rows are put in their off state. This action turns on the thin-film transistors (TFTs) in the first row, and the signals from each pixel in the first row are transferred through the data line. Once all the pixels have been read out in this row, the control switches the first row to the off state and turns on the second row, where the same procedure repeats again until all pixels in the flat-panel array have been read out.

1.1.4 Fill factor

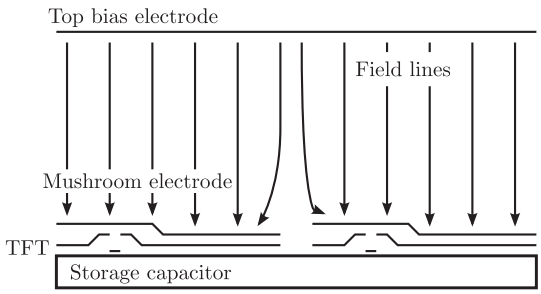

Figure 1.9: Mushroom electrodes are used to increase the effective fill-factor of a pixel.

One of the most important factors in flat-panel detector is the fill factor, which is the fraction of the pixel area that is sensitive to incoming signal. In the indirect approach, this is the fraction of the photodiode area in the entire pixel that includes the photodiode, electrodes, the readout switch, and various control lines. The fill factor in the direct approach can be much higher because the use of mushroom electrodes. The mushroom electrodes extend over the top of the switching elements and bends the electric field, so the charges can drift away from dead zones and are collected onto the capacitor as seen in Fig. 1.9.

The design rule that is used to fabricate a particular active-matrix array governs many factors such as the thickness of the metallic lines and gaps between neighboring pixels, which are usually independent of the pixel sizes. As a result, as pixels are made into smaller and smaller sizes, the fill factor will drop significantly. This is seen in Fig. 1.10.

1.2 Lens-coupled x-ray detectors

In a lens-coupled x-ray detector system, an x-ray phosphor screen is imaged with a lens onto a digital camera. Potential advantages of this approach include low cost; easy interfacing with existing computers and display software; rapid readout; flexibility in using different phosphors and different magnifications for particular

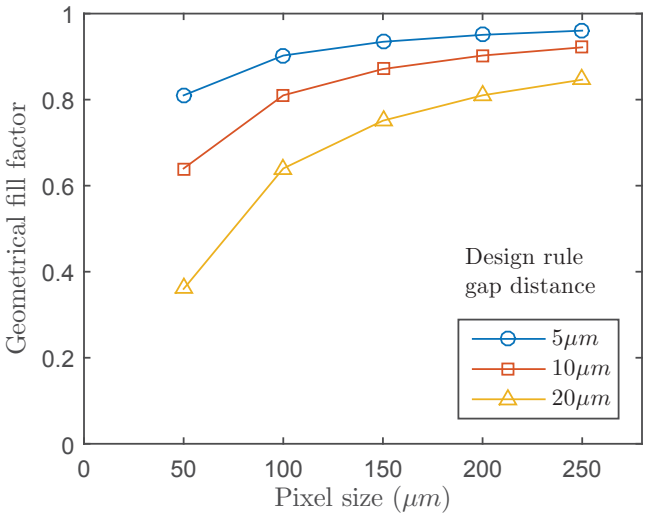

Figure 1.10: The geometric fill factor of pixels with different design rules and pixel sizes. Here the gap size is the distance between electrodes/photodiodes.

applications, and the consequent ease of trading field of view for spatial resolution. Moreover, the crystalline silicon sensors used in digital cameras are inherently much less noisy than the amorphous silicon sensors used in flat-panel devices, and they can be cooled to reduce the noise further if desired

For clinical applications, the basic problem comes down to the collection efficiency of the photons produced by the phosphor or scintillator. Enough photons from the phosphor screen need to be collected so the noise on the detector is limited by photon noise instead of inherent detector noise. Although collection efficiency of flat-panel detectors depends on their fill-factor, the collection efficiency of lens-coupled x-ray detectors depends on the lens' numerical aperture (NA).

The collection efficiency is the fraction of the solid angle from the source that is collected by the lens and focused onto the camera detector. If we consider an on-axis source with a right circular cone, the solid angle can be calculated using

$$\Omega = \int_0^{2\pi} d\phi \int_0^{\Theta_{1/2}} sin\,\theta\ cos\,\theta\ d\theta = \pi\ sin^2\,\Theta_{1/2}, \tag{1.1}$$

where θ, ϕ, and $\Theta_{1/2}$ are shown in Fig. 1.11. For a lens, the NA is equal to $n\,sin\theta$,

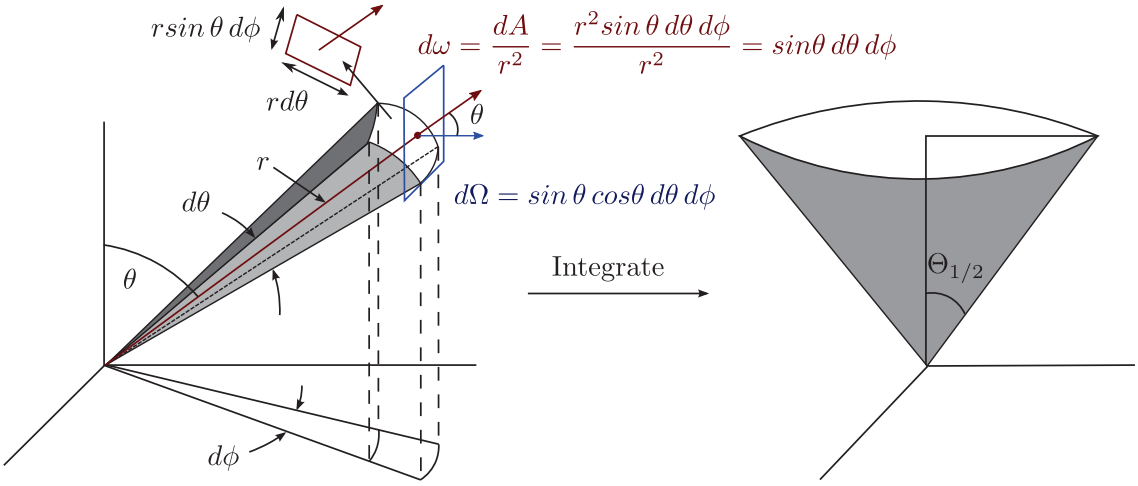

Figure 1.11: Solid angle $d\omega$ and projected solid angle $d\Omega$.

where n is the refractive index of the medium in front of the lens ($n = 1$ in air), and θ is the angle of the marginal ray with respect to the optical axis at the object. So the solid angle collected by a lens in air is

$$\Omega_{lens} = \pi sin^2\theta = \pi NA^2. \tag{1.2}$$

The solid angle of the source can be calculated similar to Eq. 1.1, and if the source is Lambertian, then $\Omega_{source} = \pi$. The collection efficiency of the lens is then

$$\eta = \frac{\Omega_{lens}}{\Omega_{source}} = sin^2\Theta_{1/2} = NA^2, \tag{1.3}$$

which holds true for all lenses used in air.

The magnification of a lens, m, is given by

$$m = -q/p, \tag{1.4}$$

where p is the distance from the object to the lens' front principal plane (P), and q is the distance from the lens' rear principal plane (P′) to the image. This is shown at the top diagram in Fig. 1.12. If the lens is used in conditions that do not satisfy the paraxial approximation but are well corrected for spherical and coma aberrations, we can use the Abbé sine condition to derive the collection efficiency. Shown at the

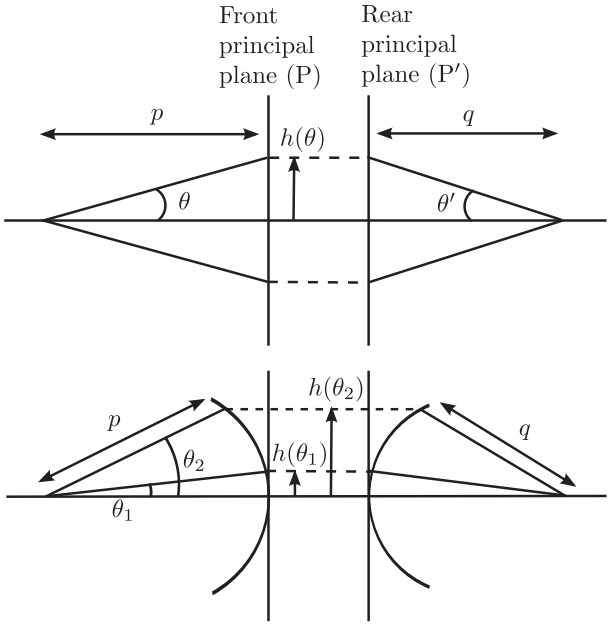

Figure 1.12: The Abbé sine condition.

bottom diagram in Fig. 1.12, the Abbé sine condition uses spherical surfaces rather than principal planes. Here the distance p and q are the radius of the spherical surface rather than the distance of the object and image to the principal planes. The condition states that $p\,sin\theta = q\,sin\theta'$ even when the paraxial approximation ($sin\theta \approx tan\theta \approx \theta$) does not hold true, which might be the case when imaging a large object with a lens that has a large NA. The collection efficiency of the lens used under the Abbé condition is

$$\eta_{Abbé} = m^2 sin^2\theta', \tag{1.5}$$

where θ' is the angle of the marginal ray in image space.

If the lens is used in conditions that satisfy the paraxial approximation, then we can use the F-number of the lens to calculate the collection efficiency. The F-number describes the image-space cone of light for an object at infinity. Under the paraxial approximation, this cone of light is approximately equal to (Greivenkamp, 2004)

$$F \equiv \frac{f_E}{D_{EP}}, \tag{1.6}$$

where D_{EP} is the diameter of the entrance pupil and f_E is the effective focal length. When two lenses are set to image at infinity and are mounted in a snout-to-snout fashion, then the diameter of the exit pupil is equal to the diameter of the entrance pupil. The light cone between the two lenses is collimated and the numerical aperture of the lens-set is equal to the image forming cone of light described by the F-number. The collection efficiency for the lens-set is then

$$\eta_{lens-set} = \frac{1}{F^2}. \tag{1.7}$$

This set up can be used when unit magnification between the object and image is desired.

When a single lens is used in conditions that satisfy the paraxial approximation. For example, when the object is not at infinity but the distance between the object and lens is still quite large. We can use the working F-number to describe the image-forming cone as,

$$F_w \approx (1 + |m|)\, F. \tag{1.8}$$

The marginal ray angle in image space can then be related to the working F-number as,

$$sin\theta' = \frac{1}{2F_w} = \frac{1}{2F\,(1 + |m|)}. \tag{1.9}$$

The collection efficiency of the lens under paraxial approximation is equal to

$$\eta_{paraxial} = \frac{m^2}{4F^2(1 + |m|)^2}. \tag{1.10}$$

While the phosphor screen must be at least the size of the object to be imaged, the lens must be able to capture the entire field of view (FOV) onto a CMOS or CCD detector with a limited size. For a fixed FOV and a small detector, we must move the lens and detector away from the object in order to fit the entire image of the object onto the sensor. In order to increase the collection efficiency, which depends on the marginal ray angle, we can move the lens and detector to decrease p, which will increase m. This means the detector size must be made larger. Alternatively, we can increase the marginal ray angle by increase the aperture size of the lens.

This means using a lens with a high numerical aperture (NA). In order to have both a large FOV and a high collection efficiency, we need both a large detector and a lens with high NA. Commercial lenses with high NA (or low F-number) can be purchased at reasonable prices. A F-1.4 DSLR lens can be purchased at approximately $600. Detectors with large sensor size can be extremely expensive and difficult to manufacturer. As a result, previous lens-coupled x-ray detector systems have been limited to small-scale imaging applications (Kim et al., 2005; Lee et al., 2001; Madden et al., 2006; Tate et al., 2005).

Recent sensor technology has improved tremendously, making it easier to purchase a camera with a large sensor size. Current consumer-grade digital single-lens reflex (DSLR) cameras can be purchased with 36 mm $\times$ 24 mm detector size at around $2000. This improvement in sensor size allows us to decrease the distance between the lens and phosphor screen, therefore improving the photon collection efficiency while maintaining a large field of view.

In this dissertation, two x-ray imaging systems, a digital radiography (DR) system and a computed tomography (CT) system were built using the concept of lens-coupled detector system. These systems are introduced in chapter 2. A method of evaluating x-ray CT detectors using an observer model is presented in chapter 3. The x-ray CT system presented in this dissertation is a fully functioning image system complete with calibration and reconstruction algorithms. These algorithms are explained in chapters 4 and 5.

CHAPTER 2

DESIGN AND CONSTRUCTION OF X-RAY IMAGING SYSTEMS

2.1 Introduction

Access to modern digital radiology is very limited in developing countries (Wootton et al., 2009). The Himalayan regions of Nepal, India, Pakistan and Tibet present special difficulties because of lack of adequate roads, inconsistent or nonexistent power grids, little internet access, and few trained physicians. In Nepal, for example, all of the remote district hospitals and many health outposts have x-ray facilities, but they are all film-based. There are very few resident radiologists, and teleradiology is rare (Graham et al., 2003; Wootton et al., 2009).

The goal of our work is to develop an inexpensive x-ray imaging system intended for wide dissemination in the Himalayan regions of Nepal and other rural areas in developing countries.

Two types of x-ray imaging systems with large fields of view (FOV) have been built. This section describes the design and construction of these two systems: the portable digital radiography system (DR) and the computed tomography (CT) system. Both systems were based on a similar concept, where a phosphor screen is imaged onto a pixelated detector using a fast lens. The digital radiography system is solely a 2D planar-imaging system that includes a phosphor screen, lens, and camera. The CT system is a test bench that can be used to test the performance of x-ray imaging systems using various scintillation screens and cameras. The CT system has a powerful research-grade x-ray tube that allows current and output kVp adjustments with a relatively small source spot size. In addition, the CT system is equipped with adjustable apertures, a rotary stage, and linear translation stages that

allow the system to test x-ray detection performances at different magnifications.

2.2 Design considerations for the DR system

2.2.1 Cameras and lenses

The DSLRs considered here are "full-field" cameras, which means that the sensor is approximately the same size as a frame of 35 mm film (24 mm × 36 mm). This format is also referred to in the DSLR world as FX. Cameras in this class include the Canon 6D and 5D Mark III, and the Nikon D810, D750 and Df. Even larger sensors are also available; for example, the MegaVision E6 which has a 37 mm × 49 mm sensor, but it is substantially more expensive than the "prosumer" (professional/consumer) full-field cameras.

A 24 mm × 36 mm sensor operated at 12:1 demagnification will allow the imaging of 29 cm × 43 cm FOV, adequate for chest radiography. For comparison, a 37 mm × 49 mm sensor will cover a comparable field at 8:1 demagnification. Of course, smaller FOVs require proportionally smaller demagnification factors. With a full-field camera, a 12 cm × 18 cm FOV can be achieved at 5:1 demagnification.

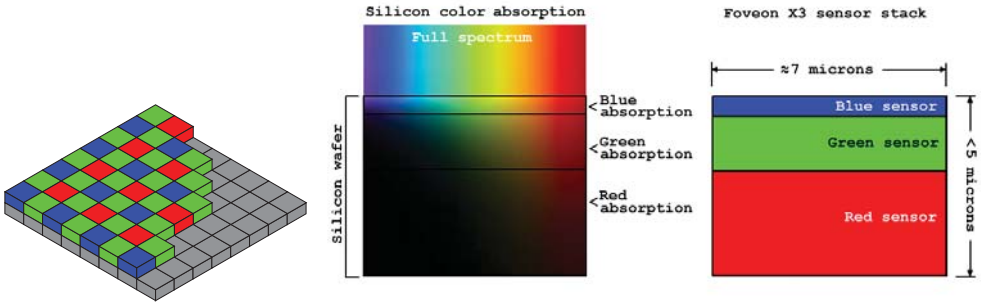

Figure 2.1: Two methods of achieving color selectivity using (a): the Bayer filter (Wikipedia, 2006): or (b): the Foveon X3 technology (Wikipedia, 2007).

Most of DSLRs are color cameras. The color selectivity can be achieved with two methods. The most common is by placing a mosaic color filter, commonly known as a Bayer filter, over the photosensitive pixels (Fig. 2.1a). Usually, half of the pixels are sensitive to green light, a quarter of them are sensitive to blue light, and a quarter to red light. These color filters are a distinct drawback because they reduce the quantum efficiency of the sensor. Fortunately, half of the pixels are well matched to the emission spectrum of green rare earth x-ray screens, such as gadolinium oxysulfide ($Gd_2O_2S : Tb$). A less common method of creating color sensitivity on the detector is the Foveon X3 sensor (Foveon, 2010). Sensors that use this technology feature three layers of pixels, each detecting a different color (RGB) to form a direct color-image sensor that can capture color in a way very similar to color film cameras (Fig. 2.1b). It is possible that more photons entering the camera will be detected by the Foveon X3 sensor compared to a mosaic sensor, particularly matching to the emission spectrum of $Gd_2O_2S : Tb$ since the green light from the x-ray screen needs to pass through only a thin layer of blue sensor before being absorbed by the second layer of green sensor. Unfortunately, this technology is relatively new, and only a limited number of cameras currently made by Sigma Corporation employ the Foveon sensor. The Foveon X3 sensor has been noted as noisier than the sensors in other DSLRs that use the Bayer filter at low-light conditions (CNET, 2004; Digicams, 2003). The only black-and-white DLSR, named "Henri", is made by Leica. It would provide a huge increase in collection efficiency though the camera itself costs over $8,000. Another way to artificially produce a black and white camera is by carefully removing the color filter on top of the sensor. A company called LDP, LLC has been doing this since 1996. This procedure typically terminates the camera's warranty with the original manufacturer, and they are able to convert only a limited number of cameras (MaxMax.com, 2014).

Most of the new DSLRs use CMOS (complementary metal oxide semiconductor) sensors rather than CCDs (charge-coupled devices), which means that they have circuitry for charge integration, preamplification, noise control, and readout switch-

ing at each individual pixel. This circuitry greatly improves the camera's noise performance (see Sec. 2.2.3), but it reduces the silicon area that is available for the photosensors, and that in turn would further reduce the quantum efficiency were it not for two clever optical tricks employed by most of the major DSLR manufacturers. The first is to use an array of microlenses to concentrate light on the active sensor area, shown in Fig. 2.2. For light arriving at the sensor at normal incidence, each microlens focuses the light into the center of its photodetector element, but for non-normal incidence, the light could be diverted to the insensitive areas between photodetectors.

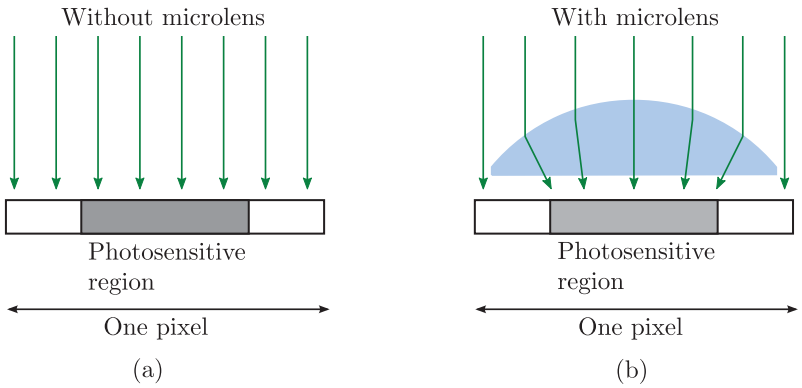

Figure 2.2: (a) A pixel is used without microlens. (b) A pixel is used with microlens.

This latter problem is avoided with so-called "digital" lenses, which simply means that they are intended to be used with digital cameras. The important feature of digital lenses is that they are telecentric in image space, so the chief ray is always perpendicular to the sensor plane and hence parallel to the optical axes of the microlenses. The result is that nearly all of the light transmitted by the lens and color filters arrives at the active area of the CMOS sensor.

Canon, Nikon, and other manufacturers supply fixed-focus (non-zoom) F/1.4 digital lenses for full-field DSLRs. Older lenses designed for use with 35 mm film cameras such as the Nikkor 50 mm, F/1.2, can also be used, but sensitivity at high field angle will be sacrificed because the lenses are not telecentric. Specialty lenses as fast as F/0.7 are available on the surplus market, but they do not usually cover

the full FX format.

2.2.2 Spatial resolution

The full-field DSLR sensors all have nominally either 12 or 24 megapixels (MP). The 12 MP cameras (e.g., Canon 5D or Nikon D700) have approximately a 2,800 $\times$ 4,300 array of 8.5 μm $\times$ 8.5 μm pixels, and the 24 MP cameras (e.g., Canon 5D Mark II or Nikon D3X) have approximately a 4,000 $\times$ 6,000 array of 6 μm $\times$ 6 μm pixels. If we consider 12:1 demagnification as for chest radiography, the 12 MP cameras provide effectively 100 μm $\times$ 100 μm pixels at the x-ray screen, and the 24 MP cameras provide 72 μm $\times$ 72 μm pixels. Larger effective pixels can readily be achieved by binning the sensor pixels during readout.

Fixed-focus lenses designed for use with full-field DSLRs and used at full aperture typically have about 30 lp/mm resolution at 50% MTF, which corresponds to a focal-plane resolution of about 15 μm FWHM. At a demagnification of 12:1, therefore, the lens contribution to the resolution at the x-ray screen is about 2.5 lp/mm at 50% MTF or 180 μm FWHM.

The other significant contributor to spatial blur is the screen itself. Lanex screens ($Gd_2O_2S : Tb$) yield resolutions in the range of 1-3 lp/mm at 50% MTF depending on the speed of the screen. Columnar CsI screens, now available in chest size, can be as good as 5 lp/mm at 50% MTF and can have a thickness of 150 μm (Nagarkar et al., 1997). The demagnification does not affect the screen contribution to the resolution.

2.2.3 Noise

A major concern with using DSLRs for DR is collecting sufficient light from the x-ray screen (Hejazi and Trauernicht, 1997). At 10:1 demagnification, a standard F/1.4 camera lens will collect about 0.01% of the light emitted by a Lam-

bertian source. Measured conversion efficiencies (from x-ray energy to optical energy) of Gd_2O_2S : Tb or La_2O_2S screens are in the range of 18-20% (Kandaraks and Cavouras, 2001), which means that a single 60 keV x-ray photon will yield approximately 5,000 optical photons, each with energy around 2.5 eV (green). If we collect 0.15% of them, then only 7 photons will reach the camera sensor, and if the sensor quantum efficiency is around 25% (see Sec. 2.2.1), we obtain around 2 photoelectron per x-ray photon. These numbers improve somewhat if we use an F/1.2 lens or if we consider a smaller demagnification, and they could be improved further by removing the color filter or using one of the new brighter phosphors such as columnar CsI, $LaBr_3$, or ceramic scintillators such as GLuGAG and GGAG (Cherepy et al., 2009; Wang et al., 2012).

In addition to the x-ray photon noise, the noise generated in the DSLR, referred to generically as read noise, is a major issue. The potential contributors to read noise are dark current; kTC noise, which arises from resetting the gated integrators in either CMOS or CCD sensors; thermal noise in the electronics, and 1/f or flicker noise. Of these components, we can readily dismiss dark-current noise, which is negligible compared to the other noise sources for the short exposures used in x-ray imaging. Similarly, pure thermal (Johnson) noise is negligible compared to kTC and 1/f noise in most practical sensors. With respect to the two remaining noise sources, modern CMOS sensors have a huge advantage over CCD sensors, even over expensive scientific-grade cameras, basically because they place a lot of electronic circuitry at the individual pixels rather than at the end of a charge-transfer chain as with a CCD (Magnan, 2003).

To understand this point, consider first kTC noise, which is endemic in both CMOS and CCD sensors. In both, the charge produced by the light is converted to a voltage by storing it on a capacitor, which should be reset to zero after each conversion. Basic thermodynamics, however, shows that the residual voltage on the capacitor cannot be truly zero but instead fluctuates with a variance of kT/C (k = Boltzmann's constant, T = absolute temperature, C = capacitance). One way

of suppressing kTC noise (which really should be called kT/C noise) is a process called correlated double sampling (CDS) in which the voltage on the capacitor is measured after each reset and then again after the charge is stored and before the next reset; the difference between the readings is proportional to the photoinduced charge with little residual error from the thermodynamic effects. Alternatively, a process called active reset can be used in which feedback control drives the residual voltage on the capacitor close to zero.

In a modern CMOS sensor, there is an integrating capacitor and a CDS or active-reset circuit at each pixel. The capacitor is reset and the sensor is exposed to light for a frame period (100-200 msec for a sensor that operates at 5-10 frames per second, as many DSLRs do), and then the capacitor is reset again. The CDS or active-reset circuit must therefore operate only once per frame, but the circuits at all pixels can operate in parallel, so the overall processing rate is millions of times higher. In a CCD, by contrast, the signal remains in the form of charge until it is shifted out to a capacitor. There is just one reset and CDS or active-reset circuit, and it must operate serially at the pixel rate rather than the frame rate.

There is a similar advantage to CMOS detectors with respect to thermal noise, which has a variance that is proportional to bandwidth. The lower circuit bandwidth associated with parallel processing at the pixel level automatically results in lower noise. The 1/f noise is further eliminated by CDS at the pixel level. One way to see this is to note that if the power spectral density, $S(f)$, varies as $|f|^{-\beta}$, then its Fourier transform, the noise autocorrelation function, satisfies $R(\tau) \propto |\tau|^{\beta-1}$, which approaches a constant as $\beta \to 1$ (see Barrett and Myers (2004), Sec. 3.3.7). As a result, low-noise, scientific-grade CCDs are often read out at only 50,000 pixels per second, while prosumer DSLRs can go over a thousand times faster.

An excellent source for quantitative comparisons of CCD and CMOS cameras and sensors is the Clarkvision website (Clark, 2014). Tables and graphs given there show that prosumer DSLRs typically have an RMS read noise equivalent to about 3-5 electrons, but scientific-grade CCD cameras and sensors can be up to ten times

worse, in spite of their much higher cost and much lower bandwidth.

2.2.4 Image quality and Detective Quantum Efficiency (DQE)

A simple way to understand the effect of read noise on objective (task-based) image quality is to assume that all of the light emitted from a single x-ray interaction and collected by the lens ends up on a single pixel in the camera sensor. With the numbers given in Sec. 2.2.3, this might be a valid assumption if we use 2 × 2 or 3 × 3 pixel binning.

With this assumption, the performance of an ideal linear (Hotelling) observer (Barrett and Myers, 2004) for the task of detecting a known signal on a known background can readily be derived. The Hotelling detectability is given by,

$$SNR^2_{Hot} = \sum_{m=1}^{M} \frac{\bar{k}^2(\Delta\overline{N}_m)^2}{\sigma^2_{read} + \overline{N}_m(\bar{k} + \bar{k}^2)} \tag{2.1}$$

where the sensor contains M pixels, each of which is denoted by an index m; σ^2_{read} is the variance of the read noise (expressed in electron units and assumed to be the same for all pixels); $\overline{N}_m$ is the mean number of x-ray interactions imaged to pixel m when there is no signal present; $\Delta\overline{N}_m$ is a small change in that number when a signal is present, and k is the mean number of photoelectrons produced by each x-ray interaction (again assumed to be independent of m).

Following Gagne (Gagne et al., 2003), we can define a task-specific DQE (detective quantum efficiency) by dividing the Hotelling detectability for the actual detector by the detectability on the same task for an ideal detector that has no read noise and $\bar{k} >> 1$. For the task of detecting a uniform disk object on a flat background, we find

$$DQE = \frac{\bar{k}^2\overline{N}}{\sigma^2_{read} + \overline{N}(\bar{k} + \bar{k}^2)} \tag{2.2}$$

where $\overline{N}$ is the common value of $\overline{N}_m$ for all pixels in the disk region. If the disk region is large compared to the optical blur, for example for detection of a 1 mm

lesion, this same expression is obtained even without assuming that all of the light from one x-ray photon is imaged to a single camera pixel.

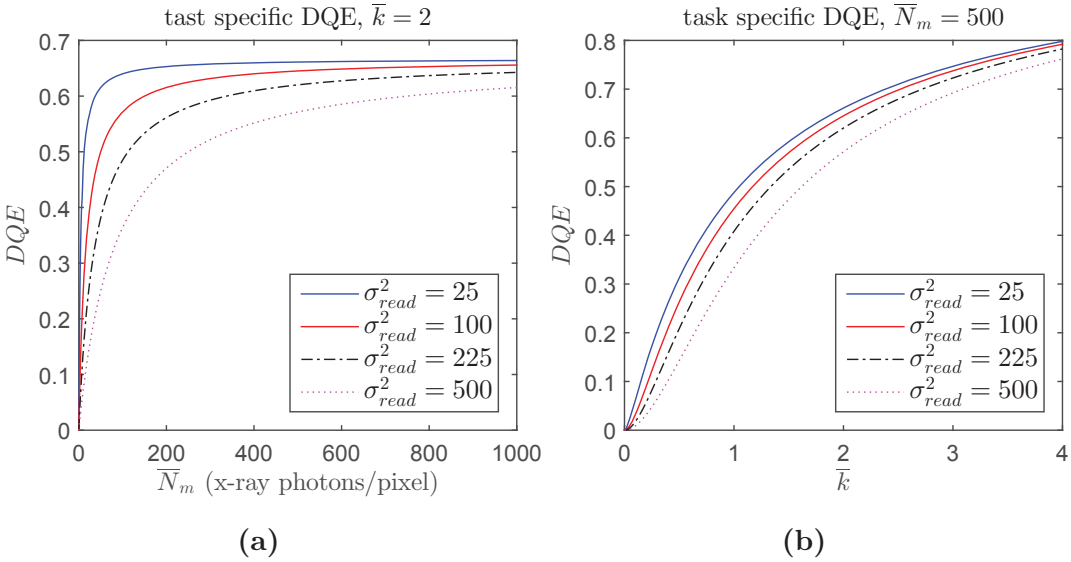

Figure 2.3: DQE for detection of a uniform disk lesion on a flat background. (a): DQE vs. x-ray fluence (absorbed photons per 100 μm pixel) for fixed optical efficiency (2 photoelectrons per x-ray photon) and difference camera read-noise variances. (b): DQE vs. optical efficiency for different x-ray fluences and noise levels. Typical $\overline{N}_m$ in DR is 500 photons per pixel, and typical σ^2_{read} in a modern DSLR is about 25 photons per pixel(5 electrons RMS).

The dependence of DQE on read noise, optical efficiency and x-ray fluence is shown in Fig. 2.3. Several limits are of interest. If there is no read noise but the lens is very inefficient so that $\bar{k} << 1$ the equation above predicts that the DQE of the detector (not including the x-ray screen) is simply $\bar{k}$. If there is no read noise but the lens is sufficiently efficient that $\bar{k} >> 1$, then we get DQE = 1. The case of interest, however, is when $\bar{k} \sim 1$ and the read noise is not zero. In that case, we can still get nearly quantum-limited performance, provided the x-ray fluence is high enough; if $\overline{N}_m(\bar{k} + \bar{k}^2) >> \sigma^2_{read}$, then the read-noise term in the denominator can be neglected and the DQE is $\bar{k}^2/(\bar{k} + \bar{k}^2)$. In order to do high-quality DR with a DSLR, therefore, it is very important to choose a camera with low read noise.

2.3 Prototype digital radiography system

A prototype digital radiography system was built with help from Jared Moore, Brian Miller, Stephen Moore, Heather Durko, and Lars Furenlid. Based on the cost and the design considerations above, we chose a Nikon D700 camera with an AF-S Nikkor 50 mm F/1.4G lens for the prototype. Because we elected not to use a folding mirror, the x-rays transmitted by the screen impinged on the camera. By measuring the x-ray transmittance of the lens, however, we found that the x-ray flux on the camera sensor was very small. No radiation damage was expected, and with several thousand x-ray exposures to date, none has been observed.

(a) **(b)** **(c)**

Figure 2.4: The imaging components that were used in the DR system, (a): Nikkor lens, (b): Nikon D700 camera, and (c): phosphor screen.

The imaging components inside the DR system are shown in Fig. 2.4. The system is constructed on an extruded aluminum frame that folds down into a small suitcase as shown in Fig. 2.5a. The vertical assembly on the right side in that figure is an opaque bakelite sheet with a standard Lanex screen mounted on the side facing the camera. The screens are interchangeable, and both Lanex Regular and Lanex Fast have been used. There is a light-tight felt cloth shroud, where only a thin camera cable needs to emerge from the shroud during operation, shown in Fig. 2.5b.

For transport, the suitcase contains the aluminum frame and x-ray screens, the shroud, a laptop computer, a solar panel for charging the computer and camera, a dosimeter and miscellaneous tools. Exclusive of the camera, which was carried

(a) **(b)**

Figure 2.5: First portable DR system that went to Nepal. (a): The uncovered prototype DR system showing an x-ray screen on the right and Nikon D700 DSLR camera on the left. The frame folds down into the suitcase for transport. (b): The same system but covered with a light-tight felt shroud in place. The system is shown as set up in the Manang District Hospital, Chame, Nepal, with the breast phantom in position for imaging.

separately, the DR system weighs about 45 pounds. The total cost of the system, including the camera, laptop, and lens, was less than $5,000.

The prototype system was taken to Nepal in spring, 2009, and tested in two clinics in the Kathmandu valley and in two district hospitals along the Annapurna Circuit Trail. Because all locations had existing x-ray tubes, no x-ray source was transported. A standard breast phantom was imaged with varying kVp and mAs and camera ISO settings at all four locations in Nepal and also in the Radiology Department of the University of Arizona. Comparison film-screen images were obtained at the Nepali locations, and Computed Radiography (CR) images were obtained in Arizona. Radiation exposure incidents on the phantom were measured in all cases.

A sample comparison using a breast phantom is shown in Fig. 2.6. The film image on the right was acquired in Nepal but brought back to Arizona and digitized by photographing it with the Nikon D700 camera, attempting to match the contrast

presentation with that of the DSLR image on the left as closely as possible. All features of interest are visible in both images, but uneven development and several white blotches, probably from foreign matter on the screen, are evident on the film-screen image.

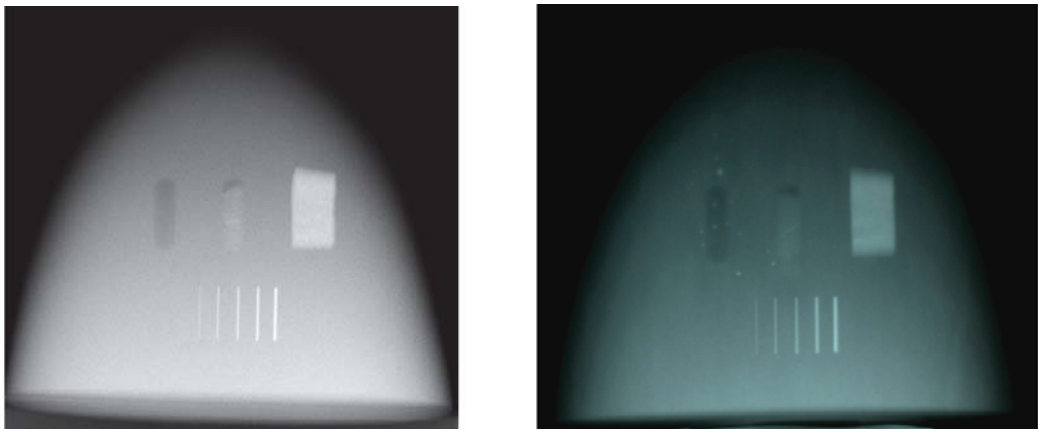

(a) **(b)**

Figure 2.6: Images of the breast phantom taken with the same exposure in a Himalayan clinic in Nepal, (a): an image taken with the DSLR system, and (b): an image taken with a local film-screen technique.

A second comparison, conducted entirely in Arizona, is illustrated in Fig. 2.7. In this case, a human skeleton embedded in plastic was the phantom, and the comparison was between the DSLR system and a Fuji CR system. The exposure conditions, noted in the caption, are not identical in this case, but we again made an effort to match the display contrasts. There is no evident difference in feature visibility.

2.3.1 Second prototype DR system

A second DR system was built in 2012 and delivered to Dr. Wendell Gibby, a radiologist from Utah. Slight adjustments were made to the first system because Dr. Gibby desired to test the DR system using his own camera at various magnifications; thus, this system does not include its own DSLR camera. This second system is

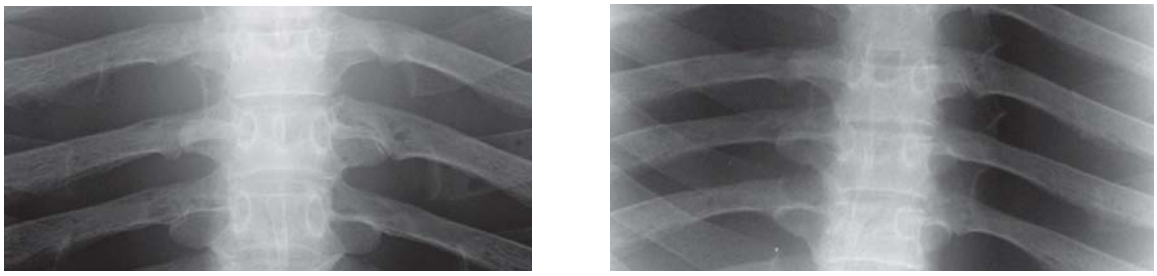

(a) **(b)**

Figure 2.7: Magnified portions of chest-phantom images taken at the University of Arizona with two different DR systems. (b): DSLR system, 80 kVp, 25mAs, ISO 4000. (b): Fuji XG5000 Computed Radiography system, 109 kVp, 10mAs.

slightly bigger than the first unit, although it is still collapsible. Instead of using a folding mechanism, we made so that the camera can be slid into different magnification positions to adjust for different fields of view. The entire system fits inside a large Pelican camera case and can be transported on wheels. Figure 2.8 shows the second system in SolidWorks, both in the measurement setup and the collapsible setup.

(a) **(b)**

Figure 2.8: The second portable DR system, showing (a): the DR system in imaging mode, (b): the system collapsed.

2.3.2 DR system results

When used with conventional x-ray screens, modern prosumer DSLRs are attractive detectors for DR. Compared to other consumer digital cameras, they have much lower read noise and substantially larger sensors, reducing the demagnification factor needed to cover a given FOV and hence increasing the light-collection efficiency. The use of microlenses to direct the light to the photosensitive region of each pixel along with telecentric "digital lenses" results in a sensor fill factor of, effectively, 100%. For large fields of view (e.g., chest radiography), the optical collection efficiency is approximately 1 photoelectron per x-ray interaction, but this number can be improved either by using smaller fields or by removing the color filter on the camera. Because the DSLR read noise is so low, the DQE (not including the screen absorption) for a disk-detection task can exceed 50%. Compared to scientific-grade CCD cameras, the DSLRs have significant advantages in cost, read noise, and readout speed. They cannot compete with CCDs in terms of quantum efficiency or dark current, but neither of these characteristics is critical for DR. Compared to current CsI or amorphous selenium flat-panel detectors, the main advantage of the DSLR approach is cost and readout speed. The resolution and noise performance of the DSLR system may be comparable to those of flat-panel detectors, but more studies are needed to confirm this conjecture. Compared to film-screen systems in rural clinics, a major advantage of the DSLR approach is the digital character of the data. A DSLR provides an instant digital image for display manipulation and telemedicine, and it eliminates concerns about control of the developing process. Moreover, the large dynamic range of the cameras should lead to fewer incorrect exposures than with film. The DSLRs may also offer advantages over film-screen in terms of resolution, noise, and the dose required for equal objective image quality, but many more studies are needed in this area. Finally, we note that the DSLR approach has the potential to bring fluoroscopy into rural settings; some DSLRs can take continuous data at 30 fps.

2.4 Prototype Computed Tomography (CT) System

The previous results from the DR systems were very promising, and we were interested in testing different cameras and x-ray screen combinations. In addition, we wanted to test how well this concept would work on a CT system. Therefore, the prototype computed tomography system was built. The system setup is shown in Fig. 2.9. Since this is only a prototype test-bench system, we decided to rotate the object on a leveled surface rather than rotating the x-ray tube and detector system on a gantry, thereby reducing the system's complexity while still maintaining our objectives. The frame of the CT system was built using extruded aluminum from 80/20 Inc., and an x-ray tube was mounted to a fixed location. The x-rays generated from the tube were converted to visible light after they have passed through the vertical x-ray phosphor screen located behind the cylindrical object, seen in Fig. 2.9b. The visible light from the phosphor screen is re-directed vertically via a 45° front-surface folding mirror. The camera and lens are mounted on a vertical translation stage to minimize direct x-ray exposure to the camera sensor.

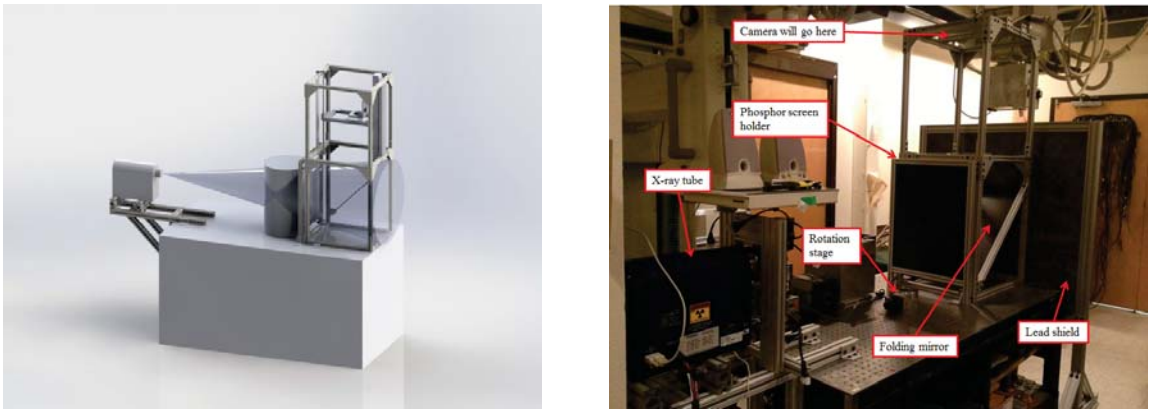

(a) **(b)**

Figure 2.9: The CT system configuration, (a): system model designed in SolidWorks, (b): the system setup in the lab.

Many safety measures were taken to minimize accidental x-ray exposure. All three entrances into the lab were wired with visible warning signs which will light

up when x-rays are generated. These entrances were also attached to magnetic on/off switches that will shut off the power to the x-ray tube immediately if any doors are opened while the x-rays were being generated. A hand-held "deadman's" switch was wired into place behind a shielded room to ensure that an operator is present at all times while x-rays were being generated. This is an extra safety step so that the operator can monitor the scanning process in order to prevent anything disastrous from happening. A 36 ″× 36 ″× 5/8 ″size lead sheet was placed behind the CT system to prevent direct x-rays from penetrating the room. These safety components are shown in Fig. 2.10 - 2.11.

(a) **(b)** **(c)**

Figure 2.10: Safety mechanisms installed in the x-ray room. (a): x-ray warning sign, (b): magnetic on/off switch on doors, (c) "deadman's" switch.

2.4.1 X-ray source

The CT test bench system is equipped with a very powerful research-grade x-ray tube from Fisher Scientific, shown in Fig. 2.12. It can generate x-ray beams up to 130 kVp with maximum current at 0.5 mA and any voltage and current values in between, although operation at low voltage and high current is not recommended. The x-ray tube has a small spot size which can vary with output power and operating voltage. The spot sizes are shown in Table 2.1. Resolution of our x-ray imaging system can depend on the source size. This is because a finite x-ray source can be viewed as a collection of point sources, where each point source creates an image

Figure 2.11: The lead shield for stopping direct x-rays.

of the object at the phosphor screen. An extended source would not affect the resolution if the object were infinitely thin and placed directly against the phosphor screen. However, anything less than this ideal situation would affect the resolution. When the distance between the x-ray source, object, and phosphor screen is large, then the resolution ultimately depends on the size of the x-ray source. Smaller spot sizes allow the x-ray images to have higher resolution, although smaller spot sizes also limit the total output produced by the x-ray tube. This problem can be easily overcome by increasing the exposure time on the camera since scan duration is not our top priority. The x-ray tube also has a very wide angular illumination output, with a nominal angle at 54°. This allows us to limit the distance between the x-ray tube and the phosphor screen.

Figure 2.12: The x-ray tube.

$\leq 10\ \mu m$ @ 8 watts, 50-130 kV
$\leq 22\ \mu m$ @ 16 watts, 50-130 kV
$\leq 48\ \mu m$ @ 32 watts, 70-130 kV
$\leq 100\ \mu m$ @ 65 watts, 130 kV

Table 2.1: The x-ray tube spot sizes.

2.4.2 Cameras

We have three different cameras at our disposal to test on the CT system, shown in Fig. 2.13 and Table 2.2. These are the Andor Neo, Nikon D700, and the PIXIS 2048B. The Andor Neo employs a scientific CMOS sensor with rapid frame rates up to 30 fps at full frame and is capable of operating at -40°C using built-in thermoelectric (TE) coolers in air. The camera is purchased with a LabView software development kit (SDK) and a 4 GB data acquisition board so that we can acquire data bursts at frame rates faster than the computer file-write speed. The Neo camera was integrated into the CT software in LabView. Currently, the camera's sensor temperature is cooled by attaching an external water cooler for longer CT scan routines. The Andor Neo camera has a microlens array in front of the detector. The quantum efficiency is approximately 55% at $Gd_2O_2S : Tb$'s emission wavelength.

The PIXIS 2048B is an ultrasensitive CCD camera, which has a large detector and pixel size compared to the Andor camera, and can cool down to -60°C in air. The camera has a very slow acquisition speed of 100 kHz, which is the mode used for image acquisition. The camera also has a higher readout speed at 2 MHz, which is used for adjusting the lens and field of view. The quantum efficiency is over 95% at $Gd_2O_2S : Tb$'s emission wavelength. The D700 Nikon camera was described in the previous section.

(a) **(b)**

Figure 2.13: Cameras used to test the CT system. (a): Andor Neo sCMOS camera, (b): PIXIS 2048B CCD.

Cameras	Princeton PIXIS	Andor Neo	Nikon D700
Sensor Type	CCD	scientific CMOS	CMOS
Pixel Pitch	13.5 μm	6.5 μm	8.5 μm
Array Size	2048×2048	2560×2160	4256×2832
Imaging Area	27.6×27.6 (mm^2)	16.6×14 (mm^2)	36×24 (mm^2)
Readout Speed	100 kHz	100 MHz	60 MHz
Microlens array	No	Yes	Yes
Color Filter	No	No	Yes, Bayer

Table 2.2: Cameras for the CT system.

2.4.3 Shutter

A shutter assembly, mounted to the front of the x-ray tube, is used to stop the x-ray beam, reduce x-ray exposure to the operator, and to prevent the tube from being repeatedly turned on and off. The shutter assembly was originally designed by Jared Moore for the FaCT system, and it has been modified to stop higher-energy x-rays. The shutter assembly is composed of a tungsten epoxy shutter, a rotary solenoid, and an optical sensor all mounted to an aluminum holder that can accommodate various x-ray filters, shown in Fig. 2.14.

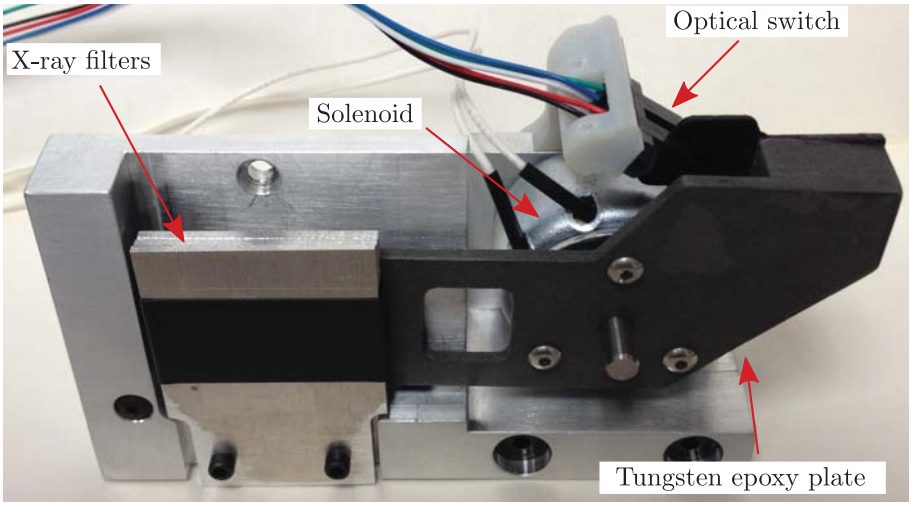

Figure 2.14: The x-ray shutter assembly.

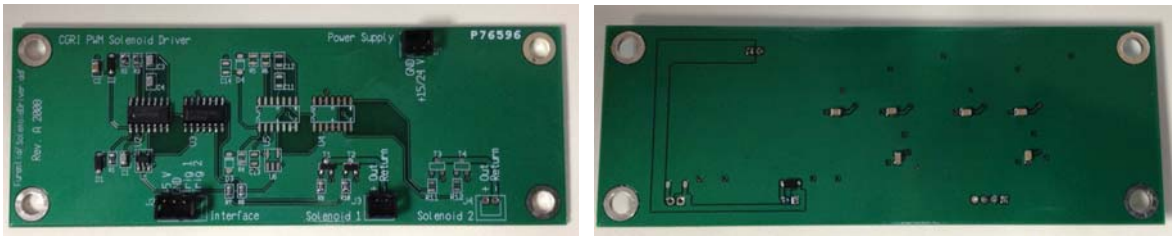

(a) (b)

Figure 2.15: Electronic PCB board for the shutter system.

The shutter assembly is controlled by an electronic prototype circuit board (PCB) designed by Lars Furenlid, shown in Fig. 2.15. The PCB controls the rotary solenoid by first feeding the solenoid with a large burst of current. This current rotates the solenoid and throws the shutter plate to the open position. An oscillating holding current follows the large current burst, keeping the shutter at the open position and preventing the solenoid from overheating. Fig. 2.16 shows the schematic diagram for the shutter board, and Appendix A provides a list of the components that were used for the shutter. The optical switch is used to make sure the shutter is fully open. The PCB is powered by a +24 VDC power supply. The trigger that controls the shutter is held at +5VDC when the shutter is fully closed and will open when the the trigger is set to ground. This trigger signal for the shutter assembly

is controlled via a National Instruments USB DAQ module. The shutter assembly trigger is integrated into the CT acquisition software.

2.4.4 Aperture assembly

The aperture assembly is used to mask the x-ray beam so that its projection size is slightly larger than the imaging field of view. The maximum beam size at the lead shield should never exceed the size of the lead shield itself (36 $''\times$ 36 $''$). The aperture assembly is constructed using four tungsten copper alloy plates (CW80) purchased from Leading Edge Metals & Alloys Inc., shown in Fig 2.17. The plate thickness (1/8 $''$) was calculated to ensure very little x-ray penetration (2.9×10^{-10} at 100 kVp, and 0.038% at 150 kVp). Linear translation stages, purchased from Velmex Inc., were used to move individual tungsten blades.

2.4.5 Software control

The x-ray source, aperture assembly, rotation stage, and the Anor Neo camera are integrated using LabView. This software also includes an x-ray tube warm up routine, CT scanning routine. A region-of-interest can be selected for the aperture assembly by either sending commands to individual motors, or using the graphic interface by dragging the cursors in the panel. The front control panel for the software is shown in Fig. 2.18.

2.5 Summary

We have described the components that were used to construct both the digital radiography system and the prototype computed tomography system. For the digital radiography system we have explained the reasoning behind our camera selection and lens selection; for the CT system, we have shown the major components and

the subassemblies in the system. We have also shown the safety features that were employed in the CT system.

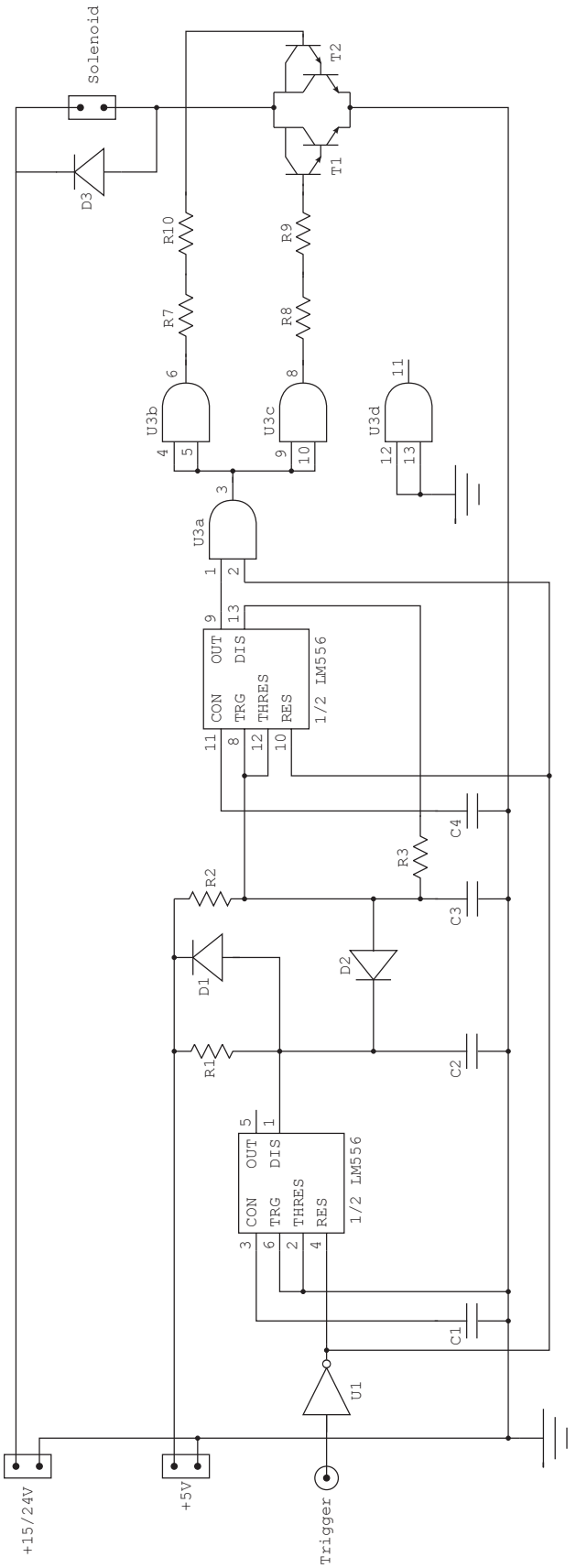

Figure 2.16: Schematic for the solenoid PCB board

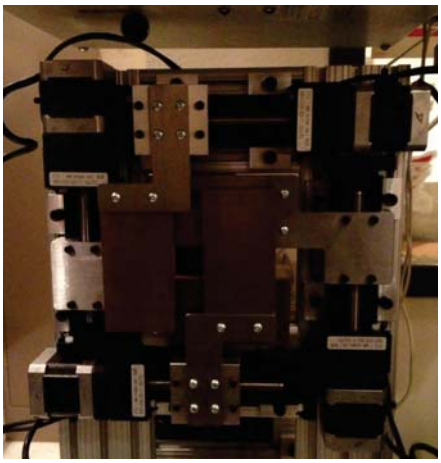

Figure 2.17: Aperture assembly

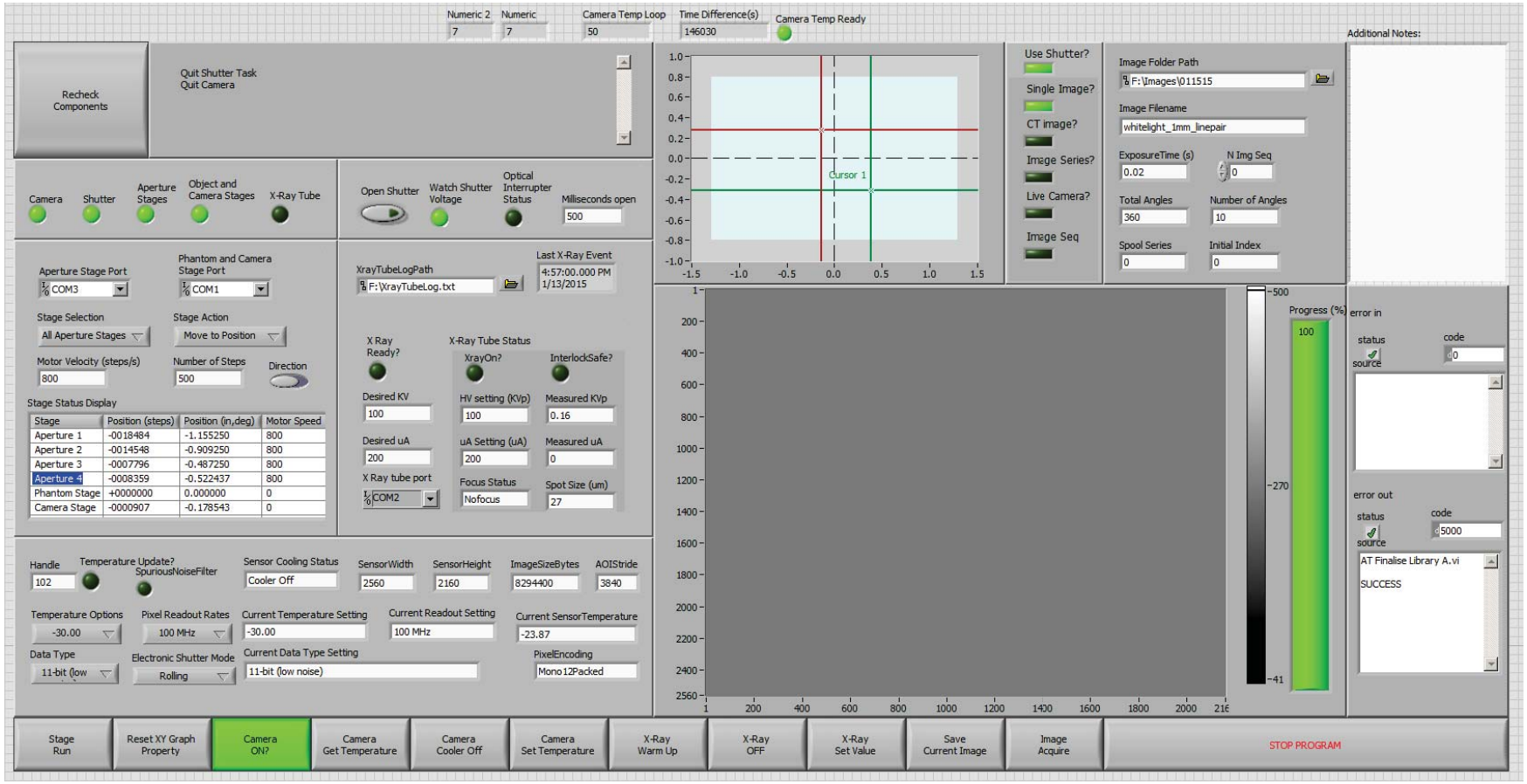

Figure 2.18: Software control panel for the system.

CHAPTER 3

FEASIBILITY STUDY USING MODEL OBSERVER

3.1 Introduction

When evaluating an imaging system, it is often useful to first use a model observer to compute the performance of the system. One can optimize the imaging system by calculating its performance using the model observer for a particular task with multiple input parameters. Considerable research has been performed in computed tomography (CT) on signal detection in flat backgrounds under various conditions, but little has been done with complex, random backgrounds. In this chapter we present a new way to evaluate the detector for signal detection tasks using raw projection data. This work utilizes the channelized Hotelling observer and the correlation between all pairs of channels over discrete angles to compute the signal-to-noise ration (SNR) as a figure of merit for the detector. The variables considered are number of incident x-ray photon per pixel, mean number of photoelectrons per x-ray photon, variance of camera read noise, the number of detector pixels, and the lumpiness of the background. The detector considered is a scintillator coupled to a small pixelated detector by a lens.

The best observer that can be used is the ideal observer or Bayesian observer, defined as the observer that utilizes all statistical information available regarding the task to maximize task performance as measured by Bayes risk or some other related measure of performance (Barrett et al., 2013; Barrett and Myers, 2004). However this method requires us to know the exact probability density function for all possible input, which is next to impossible. A much simpler observer is the Hotelling observer that only requires us to know the mean and covariance of our images. Although this sounds simple, even the Hotelling observer is computationally intensive and

very impractical. The Hotelling observer can be approximated by a number of channels, or mathematical functions. Different channels can be selected depending on the tasks at hand. An advantage to the channelized Hotelling observer is that it requires less computation to calculate the covariance matrix of the observer. We chose to use the channelized Hotelling observer to measure the system performance.

3.2 Theory

In x-ray imaging, the x-ray photons are attenuated when they pass through a material. For a monochromatic incident x-ray beam, the attenuation of the x-rays depends on the attenuation coefficient of the material and is expressed by the equation (Barrett and Myers, 2004),

$$\overline{N}_m = \overline{N}_0 \exp\left[-\int_0^\infty \mathrm{d}l\, \mu(\mathbf{r}_m - \hat{\mathbf{s}}_m l)\right], \tag{3.1}$$

where $\overline{N}_0$ is the mean number of x-ray photons that would strike detector m with no object present, $\mathbf{r}_m$ is the 3-D vector specifying the location of the detector m, $\hat{\mathbf{s}}_m$ is a unit vector from the source to detector m, and $\mu(\mathbf{r})$ is the attenuation function of the object. This equation assumes all rays from the x-ray point source to the detector subtend small angles ($\cos(\theta) \approx 1$), so $\overline{N}_0$ is the same for all m. The attenuation function of the object for this simulation is,

$$\mu(\mathbf{r}) = \mu_{H_2o}\, sph(\mathbf{r}/D) + \Delta\mu(\mathbf{r}), \tag{3.2}$$

where μ_{H_2o} is the attenuation coefficient of water, $\mathbf{r}$ is a 3-D vector in Cartesian coordinate, $sph(\mathbf{r}/D)$ is a spherical function of diameter D, where $sph(\mathbf{r}/D) = 1$ for$|\mathbf{r}| < D/2$, and 0 otherwise. The lumpy background model used by Rolland is $\Delta\mu(\mathbf{r})$, and is given by,

$$\Delta\mu(r) = \sum_{j=1}^{K} \Delta\mu_0 \exp\left(-\frac{|\mathbf{r} - \mathbf{r}_j|^2}{2r_b^2}\right), \tag{3.3}$$

where $\mathbf{r}_j$ is a random vector confined to a spherical diameter d, K is the random number of Gaussian lumps in the background, $\Delta\mu_0$ is the amplitude of the lump,

and r_b is the rms radius of the Gaussian lumps. Note that K is taken from a Poisson distribution with mean $\overline{K}$ and $\mathbf{r}_j$ is taken from a uniform distribution. The values $\overline{K}$ and $\Delta\mu_0$ are chosen so the mean of the lumpy background is equal to the attenuation coefficient of water. From Eqn. 3.1, the mean number of x-ray photons incident on the detector when $\Delta\mu(r) \ll d$ is,

$$\overline{N}_m \approx \overline{N}_{0m}\left\{1 - \int_0^\infty \mathrm{d}l \Delta\mu(\mathbf{r}_m - \hat{\mathbf{s}}_m l)\right\} \equiv \overline{N}_{0m}[1 - \Delta p_m], \tag{3.4}$$

where $\overline{N}_{0m} \equiv \overline{N}_0 \exp\{-\mu_{H_2o} \int_0^\infty dl\, \mathrm{sph}[(\mathbf{r}_m - \mathbf{s}_m)/D]\}$ and $\Delta p_m \equiv \int_0^\infty dl\, \Delta\mu(\mathbf{r}_m - \hat{\mathbf{s}}_m l)$. Because the read noise has zero-mean, we can write the projected value of the object on the detector m in electron units as,

$$\bar{g}_{m0} = \eta\bar{k}\overline{N}_{0m}[1 - \Delta p_m], \tag{3.5}$$

which is the conditional mean for a single realization of the lumpy background, with the data averaged over the Poisson fluctuations of the number of x-ray photons, over the photoelectron generation process, and over read noise. In this equation, η is the quantum efficiency of the detector and $\bar{k}$ is the number of photoelectrons produced per incident x-ray photon. These values are assumed to be the same for all detectors. The overall mean, including an average over lumpy backgrounds, is then given by,

$$\bar{\bar{g}}_{m0} = \eta\bar{k}\overline{N}_{0m}[1 - \Delta\bar{p}_m]. \tag{3.6}$$

The signal used in this study is a 2-D Gaussian function. In the signal-present case, the projected value on the detector and its mean are $\bar{g}_{m1} = \eta\bar{k}\,\overline{N}_{0m}[1 - \Delta p_m - \Delta s_m]$ and $\bar{\bar{g}}_{m1} = \eta\bar{k}\,\overline{N}_{0m}[1 - \Delta\bar{p}_m - \Delta\bar{s}_m]$, where $\Delta s_m \equiv \int_0^\infty dl\, \Delta\mu_s(\mathbf{r}_m - \hat{\mathbf{s}}_m l)$, and $\Delta\mu_s$ is the signal amplitude. When both measurement noise and object variability are taken into account, the general covariance matrix in component form is defined by (Barrett and Myers, 2004),

$$[\mathbf{K}_\mathbf{g}]_{mm'} \equiv \langle\langle[g_m - \bar{\bar{g}}_m][g_{m'} - \bar{\bar{g}}_{m'}]\rangle_{\mathbf{g}|\Delta\mu}\rangle_{\Delta\mu}. \tag{3.7}$$

Equation 3.7 simplifies down to two terms, one representing the average noise covariance and the other representing the object variability. These two terms are

described by the equation,

$$[\mathbf{K_g}]_{mm'} = [\overline{\mathbf{K}}_{\mathbf{g}}^{noise}]_{mm'} + [\mathbf{K}_{\bar{\mathbf{g}}}^{obj}]_{mm'}. \tag{3.8}$$

The noise term in the data covariance matrix is diagonal because we are assuming that there is no light spread in the scintillator (e.g. columnar scintillator crystals) and in the coupling optics between scintillator and optical detector. It follows from Burgess variance theorem (Barrett and Myers, 2004; Burgess, 1959) that the covariance matrix due to noise is,

$$[\overline{\mathbf{K}}_{\mathbf{g}}^{noise}]_{mm'} = \delta_{mm'}[\sigma^2 + \eta^2 \overline{N}_{0m}(\sigma_k^2 + \bar{k}^2)\langle(1 - \Delta p_m)^2\rangle_{\Delta\mu}]. \tag{3.9}$$

In equation 3.9, σ^2 is the variance of the camera read noise and σ_k^2 is the variance in the number of photoelectrons per x-ray photon. These variables are assumed to be the same for all detectors. The covariance matrix representing object variability is not diagonal, and its elements are given by,

$$[\mathbf{K}_{\bar{\mathbf{g}}}^{obj}]_{mm'} = \eta^2 \bar{k}^2 \overline{N}_{0m} \overline{N}_{0m'} \langle[\Delta p_m - \Delta \bar{p}_m][\Delta p_{m'} - \Delta \bar{p}_{m'}]\rangle_{\Delta\mu}. \tag{3.10}$$

The observer used for the task of signal detection is the channelized Hotelling observer. The application of using channelized observers for medical image-quality assessment is well established. It began with the work of Myers (Myers, 1985) and Myers and Barrett (Myers and Barrett, 1987), who introduced the channelized Hotelling observer. Others have used the channelized observer to estimate the ideal linear observer in order to assess images (Abbey and Bochud, 2000; Barrett and Abbey, 2001; Gallas and Barrett, 2003). Detailed treatments can be found in Abbey (Abbey, 1998) and Abbey and Bochud (Abbey and Bochud, 2000); for the purpose of this work, only the essential equations are provided for SNR calculation.

The SNR for the channelized Hotelling observer is given by,

$$\mathrm{SNR}_{\mathrm{Hot}}^2 = [\Delta \bar{\mathbf{v}}^{\mathrm{t}}] \mathbf{K}_{\mathbf{v}}^{-\mathbf{1}} [\Delta \bar{\mathbf{v}}], \tag{3.11}$$

where $\Delta \bar{\mathbf{v}} = \mathrm{U}^{\mathrm{t}}(\bar{\mathbf{g}}_{\mathbf{1}} - \bar{\mathbf{g}}_{\mathbf{0}})$, $\mathrm{K_v} = \mathrm{U}^{\mathrm{t}}(\mathbf{K_g})\mathrm{U}$, and U is the channel template. In this study we used 5 channels and the observer templates are the Laguerre-Gauss functions. This set of functions is used to detect the Gaussian signal because they form

a basis on the space of rotationally symmetric square-integrable functions. They can represent any rotationally symmetric function that is square integrable if an infinite number of terms were used. Since we have prior knowledge of the signal, both its exact location and the fact that the signal is rotationally symmetrical, the Laguerre-Gauss functions are a good choice for the observer template. Note that these channels were chosen not to mimic human performance but to estimate the ideal-observer performance.

3.3 Simulation Model

For this simulation, the object function parameters D and d are 500 mm and 20 mm, respectively. The attenuation coefficient of water (μ_{H_2o}) is 0.02 mm^{-1}. Figure 3.1 provides the overall system geometry considered in this study. The object function, measured from the center, is placed 500 mm behind the x-ray point source. The screen is placed 1000 mm away from the x-ray source. The size of the screen is 80 mm$\times$80 mm. The projection data are calculated using a fixed detector size and a varying number of pixels. The radius of each lump for the random background was set to 4.5 mm and the mean number of lumps that resides inside the sphere with diameter d was set to 180. The radius of the lumps and the mean number of lumps where chosen so that two points closer together has higher correlation compared with two points farther apart. The projection of the object function is calculated for 36 discrete angular increments about its vertical axis for both signal-present and signal-absent cases. The process is then repeated several hundred times using different object functions for various signal sizes and amplitudes. The channelized-Hotelling observer is trained for each signal radius, and the channelized covariance matrix is calculated between all pairs of channels as a function of angle. The final SNR represents the ability of the detector to detect the signal using the raw projection data over 36 discrete angles. Figure 3.2 is an example of the Laguerre-Gauss channel template for one particular signal size.

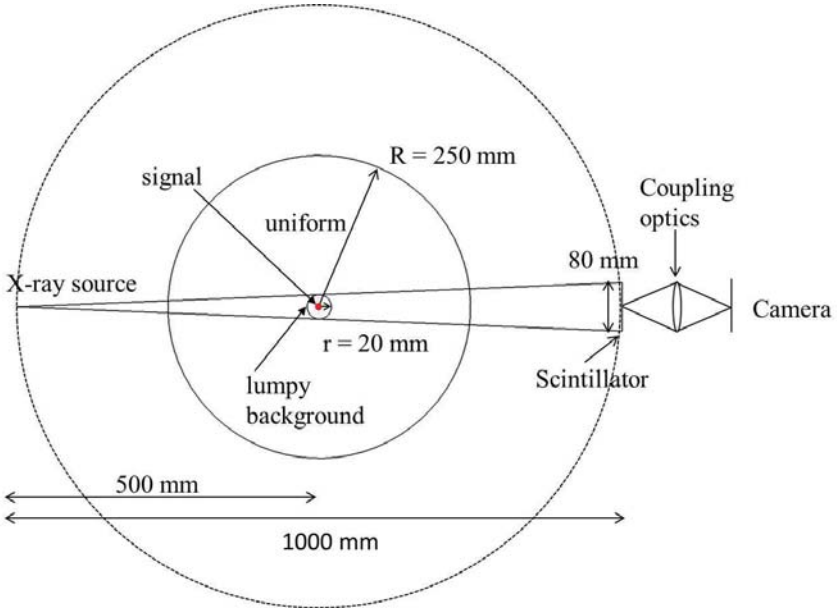

Figure 3.1: System geometry

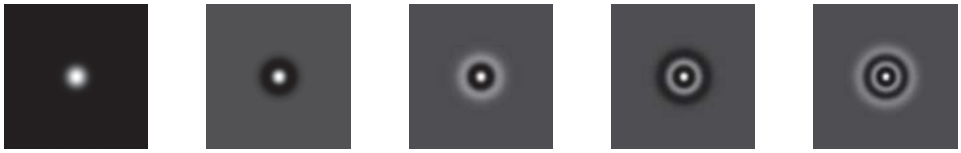

Figure 3.2: The first 5 channels of Laguerre-Gauss function for signal diameter = 2 mm

3.4 Results

The Hotelling observer implements the optimal linear discriminant. The correlation between each pairs of channels of the Hotelling observer is calculated for all projection angles. As a result, the relationship between each angle and channel pair increases the information content of the covariance matrix and the observer's ability to discriminate between signal-present and signal-absent cases. Figure 3.3 shows the cross correlation between all pairs of Hotelling channels over 360 degrees. With our problem set-up, the covariance matrix is statistically stationary in the angle variable, so only one angle is needed in these plots.

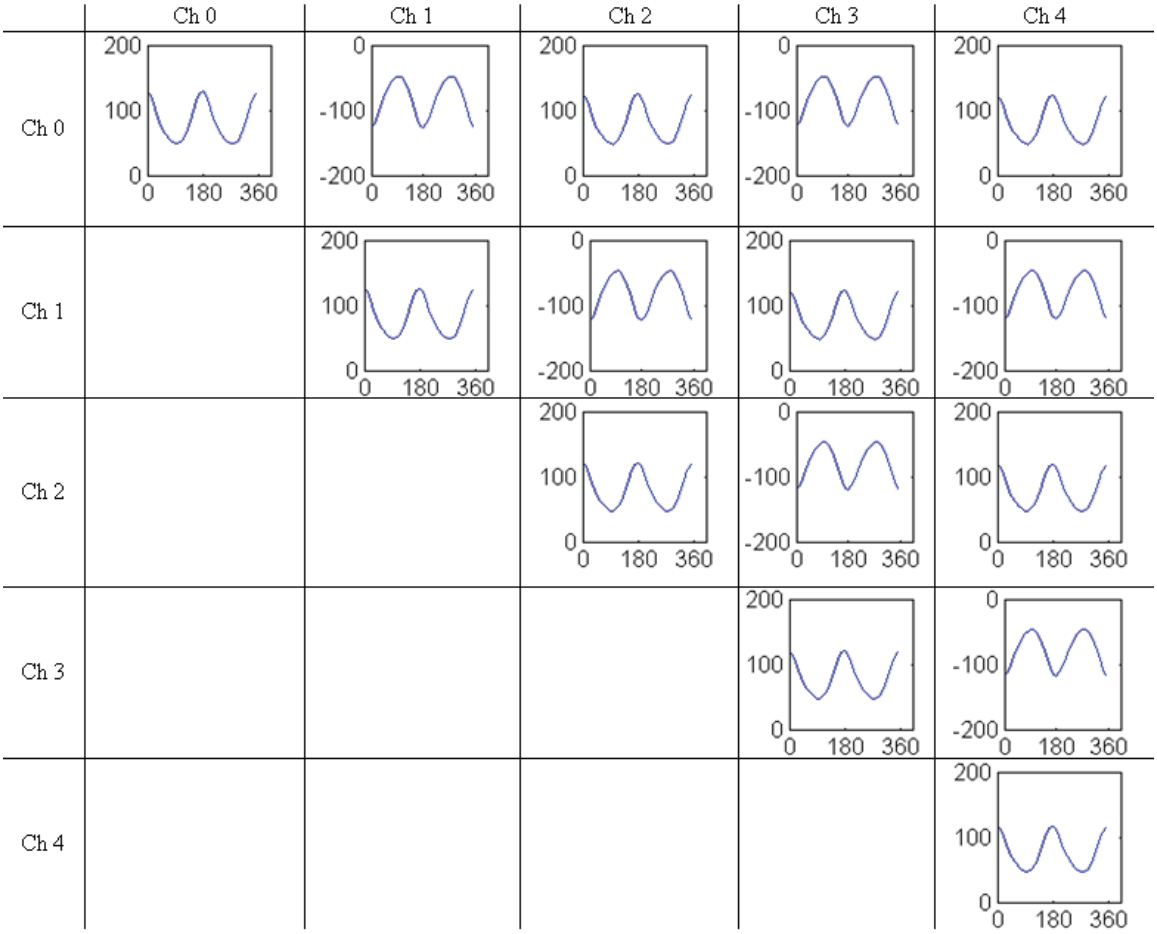

Figure 3.3: covariance values between channel pairs over projection angles

There is a linear relationship between the contrast of the signal at the detector and the SNR, so a contrast-detail diagram can be calculated for a fixed SNR value. The variables considered here are $\bar{k}$, $\overline{N}_0$, σ_{read}, the number of pixels in the detector, and the type of background (i.e. uniform vs. random). Figure 3.4 shows the relationship between the variables considered in this study. The contrast vs. detail diagrams were displayed in log-log scale to show that for a fixed SNR value, the contrast required to detect the signal increases as the signal size decreases. As expected, $\overline{N}_0$, σ_{read}, and $\bar{k}$ are big factors that contribute to the performance of the detector as shown in Fig. 3.4a 3.4b 3.4c. The figures showed that an increase in $\overline{N}_0$ and $\bar{k}$ provided better detector performance while σ_{read} decreased performance. Figure 3.4d

showed that for a fixed incident $\overline{N}_0$ per detector area, the performance decreased slightly with increased number of detector pixels. Note that for all of the results, we did not see a point where the slope of the contrast-detail diagram transitioned from linear slope to asymptotic slope. According to Wagner and Brown (Wagner et al., 1979) this transition should occur when the signal size is near the spatial resolution limit of the detector. We did not observe a significant change in the slope when signal sizes reached the detector pixel size. A similar pattern was also noticed in Sain's (Sain and Barrett, 2003) modular gamma camera experiment where the channelized Hotelling observer was also employed with Laguerre-Gauss templates. Further evaluations are needed to verify this anomaly.

3.5 Conclusions

Using the channelized Hotelling observer on raw projection data over CT projection angles, we have shown that, at a fixed observer SNR, the contrast required to detect a signal increases dramatically as the signal size decreases. The contrast-detail diagram was presented for different variables including number of incident x-ray photons per pixel, read noise of the camera, the number of photoelectrons per pixel collected by the detector, the number of pixels in the detector and the type background (flat vs. random background). We have shown that this method uses the angle correlation information in the data to calculate signal detectability and it can be very useful to optimize the imaging system.

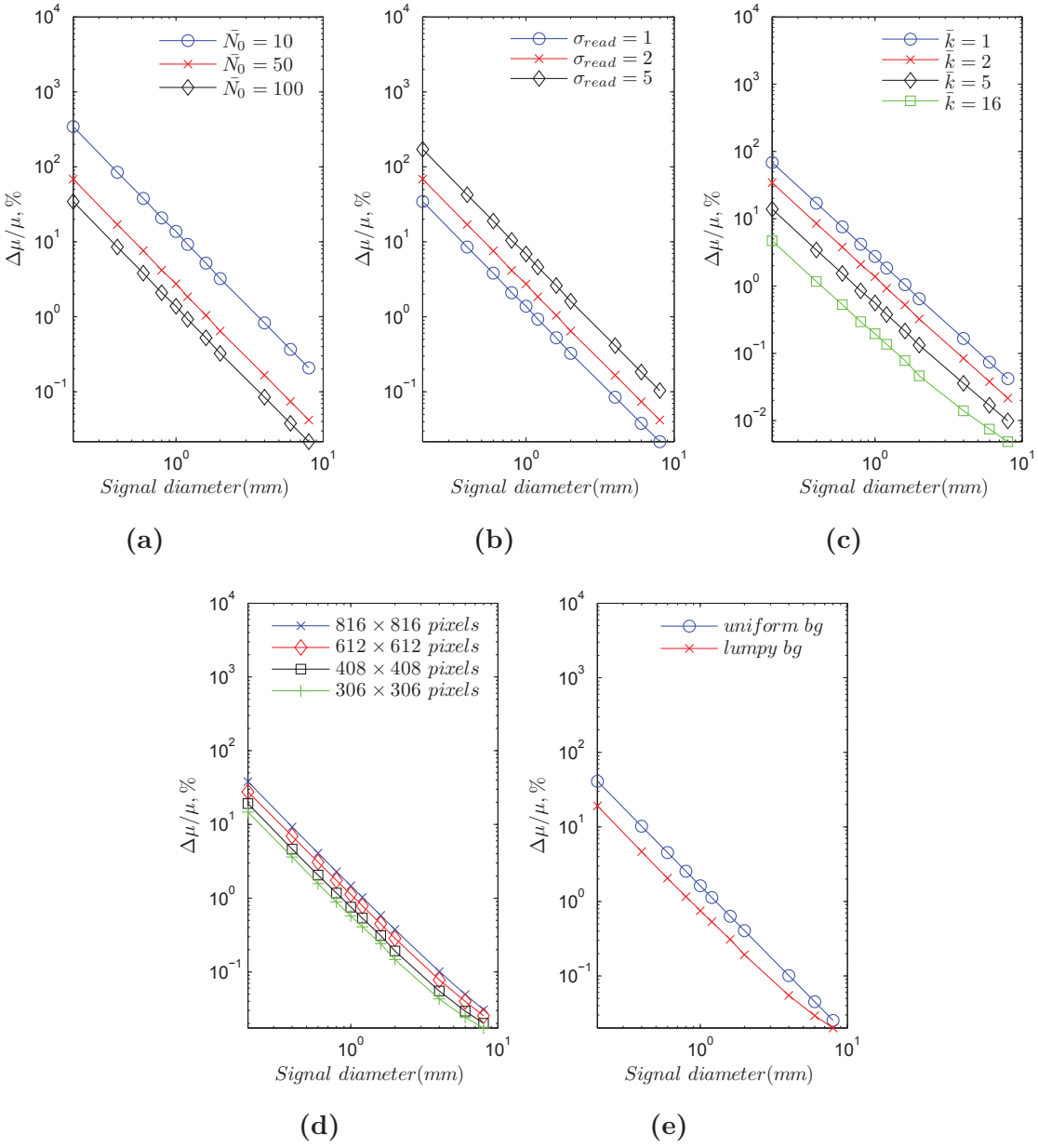

Figure 3.4: Contrast-Detail diagram for SNR = 2 using a detector with 816 × 816 pixels for $\eta = 1$ and $\sigma_{read} = 2$. (a): $\bar{k} = 2$, and $\sigma_{read} = 2$ when $\overline{N}_0$ =10, 50 and 100. (b): $\bar{k} = 2$, and $\overline{N}_0 = 50$ when σ_{read} =1, 2 and 5. (c): $\bar{N}_0 = 50$ and $\sigma_{read} = 2$ when $\bar{k}$ =1, 2, 5 and 16. (d): using 4 detectors with 816 × 816 pixels, 612 × 612 pixels, 408 × 408 pixels, and 306 × 306 pixels when $\sigma_{read} = 2$, $\overline{N}_0 = 50$ photons/0.01 mm^2, and $\bar{k} = 2$. (e): CD diagram for lumpy background and uniform background when $\overline{N}_0 = 50$, σ_{read} =1, and $\bar{k}$ =2

CHAPTER 4

GEOMETRICAL CALIBRATION OF THE CT SYSTEM

4.1 Background

The geometry of the computed tomography system can be described using a set of global parameters. These parameters are crucial for the reconstruction algorithm in order to provide the best object resolution. Since it is impossible to know precisely the geometry of the system after assembly, a calibration method is needed in order to calculate these system parameters and to account for misalignment of the system prior to image reconstruction.

In tomography, it is well known that using inaccurate parameters can produce severe artifacts (Li et al., 1994a,b; Wang et al., 1998). Methods for estimating geometrical parameters of tomographic scanners have been investigated by many groups since 1987, starting with Gullberg (Gullberg et al., 1987). Some calibration methods tend to be specific to the 2-dimensional parallel-beam geometry (Azevedo et al., 1990; Busemann-Sokole, 1987); others are only for 2-dimensional fan-beam geometry (Crawford et al., 1988; Gullberg et al., 1987; Hsieh, 1999). In these earlier methods, the overall approach to calibration is to estimate the geometric parameters by first measuring the locations of point objects on the detector and determining the analytic expressions for these point-object locations as functions of the unknown scanner parameters and unknown positions of the point objects. This step provides a set of nonlinear equations, which are then solved using an iterative method such as the Levenberg-Marquard algorithm (Rougee et al., 1993). The downside of this method is that the algorithms rely heavily on a highly nonlinear parameter-estimation problem and are highly sensitive to the initial estimations and the order

in which the parameters are estimated. There are questions of stability and uniqueness of the parameters. It is uncertain if local minima exist or if more than one set of calibration parameters can satisfy these equations. This work was later extended to 3-dimensional cone-beam scanners (Gullberg et al., 1990); however, the degrees of freedom were restricted, and some shift parameters were assumed to be known.

To avoid initialization and convergence problems created by the Levenberg-Marquard algorithm, many authors have proposed methods that employ direct calculations of the system parameters. In 1999, a method was proposed by Bronnikov that required only two 180°-opposed projection images of a circular aperture. Later authors such as Noo et al., Yang et al., and Cho et al. had similar ideas in which they used a set of intermediate equations to describe the projection-orbit data of fiducial markers (Cho et al., 2005; Noo et al., 2000; Yang et al., 2006). The equations proposed by Noo and Yang were slightly different from each other. In Cho's case, they used a rapid prototype printer to create a phantom that contains multiple fiducial markers to produce several sets of rings about the rotation axis so that the phantom does not need to be rotated during data acquisition. However, all of these methods are limited to a restricted set of parameters, usually omitting out-of-plane rotation of the detector. In 2004, Smekal (Smekal et al., 2004) introduced another analytical method to solve for all system parameters except that some parameters are presented together as ratios rather than individual values. The advantage of this method is that it is insensitive to the precise extraction of the phantom point projection location on the detector. In 2008, Panetta and coworkers (Panetta et al., 2008) proposed a new method in which they measured the misalignment parameters of a cone-beam scanner by minimizing a geometry-dependent cost function. This cost function is computed from the projection data of a generic object; hence, no a-priori knowledge of the object shape or position is required. In 2011, Jared Moore used maximum-likelihood expectation-maximization (MLEM) algorithm to estimate all system parameters by calculating the projection of a known phantom at two 90°-opposed angles.

In the next section, we will describe the calibration method that was used for the prototype x-ray CT system. We will first define the global coordinate system, then we will describe the steps and methods that were used to find all system calibration parameters.

4.2 Defining Geometric Parameters

A global coordinate system is used to describe the scan geometry of the CT system, and a local coordinate axis is later used to describe the points on the misaligned detector. The z-axis is defined as the rotation axis of the object and is set by the rotation stage; the y-axis is defined as a perpendicular line to the z-axis. It passes through the x-ray source and through the ideal x-ray screen plane and camera sensor plane, where both are ideal in the sense that they are perpendicular to the y-axis. The y-axis is also referred to as the optical axis of the system. The x-axis is defined as a line that is perpendicular to both the y-axis and z-axis. Fig. 4.1a shows the global coordinate system with the ideal x-ray screen plane and ideal camera sensor plane.

When we define the global coordinate system, we have assumed that the x-ray source is infinitesimally small and does not change with the tube current or voltage. In reality, the x-ray focal spot has a finite size as shown in Chapter 2. Its size increases with both kVp and mAs. Knowing that the size is finite and changing, we still made this assumption because the calibration method is insensitive to the focal spot size change. In addition, we can apply the calibration parameters obtained at one x-ray tube setting to other techniques (i.e. different mAs).

Next, we need to choose a set of geometric parameters that can be used to define the CT system. These parameters will be used later in the reconstruction algorithm. Although each component in the system can potentially have up to six degrees of freedom, it is not always necessary to treat each component individually and to use all six variables for every component. Instead, we can define a smaller set of

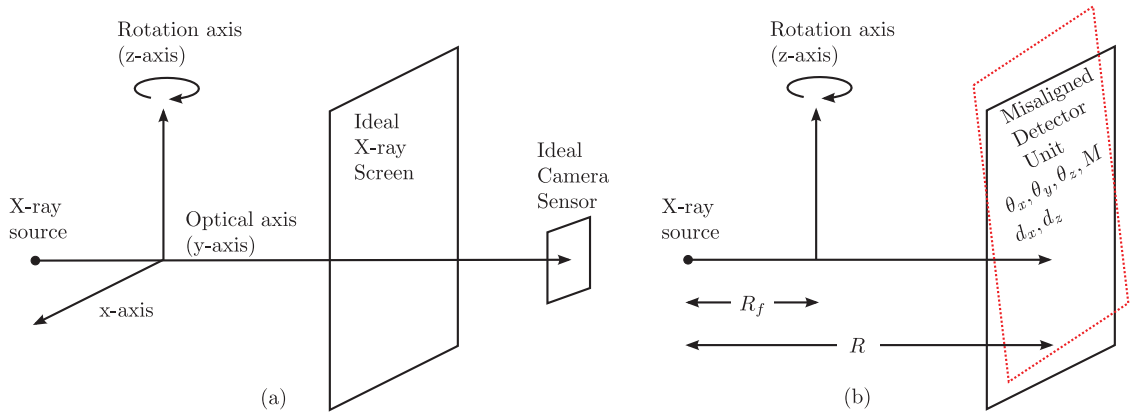

Figure 4.1: (a): The global coordinate system. (b): The eight global parameters that are used to describe the CT system, where the ideal x-ray screen and ideal camera sensor are treated as one unit and are described by one set of global misalignment position and orientation parameters $(d_x, d_z, \theta_x, \theta_y, \theta_z)$ with one additional optical magnification factor M that is used to scale down the x-ray screen onto the camera sensor by the lens. The distance between the x-ray source and the ideal x-ray screen is defined as R, and the distance between the x-ray source and the rotation axis is R_f.

parameters that summarizes the overall geometry of the system by making some simple assumptions. The first assumption is that the lens focuses every point on the x-ray screen within the lens' field-of-view (FOV) onto the camera sensor. We made this assumption because we expect the lens to be well corrected for distortion, at least within the center of FOV. Since the lens is designed for a full-frame sensor, distortion on a smaller sensor, such as the Andor Neo is minimum. In addition, we use only the center part of the image for calibration, therefore we have ignored any distortion in image by the lens at the outer edges. This condition eliminates any misalignment between the x-ray screen, the lens, and the camera. As a result, we can describe the misalignment of these three components as one detector unit. In practice, we cannot change the alignment between the lens and camera as they are fitted together using a mechanical mount (Nikon F-mount), and we have not noticed any distortion in the calibration images we have taken using the Andor Neo camera. In addition, the commercial Nikon lens has a large depth of focus, which depends on the F-number, however we did not perceive any defocus within the field

of view on the phosphor screen for the camera positions that we have used.

We have also assumed that the x-ray screen is large enough that any lateral shift in its plane does not change the final image on the camera sensor. These assumptions allow us to decrease the set of calibration parameters to eight values.

Fig. 4.1b shows the eight global parameters that are used to describe the CT system. The detector unit is defined as the combination of the x-ray screen, lens and camera, where the x-ray screen plane is conjugate to the camera sensor plane with a magnification factor M set by the lens. The optical axis passes through the center of the x-ray unit and is defined as the center of the camera sensor magnified back onto the x-ray screen. The eight global parameters are: R, R_f, d_x, d_z, θ_x, θ_y, θ_z and M, where R is the distance between the x-ray source and the detector unit, R_f is the distance between the x-ray source and the rotation axis, d_x and d_z are the position misalignments of the center of the detector unit away from the optical axis in either x and z direction respectively, and θ_x, θ_y, and θ_z are the angular rotations of the detector unit about its respective axes. These essential parameters are used in the reconstruction algorithm described later in Chapter 5.

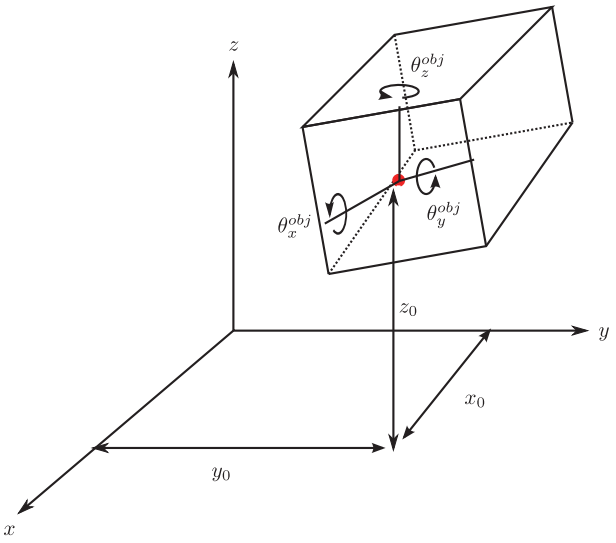

Figure 4.2: The six nuisance parameters that describe the misalignment position and orientation of the phantom.

In order to estimate all of the global parameters, we needed to add an additional six parameters to complete our calculation. These are called nuisance parameters and, just as the name indicates, these parameters are not necessary to define the geometry of the system, however, the calibration method we used required them to be estimated in order to complete our calculation. These six nuisance parameters are used to describe the position and orientation of the calibration phantom $(x_0, y_0, z_0, \theta_x^{obj}, \theta_y^{obj}, \theta_z^{obj})$ shown in Fig. 4.2.

4.3 Calibration Method

We have employed three steps in order to compute all of the calibration and nuisance parameters, as follows:

1. Calculate the lens optical magnification power, M.
2. Calculate the majority of global parameters using Smekal's method, which includes $\theta_x, \theta_y, \theta_z, d_x, d_z$, and R.
3. Calculate the nuisance parameters $(x_0, y_0, z_0, \theta_x^{obj}, \theta_y^{obj}, \theta_z^{obj})$ and find R_f.

4.3.1 Calculate lens magnification power

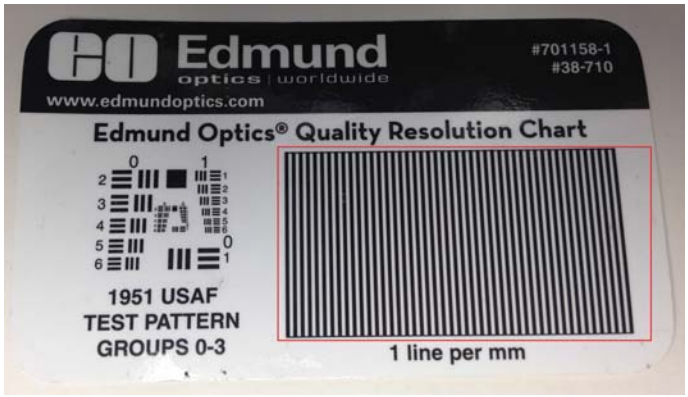

Figure 4.3: Resolution chart from Edmund Optics.

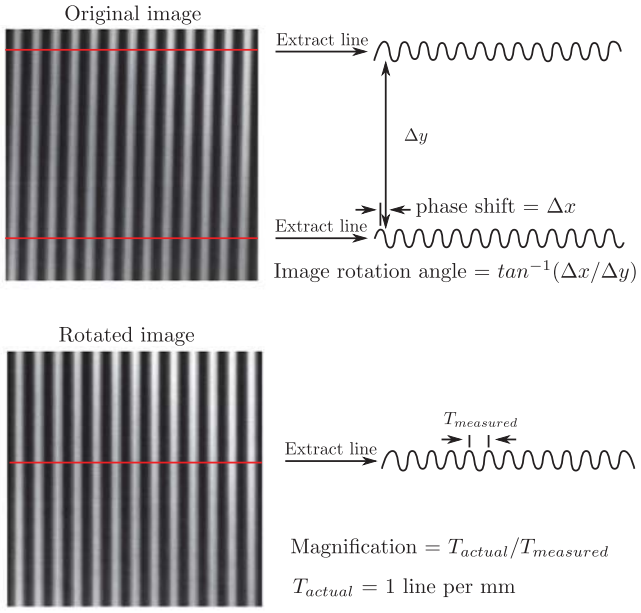

Figure 4.4: Procedure for obtaining the optical magnification factor (M) using Edmund Optics' resolution chart.

The optical magnification can be measured under white light by placing an item of a known size at the phosphor screen and measuring the image size of the object scaled on the sensor. In practice, we used a resolution chart purchased from Edmund Optics, shown in Fig. 4.3 and focused our camera on the 1 line per mm bar section of the resolution chart. For each row of the image, we fitted the data to the first order of the Fourier series using the "fit()" function in MATLAB. The phase shift of each row of the image corresponds to the bar target rotation. Once the image is corrected for rotation by use "imrotate()" function, we can then average the image over rows and calculate the period of the bar target. This procedure is illustrated in Fig. 4.4.

4.3.2 Calculate global parameters

In order to find the global system parameters, we opted to use Smekal's calibration method (Smekal et al., 2004) that derives explicit analytic expressions for a set of

fiducial markers. This method does not require precise knowledge of the marker's spatial location inside the phantom; rather, it uses the marker's projection orbit on a misaligned detector for the calculation. These orbits are first analyzed using Fourier components with low spatial frequency. The parameters are then calculated based on each individual point marker from the Fourier coefficients by using a series of equations. The averages of the parameters over the set of fiducial markers are used as the final result. The corresponding standard deviations for each parameter are used as error bars in the estimation.

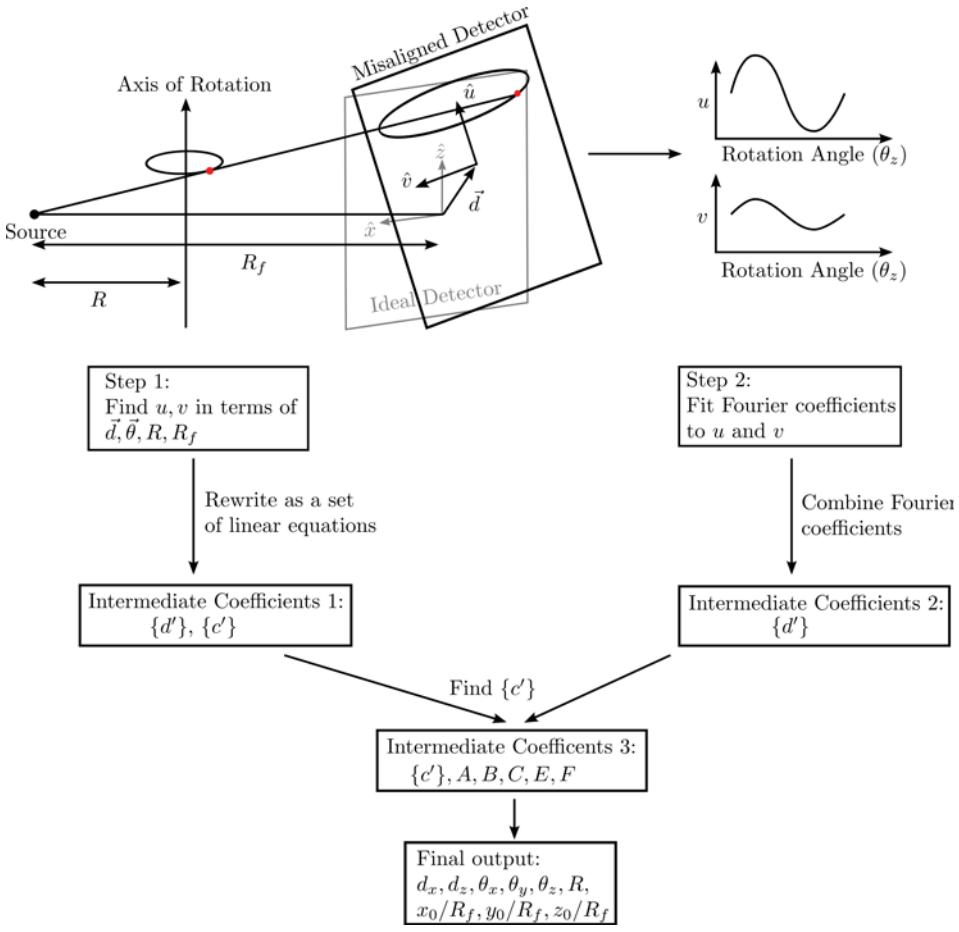

Figure 4.5: Calibration steps to calculate global parameters.

In this section, we will focus on the main ideas and equations that were used to calculate the calibration parameters. Detailed derivations are given in the pa-

per (Smekal et al., 2004). The system geometry and a graphical representation of the method are shown in Fig. 4.5, where the global coordinate system and system parameters are defined similar to those given in Fig. 4.1. The main idea behind Smekal's method is to first describe the relationship between the point markers and the projection orbit by a set of linear equations based on the rotation matrix of the misaligned detector (step 1). This set of equations is a function of the system parameters and initial marker positions. Next, the projection orbit is parameterized using a set of Fourier series coefficients (step 2). Then, it is a matter of finding the relationship between the Fourier series coefficients and the linear equations through various intermediate coefficients in order to disentangle the system parameters while eliminating dependencies on the initial marker positions.

In step 1, we can describe the projection orbits of point markers on the misaligned detector using the system parameters. Shown in Fig. 4.5, a point on the true misaligned detector (x', y', z'), with detector coordinates (u, v), can be written as,

$$\begin{aligned} u\hat{u} + v\hat{v} + \vec{d} &= u\mathbf{O}\hat{x} + v\mathbf{O}\hat{z} + \vec{d} \\ &= x'\hat{x} + (y' - R + R_f)\hat{y} + z'\hat{z}, \end{aligned} \tag{4.1}$$

where $\vec{d} = d_x\hat{x} + d_y\hat{y} + d_z\hat{z}$ is the distance between the center of the ideal detector and the misaligned detector, $\mathbf{O}$ is a 3×3 rotation matrix that maps the vectors $(\hat{x}, \hat{z})$ to $(\hat{u}, \hat{v})$ using $\theta_x, \theta_y, \theta_z$ shown in Eq. 4.2.

$$\mathbf{O} = \begin{pmatrix} cos\,\theta_y\, cos\,\theta_z - sin\,\theta_y\, sin\,\theta_x\, sin\,\theta_z & -cos\,\theta_x\, sin\,\theta_z & -cos\,\theta_z\, sin\,\theta_y - cos\,\theta_y\, sin\,\theta_x\, sin\,\theta_z \\ cos\,\theta_z\, sin\,\theta_y\, sin\,\theta_x + cos\,\theta_y \text{ sin } \theta_z & cos\,\theta_x cos\,\theta_z & cos\,\theta_y\, cos\,\theta_z\, sin\,\theta_x - sin\,\theta_y\, sin\,\theta_z \\ cos\,\theta_x\, sin\,\theta_y & -sin\,\theta_x & cos\,\theta_y\, cos\,\theta_x \end{pmatrix} \tag{4.2}$$

Generally speaking, it is not ideal to describe the point (u, v) using the coordinate (x', y', z'), i.e. $y' \neq R - R_f$. Instead, we can describe the point using the ideal coordinate (u^{id}, v^{id}) where this perfect alignment counter part (i.e. $y' = R - R_f$) connects the rays from the x-ray source, through the focus, and to the points (x', y', z')

using the equation,

$$x' = \frac{y' + R_f}{R} u^{id}, \quad z' = \frac{y' + R_f}{R} v^{id}. \tag{4.3}$$

Inserting Eq. 4.3 into Eq. 4.1, we can obtain the ideal orbit in terms of the real orbit on the misaligned detector as

$$\begin{pmatrix} u^{id} \\ v^{id} \end{pmatrix} = \frac{R}{R'_y + o_{21}u + o_{23}v} \left(\begin{pmatrix} o_{11} & o_{13} \\ o_{31} & o_{33} \end{pmatrix} \begin{pmatrix} u \\ v \end{pmatrix} + \begin{pmatrix} d_x \\ d_z \end{pmatrix} \right) \tag{4.4}$$

Thus, the inverse relationship for the real orbit in terms of the ideal orbit for Step 1 can be obtained by using some matrix manipulations, and the result is as follows:

$$\begin{pmatrix} u \\ v \end{pmatrix} = \frac{1}{det\,\mathbf{Q}} \begin{pmatrix} o_{33} - o_{23}v^{id}/R & -(o_{13} - o_{23}u^{id}/R \\ -(o_{31} - o_{21}v^{id}/R) & o_{11} - o_{21}u^{id}/R \end{pmatrix} \times \begin{pmatrix} u^{id'} - d_x \\ v^{id'} - d_z \end{pmatrix} \tag{4.5}$$

where,

$$\begin{pmatrix} u^{id'} \\ v^{id'} \end{pmatrix} = \frac{R'_y}{R} \begin{pmatrix} u^{id} \\ v^{id} \end{pmatrix} \tag{4.6}$$

and the determinant in Eq. 4.5 is given as,

$$\begin{aligned} det\,\mathbf{Q} =& (o_{11} - o_{21}u^{id}/R)(o_{33} - o_{23}v^{id}/R) \\ & -(o_{13} - o_{23}u^{id}/R)(o_{31} - o_{21}v^{id}/R). \end{aligned} \tag{4.7}$$

In Step 2, we need to parameterize the point marker's projection orbit on the misaligned detector using the Fourier coefficients. We can write the discrete real Fourier series as follows,

$$u_n = \frac{U_0}{2} + \sum_{k=1}^{N/2-1} (U_k \cos(k\alpha_n)) + \tilde{U}_k \sin(k\alpha_n) + (-1)^{(n-1)} \frac{U_{N/2}}{2}, \tag{4.8}$$

with similar expressions for v_n. The real Fourier coefficients are given by:

$$\begin{aligned} U_k =& \frac{2}{N} \sum_{n=1}^{N} u_n \cos(k\alpha_n), \quad k = 0, ..., N/2, \\ \tilde{U}_k =& \frac{2}{N} \sum_{n=1}^{N} u_n \sin(k\alpha_n), \quad k = 1, ..., N/2 - 1 \end{aligned} \tag{4.9}$$

and analogously for V_k and $\tilde{V}_k$. Only the first three Fourier components were needed in the misalignment calculation. Thus, the method is insensitive to high frequency fluctuations and uncertainties that stem from marker-point extraction between different projection angles. These Fourier coefficients and the results from Step 1 are used to calculate the final system parameters by going through some intermediate equations. These equations are shown in Appendix X.

The result of Smekal's method calculates ten parameters. These are the detector rotation misalignment, θ_x,θ_y,θ_z, detector position misalignment, d_x,d_z, R, and R'_y, where $R'_y = R + d_y$. This method also provides the object marker initial location with respect to R_f, i.e., x_0/R_f, y_0/R_f, z_0/R_f. Unfortunately, R_f and marker initial locations are presented together and can no longer be separated using Smekal's calibration method.

4.3.3 Calculating the nuisance parameters and R_f

In order to calculate R_f, we have opted to use an iterative search method. Numerous search algorithms can be used to look for a parameter vector that resides in a multi-dimensional space. We have opted to use the contracting-grid algorithm that allows the identification of a function's minimum in a fixed number of iterations using a fixed grid size (Hesterman et al., 2010). Along this search process for R_f, the values for six nuisance parameters were also calculated.

The contracting grid algorithm is based on maximum-likelihood estimation. The maximum-likelihood method can generally be formulated as a search over parameter space using (Barrett and Myers, 2004),

$$\hat{\boldsymbol{\theta}} = \arg\max_{\theta} \ \lambda(\boldsymbol{\theta}|\mathbf{g}) = \arg\max_{\theta} \ \mathrm{pr}(\mathbf{g}|\boldsymbol{\theta}), \tag{4.10}$$

where $\boldsymbol{\theta}$ is a vector composed of parameters of interest, $\mathbf{g}$ is the data vector, λ is the likelihood of observing $\mathbf{g}$, and $\hat{\boldsymbol{\theta}}$ is a vector of estimated parameters. The data vector $\mathbf{g}$ is composed of the pixel values in the image for all projection angles. If

the noise in the detector pixels are independent and identically distributed, where each pixel can be modeled using a zero-mean Gaussian function, then Eq. 4.10 is reduced to

$$\arg\min_{\theta} \|\mathbf{g} - \bar{\mathbf{g}}(\boldsymbol{\theta})\|^2, \tag{4.11}$$

where $\bar{\mathbf{g}}(\boldsymbol{\theta})$ is the mean of the image data vector without noise. Thus the maximum-likelihood solution to Eq. 4.10 is to search over $\boldsymbol{\theta}$ in order to minimize the least-squares difference between $\mathbf{g}$ and $\bar{\mathbf{g}}$. The image data vector without noise is calculated using the imaging equation,

$$\bar{\mathbf{g}}(\boldsymbol{\theta}) = \mathbf{H}(\boldsymbol{\theta})\bar{\mathbf{f}}(\boldsymbol{\theta}), \tag{4.12}$$

where $\mathbf{H}$ is the imaging system matrix. This means $\mathbf{H}$, $\bar{\mathbf{f}}$, and $\bar{\mathbf{g}}$ must be re-calculated each time a new $\boldsymbol{\theta}$ is used in the search algorithm.

Unfortunately this method is not viable due to computation constraints. For example, the projection of an phantom object was calculated in simulation with 64^3 voxels over 360 degrees at 2-degree increment, where each projection image was 1024^2 pixels. This computation took over 30 seconds in CUDA. Even if only 2 grids were used per parameter value, this means each contracting-grid iteration would require the same calculation to be repeated 128 times, totaling over an hour per iteration. In an actual experiment where the the number of object voxels and parameter grids are required to be much larger, the calibration step would take too long to be realistic. Instead, we have decided to replace $\bar{\mathbf{f}}(\boldsymbol{\theta})$ by a set of coordinate locations for each fiducial markers in the global coordinate system $(\bar{x}_i, \bar{y}_i, \bar{z}_i)$. The imaging matrix, $\mathbf{H}$, can be replaced by first applying a rotation and translation matrix onto each marker's position to incorporate the position and orientation misalignment of the object, then use Eq. 4.3-4.7 to obtain $\bar{u}_i$ and $\bar{v}_i$, which are the projection positions of the markers on the misaligned detector. These are used in place of $\bar{\mathbf{g}}(\boldsymbol{\theta})$. The image data, $\mathbf{g}$ is replaced by the coordinates of the fiducial markers obtained from

image data, $(\hat{u}_i, \hat{v}_i)$, which are acquired via centroid estimation using,

$$\hat{u}_i = \frac{\sum_{n=1}^{N} g_{in} u_{in}}{\sum_{n=1}^{N_i} g_{in}}, \qquad \hat{v}_i = \frac{\sum_{n=1}^{N} g_{in} v_{in}}{\sum_{n=1}^{N_i} g_{in}}, \tag{4.13}$$

where g_{in} is the pixel value at location u_{in} for the i^{th} fiducial marker. The contracting-grid algorithm was applied to search over $\boldsymbol{\theta}$ by minimizing the least-squares difference, d, between $\bar{u}_i$, $\bar{v}_i$ and u_i, v_i using

$$d = \sum_i \sqrt{(\bar{u}_i - \hat{u}_i)^2 + (\bar{v}_i - \hat{v}_i)^2}. \tag{4.14}$$

We note that by reducing data size and performing centroid estimation, the noise models on $\hat{u}_i$ and $\hat{v}_i$ are no longer zero-mean Gaussian functions.

The parameter grid used in the algorithm is a discrete set of numbers each centered about the parameter value. The initial spacing within each parameter grid is $\Delta\theta^0 = D_i/(N-1)$, where D_i is the grid size and N is the number of grid points used for each parameter, which we have kept as a constant value. Since we can physically measure each parameter in the beginning, at least within a few millimeters or degrees, the grids are centered about these initial values. We have set the grid size, D_i for distance measurements to be ± 5 mm and orientation measurements to be $\pm 3°$. We have chosen to set the number of grid points, N, to be 4 in order to limit the amount of time used in each iteration. In the subsequent iterations, the grid size for the k^{th} iteration contracts to a smaller size using

$$\Delta\theta^k = \frac{\Delta\theta^{k-1}}{\gamma}, \tag{4.15}$$

where γ is the contracting rate, and a new set of parameters are chosen as the new grid centers. The contracting-grid algorithm can broken down into five steps:

1. For each parameter θ_i, create a region of physically reasonable grid size.

2. Use Eq. 4.11 and calculate the least-squared results of all parameter grid combinations.

3. Find the set of parameters that generated the lowest least-squared result. This is the starting point for the next iteration.

4. Contract the grid size for centered about the parameters from the previous step using Eq. 4.15.

5. Repeat Steps 2-4 until the algorithm reaches a preset number of iterations.

Detailed information regarding the contracting-grid search algorithm is given in the paper by Jacob Y. Hesterman (Hesterman et al., 2010).

Through experimentation, we have found that it is more efficient to first obtain a rough estimate of the parameters, R_f, θ_z^{obj}, θ_x^{obj}, and θ_y^{obj} before using the contracting-grid algorithm. A rough estimation of R_f can be found by using the vertical separation between the point markers on the projection image (Δz_0) of a known phantom and applying it to the values $\Delta z_0/R_f$ calculated from the previous section. θ_x^{obj} is the initial rotation orientation of the point markers about the z-axis, changing this value does not affect the overall projection locations of the point markers but it does greatly contribute to the least-squares sum of the contracting-grid algorithm. Therefore, we have approximated its value in order to minimize the search duration later. Finally, the values for θ_x^{obj} and θ_y^{obj} are iterated over 360° to obtain the initial parameters.

4.3.4 Calibration results

Figure 4.6 shows the projections of the ball bearings from experiment vs. the projections of point markers using the calibration parameters. We have tested various number of grid points ranging from 2 to 10 and contracting rate from 1.05 to 1.3. Larger grid size requires more time to compute while slower contracting rate takes longer to converge. Through experimentation, we have settled to use 100 contracting-grid iterations with a 4 grid points for each parameter at a contracting rate of 1.05.

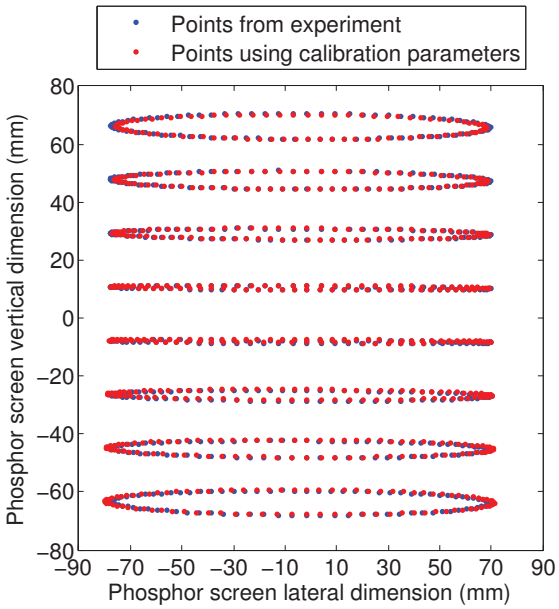

Figure 4.6: Projection of the ball bearings from experiment vs. the projection of the point markers using the calibration parameters after 100 iterations with a grid size of 4 and a contracting rate of 1.05.

Table 4.3.4 shows the calibration results of the CT system. Note that R_f is calculated using the contracting-grid algorithm without using a noise model. We have obtained the standard deviation on R_f by plotting the mean-squared error between experimental and calibration result for various R_f values centered at the R_f found via calibration. Shown in Fig. 4.7, we can see that R_f can deviate ± 1 mm to still remain within %0.5 of the mean-squared error obtained with calibration.

The most important angular measurement is θ_y because it accounts for the image rotation about the optical axis. Errors in this parameter can result in severe artifacts in the reconstruction image. Both θ_x and θ_z are less important; in fact, these values were assumed to be zero in some calibration methods (Cho et al., 2005; Noo et al., 2000; Yang et al., 2006).

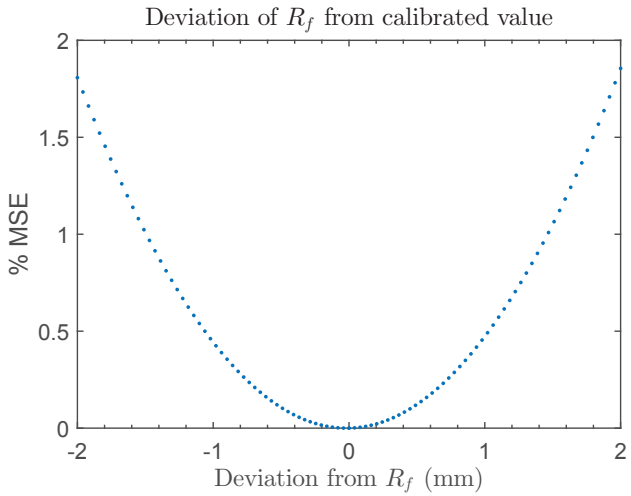

Figure 4.7: The deviation of R_f against the mean-squared error obtained using results obtained from calibration.

4.4 Calibration Phantom

The phantom used in the calibration process was designed in SolidWorks and printed using the rapid prototype machine at the Center for Gamma-Ray Imaging (CGRI). The phantom is composed of two separate pieces: a large bracket that is mounted on the rotation stage and a smaller insert where a number of ball bearings and sizes can be attached. The bracket and multiple inserts are shown in Fig. 4.8.

The bracket is designed so that the center of the ball bearings on the inserts is 60 mm from the center of the rotation axis on the bracket. The smaller insert has a conical end so it is easy to align the vertical axis of the markers against the bracket holder. The ball bearings are made out of stainless steel and are purchased from McMaster-Carr. Three different bearing sizes (1/16″, 1/8″, 3/16″ and 1/4″) were purchased and tested. Through experiments we have found that the 1/8″ ball bearings worked the best.

Parameter	Value	Standard Deviation
R	1106.3 (mm)	2.43 (mm)
R_f	900.7 (mm)	1 (mm)
d_x	4.01 (mm)	0.0028 (mm)
d_z	-1.40 (mm)	0.10 (mm)
θ_x	-0.019 (radians)	1.0743 (radians)
θ_y	0.0039 (radians)	0.0003 (radians)
θ_z	-0.0047 (radians)	0.0089 (radians)
M	13.1	0.24

Table 4.1: Calibration Results

4.4.1 Extract phantom marker locations

In order to use the calibration method described in Section 4.3, we must be able to extract the 2-dimensional coordinate location of the point markers on the detector using the phantom ball bearing projection images. The raw projection image at one angle is shown in Fig. 4.9.

Upon close inspection, although we can see the ball bearings clearly, the image is littered with small clusters of high-value pixels, also shown in Fig. 4.9. These clusters of bright pixels are the result of direct x-ray interactions, where the x-ray energies are deposited inside the detector, resulting in high detector values. They cannot be completely eliminated even after we carefully shield the camera with lead plates. The locations of these clusters are random and vary from image to image; typically higher x-ray tube energies (>60 kVp) produce more clusters than lower x-ray tube energies. However, we wish to calibrate using higher x-ray tube energies because while the projection of the steel ball bearings will remain dark, the projection of the plastic phantom material will be lighter. The higher contrast difference between the two materials allows us to extract the ball bearing location more easily without having to repeat the same experiment again, without the ball-

(a) **(b)**

Figure 4.8: (a) Calibration phantom bracket, and (b) inserts with different ball bearings.

bearings. Fortunately, we can eliminate the majority of these high-value clusters by thresholding the entire image. The result is an intermediate image with the majority of phantom structures removed, as well as the majority of these high-value clusters, leaving only the clusters of ball bearing projections and other smaller clusters left over from the phantom structures. Unfortunately, at this stage, we cannot simply use well-known clustering algorithms such as *k-means* to extract the centroid locations. This is because the algorithm require us to fix the number of clusters in the image. While we know the number of ball bearing clusters we need to identify, we do not know the number of smaller clusters left over after thresholding since it varies in every image. Instead, we use a slightly more tedious method to search for each ball bearing projection cluster. This method can be summarized by the following steps:

1. Sort all points in the main image array by their y-coordinate.

2. Retrieve the first point's x and y coordinate and set it as the center of the cluster.

3. Find the next point that is closest to the first point.

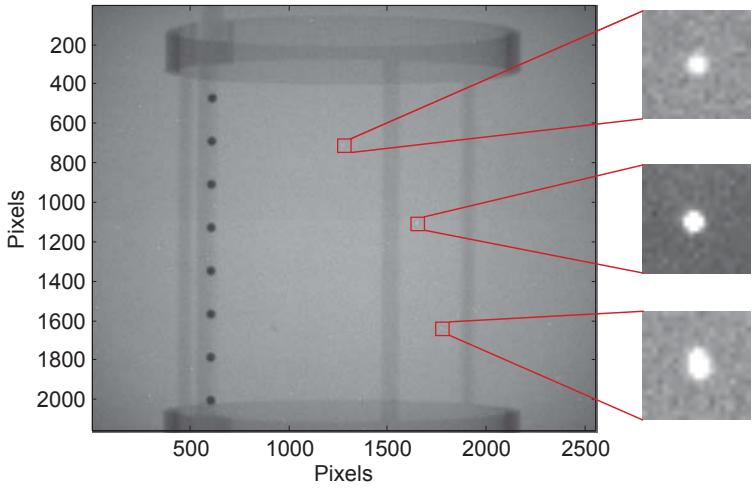

Figure 4.9: Projection of the calibration phantom at one angle. The image taken used 100 kV x-ray at 200 μA with a 2 second exposure time.

4. Re-calculate the center cluster coordinate using the neighboring point by averaging the x and y coordinate of the points.

5. Iterate through all points and repeat Step 3-4 until all points that are close to each other have been approximately identified and calculate a mean cluster coordinate using these identified points.

6. Recalculate the center coordinate for the cluster using all of the points identified in Step 5, then iterate through all points again in the main image array to ensure that no points for this cluster were missed.

7. Reject this cluster if it is too small in terms of size or the number of points.

8. Record the cluster center coordinate and remove all points from this cluster from the main image array.

9. Repeat Step 2-8 until the image cluster size reaches zero.

The cluster center is simply the mean of the x-coordinate and y-coordinate of the cluster points. The main idea for this method is to assume that points close to each other belong in the same cluster. This is the reasoning behind Step 1, where we

needed to first sort all points by their coordinate position. We reason that, after all points are sorted, then if we iteratively go through all points in the main array, all points that are within a cluster should be very close to each other. We use the mean cluster point as a reference to determine whether the next point should be included in the current cluster. The criterion for this determination is distance. If the distance between the current cluster center and the next point is close, then we classify the next point as a cluster point and repeat until we have searched iteratively through all points in the image array, Step 2-6. The distance used in this method is the approximate image size of the ball bearing measured visually using one calibration image. Once a cluster is identified, we look through all of the points in the array once more to ensure that no points that should have been included in this cluster were not over looked(Step 6). Once this cluster is identified, we classify this cluster as either a ball bearing projection cluster, or a background noise cluster based on how many points are in this cluster and the cluster physical size (step 7). The limit on the number of points and size limit were approximated using one calibration image by visual inspection. A secondary array maps the points in the image array to the newly identified cluster; thus, these points are not used when the algorithm repeats Step 2-8 in search for a new cluster. Since this method iterates through the main image array twice for each cluster, outwardly it can be a very slow method. However, since we remove all points in the cluster each time a cluster is identified, the method speeds up as more clusters are found. In fact, once the raw projection image is thresholded (before using this method), we are left with only approximately 10,000 - 30,000 points, which is very manageable size using MATLAB. In the end, this method only takes about 1-2 seconds to identify and calculate the centroid coordinates in each raw calibration image. The calibration code can be downloaded from the git public repository: `https://bitbucket.org/hxfan/matlab_calc`.

Figure 4.10 provides a graphical description of the clustering algorithm described in this section. In this figure, each point represents a point from the projection image after thresholding. The number above each point represents its rank order after the

points are sorted by the coordinate position (y coordinate). The cluster center point is used as a reference to find the next cluster point, and it is recalculated after the next cluster point is identified. Shown in the figure, once the 6$^{\text{th}}$ cluster point is identified, the distance between the center-of-mass point and point 7 exceeds $R_{point\ cluster}$; therefore, points 7 and 8 do not belong to cluster 1 and will not be used to calculate the next cluster center point. Also shown is the cluster center point after point 24 is identified. The distance d_3 between the cluster point point and point 25 exceeds $R_{point\ cluster}$ therefore point 25 is also ruled out and does not belong to cluster 1. Cluster 2 includes points 7, 8, 13, and 14; however, because this cluster is too small so it is classified as noise cluster. Point 25 is also ruled out as belonging to any cluster. Clusters 1 and 3 are classified as ball-bearing projection clusters with corresponding centroid positions.

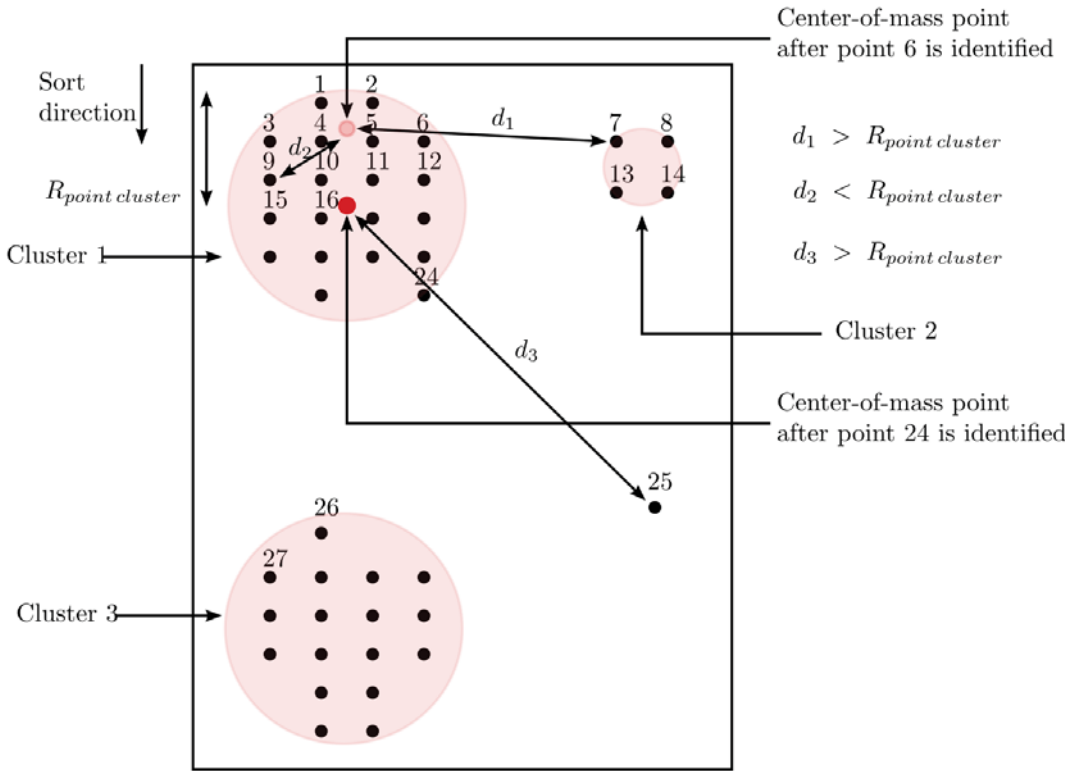

Figure 4.10: A graphical description of the clustering algorithm.

4.5 Summary

In this chapter, we have described the calibration method for the prototype CT system. We began by providing an overview of some of the existing methods for calibrating bench-top x-ray CT systems. Then, we followed by defining the geometry of the system and describing the steps that were taken to extrapolate all 14 parameters of the system. The final results of the system parameters are shown in Section 4.3.4. The last two sections of this chapter describes the physical calibration phantom and the algorithm that were used to extract the ball bearing projection points from raw calibration images.

CHAPTER 5

CT RECONSTRUCTION

The essential goal of any reconstruction is to use the information gathered to estimate the parameters associated with the object. In the case of CT, we use the information gathered on the detector over a range of angles to calculate the x-ray attenuation coefficients of the object voxels. CT systems have evolved tremendously over the years, and reconstruction algorithms have also evolved dramatically to support the various types of systems. There are two general approaches to reconstruction: analytical and iterative. In this chapter, we give a brief overview of these general techniques used for CT reconstruction, followed by an explanation of the method that was used for our system.

The first clinical CT scanner, installed in 1971, was a dedicated brain imager that used a single detector. In 1973, a whole-body CT scanner was introduced (Ulzheimer and Flohr, 2009). Up until 1990, most clinical CT scanners used the fan-beam geometry with axial rotation. In the early 1990s, out of the desire to cover an entire human organ, the first single-slice helical CT scanner was introduced. Ever since, helical geometry has been the main configuration for all clinical CT scanners. In 1996, Elscint was the first to develop a CT system that had two detector rows and could acquire two images slices with every rotation of the gantry. A few years later, General Electric (GE) came out with the first four-slice CT scanner and was quickly followed by all other major CT manufacturers. The term multi-slice CT, also called multi-detector-row CT (MDCT), quickly became the trend with manufacturers pushing for more detector rows, from 16 rows in 2002 (ImPACT, 2002) to 320 slices in late 2007 by both Philips and Toshiba (Ulzheimer and Flohr, 2009). The industry's push for larger volume coverage and faster scan time has fueled the need to develop newer and more efficient reconstruction algorithms.

5.1 Analytic Reconstruction Techniques

The most common method of image reconstruction for the earlier CT scanners was the fan-beam filtered back-projection algorithm. At the heart of the reconstruction algorithm is the Radon transform, which relates a function $f(\mathbf{r})$ to the collection of line integrals of that function $\lambda(p, \phi)$. Shown in Eq. 5.1, the projection line is described using $\mathbf{r} \cdot \hat{\mathbf{n}} = p$, where $\hat{\mathbf{n}}$ is a unit vector making an angle ϕ to the x-axis, shown in Fig. 5.1.

$$\lambda(p, \phi) = \int_{\infty} d^2r \; f(\mathbf{r})\delta(p - \mathbf{r} \cdot \hat{\mathbf{n}}). \tag{5.1}$$

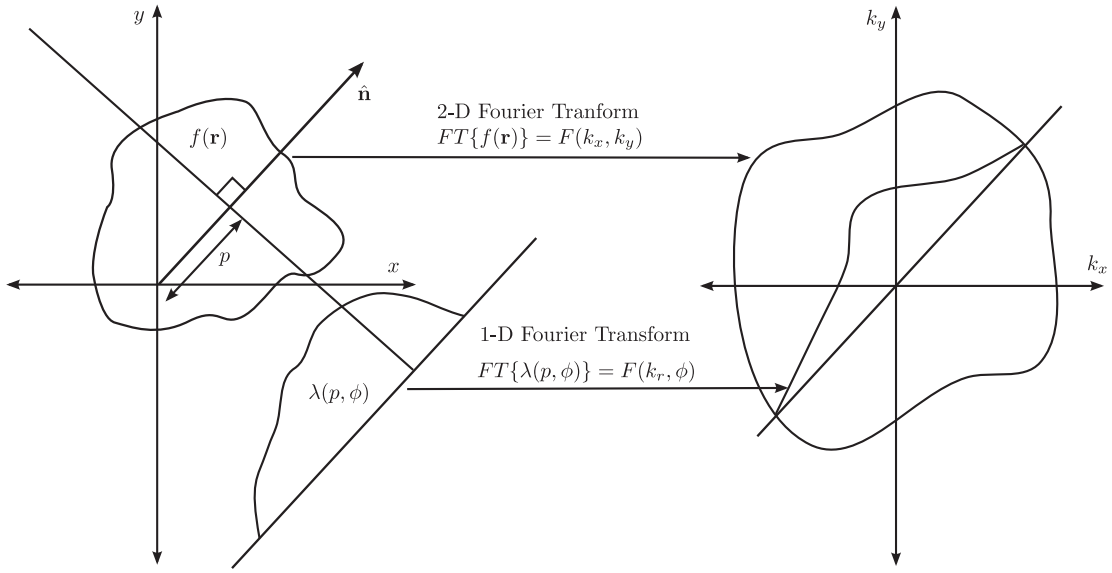

Figure 5.1: The 2D Radon transform of a 2-D object and its Fourier transform.

To invert the Radon transform, the projection data on the detector at each angle go through a Fourier transform. The Fourier transform of the projection data along a projection angle represents the Fourier transform of the object along the same projection angle as seen on the right of Fig. 5.1. The Fourier transformed data are then filtered in the spatial-frequency domain by a ramp filter, then back-projected into object space to reconstruct the original object. This algorithm is also known as the Filtered Back-Projection (FBP). For the fan-beam geometry, typically the

projection data are gathered and rebinned into parallel projection sets before taking the inverse Radon transform to obtain the reconstructed slices.

CT scanning geometries can be divided into two general categories, depending on the targeted region of interest (ROI) within the body. The first category is circular/axial orbit scanning, where the patient remains stationary and the source and detector traces a circle around the patient. This orbit is typically used to image smaller features of the body, such as the brain or the heart. The circular-scanning geometry has the advantage of being very simple and fast, especially when the data acquired must be synchronized with a physiological signal, such as an electrocardiogram (EKG). The most widely used reconstruction algorithm is the Feldkamp-Davis-Kress (FDK) reconstruction (Feldkamp et al., 1984). The algorithm is very similar to the conventional fan-beam reconstruction, but the off-axis rays of the cone beam are weighted by a cosine term in order to approximate them as the 2D fan-beam rays. The FDK algorithm works well when the cone angle is moderate, and many authors have proposed alternative methods to fix and compensate the image slices at the outer edges of the cone beam (Chen, 2003; Hu, 1996; Katsevich, 2003).

The second and the most widely used scanning method is the helical geometry. During data acquisition, the patient bed moves in an axis that is perpendicular to the rotation plane of the gantry so the source and detector traces a helix around the patient. There are two approaches to use the data acquired with helical scan to reconstruct the patient body. These are the approximate and exact reconstruction methods. The most common method to solve this problem is the approximate reconstruction technique derived from the original FDK algorithm and later generalized to spiral scan by Ge Wang (Wang et al., 1993). Many authors have also succeeded in creating helical cone-beam algorithms based on the Feldkamp method (Kachelrieß et al., 2000; Kudo and Saito, 1991; Noo et al., 1999; Smith and Chen, 1992; Tang et al., 2006a; Tang and Hsieh, 2004; Tang et al., 2006b; Wang et al., 1992; Yan and Leahy, 1992). As noted by Wang, "*The key idea is to correct cone-beam data*

into fan-beam counterparts in a heuristic way. As a primary example, a cone-beam datum along an oblique ray can be approximately converted to the fan-beam counterpart along a transverse ray by multiplying the former with the cosine of the angle between the oblique and transverse rays" (Wang et al., 2007).

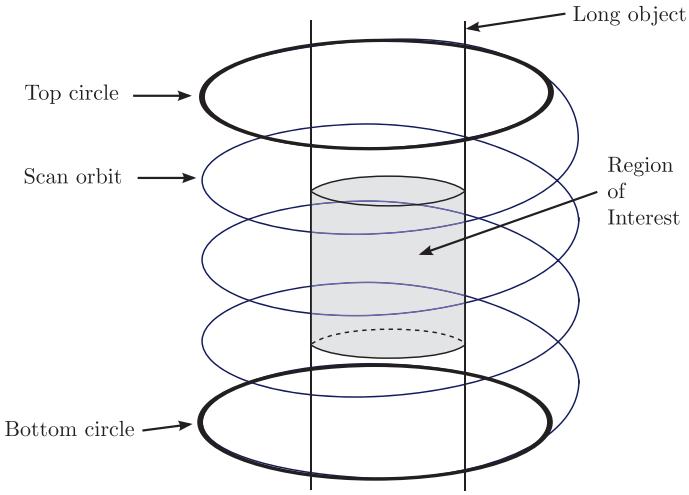

Figure 5.2: Helix-and-two-circles scan path for ROI imaging as proposed by Tam et al..

Methods of solving for exact cone beam image reconstruction have been independently reported by Tuy, Smith, and Grangeat as early as 1983 (Grangeat, 1991; Smith, 1985; Tuy, 1983). The requirement in all of these algorithms is that all the x-rays from the source that pass through the object must be covered by the detector. For example in Tuy's condition, every plane that intersects with the object must also intersect with the x-ray source orbit at least once. However, objects in medicine and many industrial inspections are very long, which would require a very large detector to cover the entire length of the object. In addition, in most of these objects, only a smaller section is of interest. The problem of reconstructing for a smaller ROI without scanning the entire object is extremely challenging. Intuitively, we need to collect all of the x-ray paths that penetrate the ROI for reconstruction. However, because parts of these x-ray beams are "corrupted" by other parts of the objects, they no longer represent the ROI exclusively. We can attempt to reconstruct the "corrupted" parts of the x-ray paths, but the data are often missing because the

detector was not large enough to collect all of the information. This problem is known as data truncation, or missing data. The exact solution to an long object problem with a ROI was proposed by Tam in 1998 using a spiral-and-two-circle scan path for ROI imaging (Tam et al., 1998), as shown in Fig. 5.2. Unfortunately, it is not entirely trivial to merge the truncated data from multiple helical turns. This problem was not solved until early 2002 by Katsevich's algorithm (Katsevich, 2002, 2003, 2004).

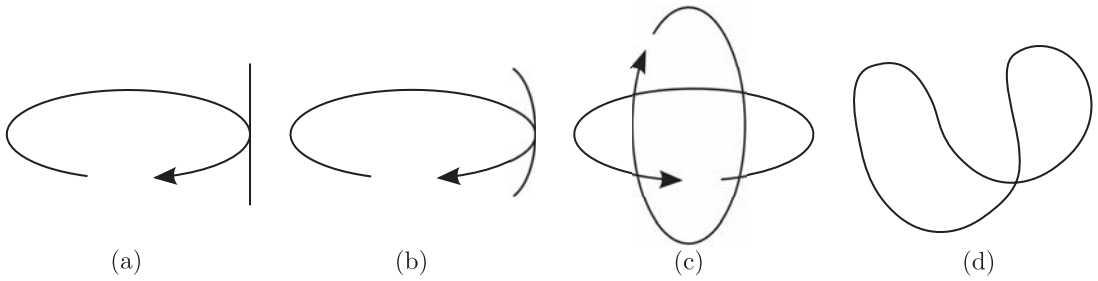

Figure 5.3: Different scanning trajectories for complete sampling. (a) circle-plus-line; (b) circle-plus-arc; (c) dual circles; and (d) saddle.

Since Katsevich's invention, various sophisticated formulas have been proposed and developed for exact reconstruction using longitudinally and transversely truncated projection data and for various scanning geometries shown in Fig. 5.3. However, although these algorithms are highly sophisticated and novel, they are computationally expensive compared to the popular FBP algorithms, not to mention the difficulties in building the hardware for these orbits. Currently, most CT manufacturers still use the approximate cone-beam reconstruction algorithms instead of exact cone-beam reconstruction algorithms for two reasons. First, the data requirements for exact reconstruction are still too difficult due to physical constraints. Second, the approximate algorithms already provide very good and sometimes even better performance compared to the exact reconstruction method, which may not have the best noise characteristics (Wang et al., 2008). It will be interesting to see when exact algorithms will replace approximate algorithms in the future.

5.2 Iterative Reconstruction Techniques

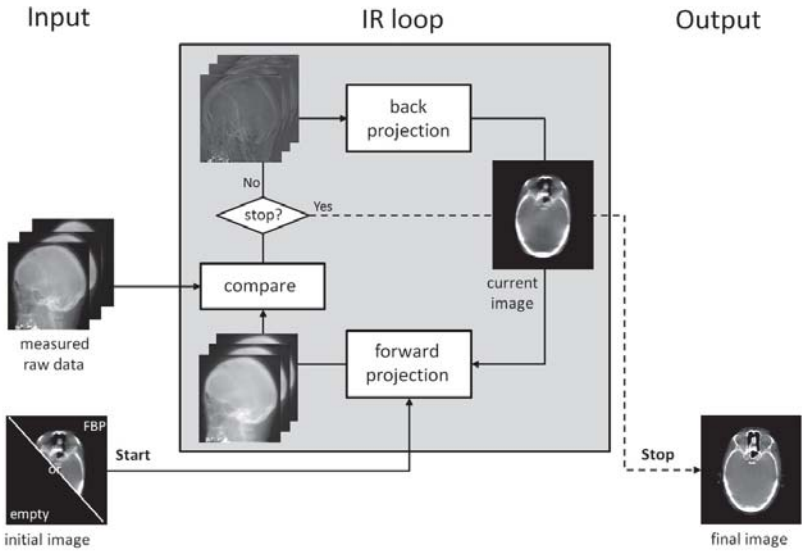

Figure 5.4: The general process of iterative algorithm[1]. The compare step involves calculating a correction term by comparing the predicted and measured data, which is then backprojected onto the object space to generate a new estimate of the object.

Iterative techniques attempt to reconstruct the object using projection images in an iterative fashion, where the estimate of the object at the current iteration will be used for the next iteration. All iterative reconstruction methods consist of three major steps. First, the forward model of the system calculates an estimate of the raw data utilizing either prior knowledge of the object or using a blank object in the first iteration. Second, the estimated raw data and the real measured data are compared, and a correction term is calculated. Third, the correction term is back-projected onto the object space and multiplied by the current object to to create a new estimate. Shown in Fig. 5.4, this process is repeated until either a fixed number of iterations is reached or the object estimation reaches a predefined criterion.

[1]Reprinted from: *Physica Medica*, **28**, Bester, M., Kolditz, D., and Kalender, W. A., Iterative reconstruction methods in X-ray CT, pp. 94-108, Copyright(2012), with permission from Elsevier.

5.2.1 Algebraic Reconstruction Techniques

From a historical perspective, the first reconstructed CT image was created using the iterative algebraic reconstruction technique (ART) based on Kaczmarc's algorithm, where the method attempts to find the object by solving a series of linear equations iteratively in

$$\mathbf{A}\,\mathbf{x} = \mathbf{b}. \tag{5.2}$$

In terms of image reconstruction, $\mathbf{x}$ is $N \times 1$ with elements represent the object voxel values that need to be reconstructed, $\mathbf{A}$ is a $M \times N$ system matrix that models the production of the image data, and $\mathbf{b}$ is $M \times 1$ where the elements represent the pixels values of the measured raw data. Both $\mathbf{x}$ and $\mathbf{b}$ are often constrained to be positive in the algorithm based on the assumption that negative attenuation values and negative detector values are not possible. The entries of the matrix $\mathbf{A}$ correspond to x-rays from the source through the object volume to the detector pixels. Solving for the object voxel values involves solving Eqn. 5.2, where $\mathbf{A}$ is most likely not a square matrix and is fairly large in size. The iterative rule to solve for the object voxel value can have the general form

$$\hat{\mathbf{x}}^{k+1} = \hat{\mathbf{x}}^{k} + \mathbf{B}[\mathbf{b} - \mathbf{A}\hat{\mathbf{x}}^{k}], \tag{5.3}$$

where $\mathbf{B}$ is an $N \times M$ matrix. This type of iterative algorithm is found by minimizing the quadratic difference between the experimental data the data generated by $\mathbf{A}$ (Barrett and Myers, 2004). Algorithms such as simultaneous ART (SART), ordered-subset (OS) version of SART, and other variations of SART or OS-SART all follows this general form (Wang and Jiang, 2004; Yu et al., 2011)

Starting from ART, a series of algorithms evolved that would try to converge to the solution faster, to reduce noise, and to reduce problems with streak artifacts; however, in general, all ART-based methods are non-statistical and model the geometry of the acquisition process better than common analytical methods based on FBP. Therefore, ART-based methods can better deal with sparse data and an irregular sampling of acquisition positions (Beister et al., 2012).

5.2.2 Statistical Iterative Reconstruction Techniques

Statistical iterative reconstruction techniques have been used extensively in single photon emission tomography (SPECT) and positron emission tomography (PET), where low photon rates and noise are the major issues. Due to public awareness of CT radiation and a need to reduce the risks associated with x-ray radiation, there has been a push to transition from FBP to statistical iterative reconstruction techniques, which has the potential of lowering radiation doses while suppressing image noise with low-dose scan techniques. Therefore, it is crucial that the mathematical models used for the CT system are accurate, and the modeling errors are suppressed so they do not grow during the iterative process. There are two types of models that are typically used in iterative reconstruction algorithms: a physical model that involves the geometry of the system and a statistical model that attempts to formulate the noise within the imaging system.

Unlike the analytical reconstruction techniques, where many physical assumptions must be made to allow for the mathematics to be more manageable, physical models used by the iterative algorithm can account for any physical process and are only limited by the computational power of the processing computer. For example, analytical solutions usually assume that the x-ray focal spot is infinitely small; the shapes and dimensions of the detector cells are ignored so that all x-ray photon interactions are assumed to take place at the center of the detector cells. Iterative reconstruction algorithms require no prior assumption about the geometry of the system. For example, a commonly used model is to launch multiple pencil rays from various locations on the x-ray focal spot that has a finite size. These pencil rays passes through an image voxel at different positions and land at different detector pixels to mimic different x-ray photon paths through an object. The summation of the x-rays at each detector cell is then used to approximate the CT image system, shown in Fig. 5.5a. Needless to say, this method is extremely time-consuming and computationally intensive. Another commonly used approach is to model the "shadow" cast by each image voxel onto the detector cells and rely

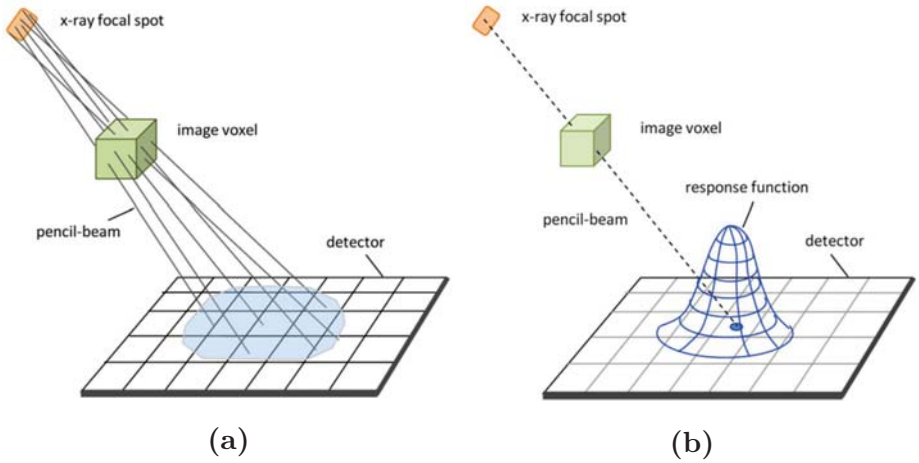

Figure 5.5: Common physical models used for the iterative reconstruction algorithm[2]. (a) The pencil beam model; and (b) the point-response model.

on the point-response function to model the forward projection process of the CT system. This point-response function is non-stationary and changes with the voxel location to account for different magnifications and orientations, shown in Fig. 5.5b. Comparatively, this method is computationally more efficient (Hsieh et al., 2013).

The statistical model or the noise model used in the iterative reconstruction algorithm attempts to incorporate the statistics of the detected photons into the reconstruction process. The random processes may include incident photon flux variations, also known as the Poisson distribution. Though Poisson distribution is still approximate due to the poly-energetic nature of the x-ray photons created by the source in CT. In addition, the variation in the number of photons produced in the scintillator by polychromatic x-ray photons, shot noise in the photodiodes, and noise in the readout electronics all contribute to the noise in the images used in the reconstruction algorithm. The most common noise model used is the zero-mean Gaussian noise.

[2]Hsieh, J., B. Nett, Z. Yu, K. Sauer, J. B. Thibaut, and C. A. Bouman (2013). Recent Advances in CT Image Reconstruction. *Curr. Radiol. Rep.*, **1**, pp. 39-51, with kind permission from Springer Science and Business Media.

Once both the geometry and noise of the CT system are properly modeled, a cost function is chosen. The iterative process searches for the minimum of the cost function, and the solution that minimizes this cost function is the reconstructed object. This cost function, sometimes called an objective functional, typically consists of two components: a data agreement term that evaluates the difference between the experimental data and the data generated by the model, and a regularizing term, sometimes called a penalty function that depends only on the object and serves as a prior, such as positivity. If the functional is strictly convex, then the minimum is unique, and all algorithms should obtain the same image if they were to run to convergence. In practice, however, iterative algorithms may not be run to convergence, and the resulting image depends on the algorithm, the initial estimate, and the stopping rule.

5.3 Maximum-Likelihood Expectation-Maximization (MLEM) algorithm

In this project, we used the Maximum-Likelihood Expectation-Maximization algorithm for the reconstruction process without any regularization functions. The MLEM algorithm is shown in Eq. 5.4 (Wernick and Aarsvold, 2004), where g_i are the image pixel values over all projection angles and represent the attenuation values of x-rays through the object voxels onto each detector pixels, H_{ij} is the imaging matrix that models the x-ray imaging system and maps each object voxel value to all image pixel value for all projection angles, and f_j are the object voxel values, and represent the x-ray attenuation coefficient of the object integrated over the object voxel. The index j and k are used to represent the object voxels, and i is indexed over image pixels on the detector for all projection angles.

$$\hat{f}_j^{(n+1)} = \frac{\hat{f}_j^{(n)}}{\sum\limits_{i'} H_{i'j}} \sum_i H_{ij} \frac{g_i}{\sum\limits_k H_{ik}\hat{f}_k^{(n)}} \tag{5.4}$$

$\sum\limits_k H_{ik}\hat{f}_k^{(n)}$ takes the current object voxel values, $\hat{f}_k^{(n)}$, and calculates its forward projection image over all angles. The forward projection images are then divided

into the data image vector, g_i, over all angle. The result, $\frac{g_i}{\sum_k H_{ik}\hat{f}_k^{(n)}}$, is a ratio between the set of simulated projection images and the experimental data. This ratio is then back-projected into object space, and is used to correct the estimate of the current object. The next iteration for object voxels, $\hat{f}_j^{n+1}$, is calculated by multiplying correction term by the current object voxel values, $\hat{f}_j^{(n)}$, and scaled by the sensitivity S_j. The sensitivity , $S_j = \sum_{i'} H_{i'j}$, is calculated by summing the H matrix over all detector pixels and projection angles, which represents the back projection of the detector values from all projection angles onto the object voxel values.

The most important factor in the MLEM algorithm is the imaging matrix, H, that models the imaging system. The H matrix can be measured in PET or SPECT, where a point source is scanned throughout the entire volume of the object, and signals are recorded for every object point at every detector pixel for all detectors. To measure the H matrix for CT using this method is nearly impossible because the H matrix would have to be astronomically large due to the number of detector pixels and projection angles. Instead of using a stored H matrix, we opted to model the CT system and compute the H matrix as operators by calculating the forward projection and backward projection processes on-the-fly using a Graphics Processing Unit (GPU). The forward projection process is the equivalent of calculating $\sum_k H_{ik}\hat{f}_k^{(n)}$ in Eq. 5.4, and the same backward projection process is used to calculate both the sensitivity, $\sum_{i'} H_{i'j}$, and in computing the correction term to the object, $\sum_i H_{ij}\frac{g_i}{\sum_k H_{ik}\hat{f}_i^{(n)}}$.

5.4 CT model and projector calculation

In x-ray imaging, the mean output of the m^{th} detector element is a function of many factors such as the size of the source, its temporal and spectral distribution, the spectral and temporal response of the detector element and the x-ray attenuation of the object that is also a function of incident x-ray energy. All of these factors

must be integrated over their respective space along x-rays from the source to the detector element in order to fully describe the mean value at the m^{th} detector element. Even if we make assumptions that the spectral response of the detector is the same for all elements and is independent of direction and position of the radiation, the attenuation coefficient of the object is independent of energy, we are still left with a nonlinear equation that relates the attenuation coefficient of the object to the value at the m^{th} detector element, as

$$\bar{g}_m \propto \int_P d^2r \int_{2\pi} d\Omega \; d_m(\mathfrak{r}, \hat{\mathbf{s}}) \; L_p(\mathfrak{r} - \hat{\mathbf{s}}\ell_0, \hat{\mathbf{s}}) \exp\left[- \int_0^{\ell_0} d\ell' \mu_{tot}(\mathfrak{r} - \hat{\mathbf{s}}\ell') \right], \tag{5.5}$$

where, $d_m(\mathfrak{r}, \hat{s})$ is the detector response function, $L_p(\mathfrak{r}, \hat{\mathbf{s}})$ is the photon radiance of the source, $\mu_{tot}(\mathbf{r}, \hat{\mathbf{s}})$ is the object's x-ray attenuation coefficient, and the equation is integrated over P, the detector plane, and the solid angle, 2π ster collected by the detector element (Barrett and Myers, 2004). This equation is nonlinear with respect to the attenuation coefficient, which is what we want to estimate in reconstruction. However, we can still take the logarithm of Eq. 5.5 and calculate its approximation by expanding the exponential term in a Taylor series. The result is

$$\ln \bar{g}_m \propto - \int_P d^2r \int_{2\pi} d\Omega \; d_m(\mathfrak{r}, \hat{\mathbf{s}}) L_p(\mathfrak{r} - \hat{\mathbf{s}}\ell_0) \; \left[\int_0^{\ell_0} d\ell' \mu_{tot}(\mathfrak{r} - \hat{\mathbf{s}}\ell') \right], \tag{5.6}$$

which is now a linear function that relates the mean detector value to the attenuation coefficient of the object. This equation describes a blurred ray from the source to the m^{th} detector element. If we make further assumptions that all x-rays originate from a point source and that the detector response function is a delta function so

$$d_m(\mathfrak{r}, \hat{\mathbf{s}}) \, L_p(\mathfrak{r} - \hat{\mathbf{s}}\ell_0) \propto \delta(\mathbf{r} - \mathbf{r_m}) \delta(\hat{\mathbf{s}} - \hat{\mathbf{s_m}}), \tag{5.7}$$

Then Eq. 5.5, becomes

$$\ln \bar{g}_m \propto \left[- \int_0^{\ell_0} d\ell' \, \mu_{tot}(\mathfrak{r}_\mathfrak{m} - \hat{\mathbf{s}}_m \ell') \right]. \tag{5.8}$$

The log of a detector element is linearly proportional to a line integral over the attenuation coefficient of the object. If we approximate the object as a set of cubic

voxels, where the value of each voxel is equal to the average attenuation coefficient of the object over that voxel. Then this line integral is a summation of the attenuation values of the voxels multiplied by the length of the ray that passed through the voxels. For complete derivation of Eq. 5.5, refer to sections 16.1.4 and 16.1.7 in (Barrett and Myers, 2004).

A pencil-beam model was used for both the forward and backward projection process, where we assumed that each x-ray beam is launched from an infinitely small x-ray point source. This pencil beam travels towards the geometrical center of each detector pixel. Along the way, the contributions from every voxel for each ray is calculated using Siddon's algorithm (Siddon, 1985). This model does not account for any scatter in the object, and it assumes that the x-ray beam is monochromatic.

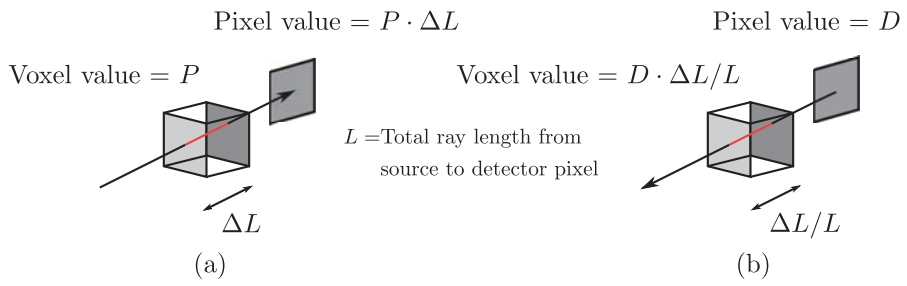

Figure 5.6: The (a) forward and (b) backward projection process.

In the forward projection process, the final values at the each of the detector elements represent the summation of the product between the length of the ray that passed through each voxel and the value at each voxel, shown in Fig. 5.6a. This final value at each of the detector element is $ln\bar{g}_m$ in Eq. 5.8. In the backward projector, the order is reversed. We take the value at the detector element, trace a ray backward through the object volume to the x-ray source. For every voxel penetrated by that ray, we calculate the length of the ray that passed through the voxel. This length is expressed as a fraction of the total ray length through the object volume, and is multiplied by the value at the detector element, shown in Fig. 5.6b. This process was repeated for all x-rays traced to all detector pixels.

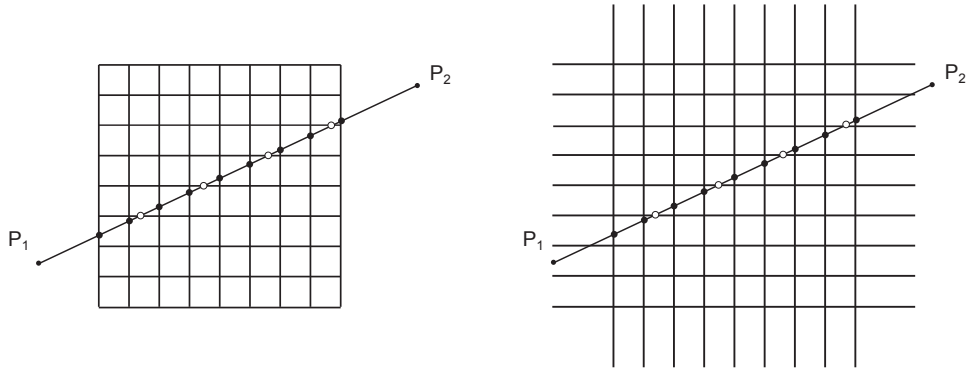

Figure 5.7: Considering a 2-dimensional object (a) as the intersection areas of orthogonal sets of equally spaced, parallel lines (b).

In the next section we will explain briefly the Siddon's algorithm and how we modified the algorithm so it can be implemented on the GPU.

5.4.1 Siddon's algorithm

Siddon's algorithm is a method of calculating the exact radiological path for a three-dimensional voxel array. Instead of directly calculating the intersections of the ray with each pixel, it calculates the ray's intersection with three parallel planes in the object volume $\{x, y, z\}$. For simplicity, a 2-dimensional object is shown in Fig. 5.7. Since the lines are equally spaced, it is only necessary to determine the first intersection. The other intersections can then be automatically generated by recursion.

For a 3-dimensional CT volume array of $(N_x - 1, N_y - 1, N_z - 1)$ voxels, the orthogonal sets of equally spaced, parallel planes can be written as,

$$\begin{aligned} X_{plane}(i) &= X_{plane}(1) + (i-1)\, d_x \quad (i = 1, ..., N_x), \\ Y_{plane}(j) &= Y_{plane}(1) + (j-1)\, d_y \quad (j = 1, ..., N_y), \\ Z_{plane}(j) &= Z_{plane}(1) + (k-1)\, d_z \quad (k = 1, ..., N_z), \end{aligned} \tag{5.9}$$

where d_x, d_y, and d_z are the distances between the x, y, and z planes, respectively. They are also the lengths to the sides of the volume voxel. We can calculate a ray's

intersection with the initial and final planes of the volume array, initiating at the point, $P_1 = (X_1, Y_1, Z_1)$, and terminating at the point, $P_2 = (X_2, Y_2, Z_2)$, by first calculating a set of minimum and maximum parametric values for that ray using the following equation,

$$\begin{aligned} \alpha_x(1) &= \frac{X_{plane}(1) - X_1}{X_2 - X_1}, & \alpha_x(N_x) &= \frac{X_{plane}(N_x) - X_1}{X_2 - X_1}, \\ \alpha_y(1) &= \frac{Y_{plane}(1) - Y_1}{Y_2 - Y_1}, & \alpha_y(N_y) &= \frac{Y_{plane}(N_y) - Y_1}{Y_2 - Y_1}, \\ \alpha_z(1) &= \frac{Z_{plane}(1) - Z_1}{Z_2 - Z_1}, & \alpha_z(N_z) &= \frac{Z_{plane}(N_z) - Z_1}{Z_2 - Z_1}. \end{aligned} \tag{5.10}$$

If the denominator, $(X_2 - X_1)$, $(Y_2 - Y_1)$, or $(Z_2 - Z_1)$, is equal to zero, then the ray is parallel to that particular plane, and the corresponding α_x, α_y, or α_z will be undefined and excluded from the calculation. These equations calculate the surface planes of the CT volume against the initial and final points of the ray.

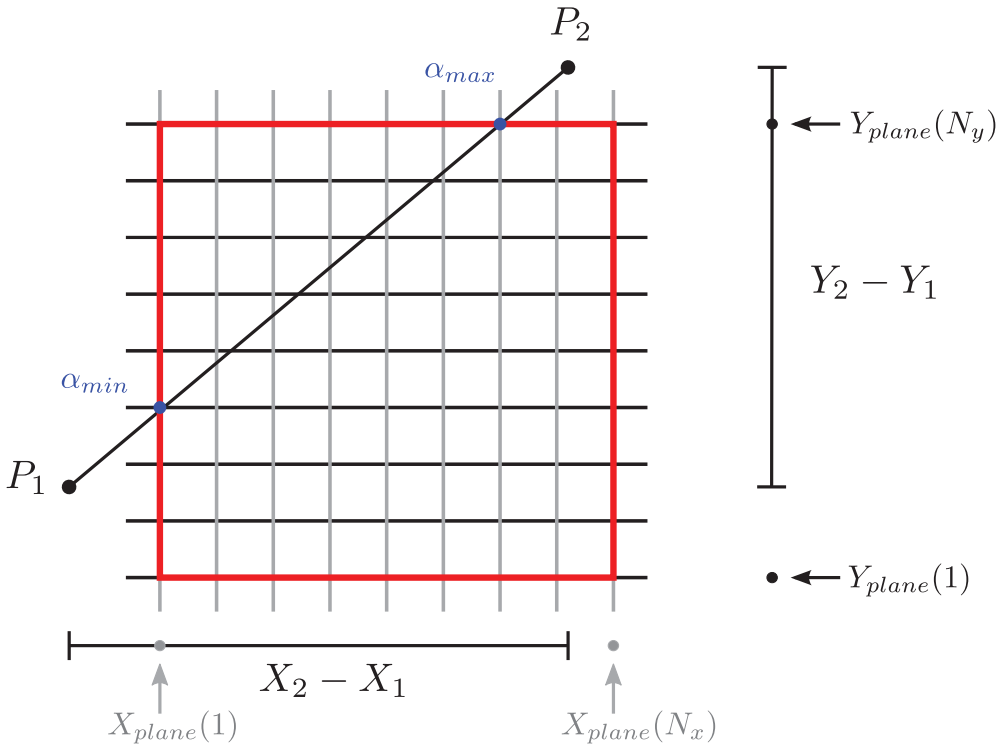

Figure 5.8: Siddon's algorithm showing the minimum and maximum parametric values for a ray passing through a 2D object array.

Once the values from Eq. 5.10 are found, two parametric values that are used to indicate the initial and final intersections of the ray with the object volume are determined using,

$$\begin{aligned}
\alpha_{min} = max\{0,\, &min\left[\alpha_x(1),\, \alpha_x(N_x)\right], \\
&min\left[\alpha_y(1), \alpha_y(N_y)\right], min\left[\alpha_z(1), \alpha_z(N_z)\right]\}, \\
\alpha_{max} = min\{1,\, &max\left[\alpha_x(1),\, \alpha_x(N_x)\right], \\
&max\left[\alpha_y(1), \alpha_y(N_y)\right], max\left[\alpha_z(1), \alpha_z(N_z)\right]\}.
\end{aligned} \tag{5.11}$$

If α_{max} is less than or equal to α_{min}, then the ray does not intersect the object volume and that ray will be excluded from the calculation. α_{min} and α_{max} are scaled against the total distance between P_1 and P_2, and are valued between 0 and 1. These variables are shown in 2-dimensions in Fig. 5.8.

Once we have determined the intersections of the ray with the surface planes of the object volume, we can then calculate the plane indices that will be intersected by the ray inside the object volume using the following equations,

$$\begin{aligned}
&\text{if } (X_2 - X_1) \geq 0 \\
&\qquad i_{min} = N_x - \left[X_{plane}(N_x) - \alpha_{min}(X_2 - X_1) - X_1\right]/d_x, \\
&\qquad i_{max} = 1 + \left[X_1 + \alpha_{max}(X_2 - X_1) - X_{plane}(1)\right]/d_x. \\
&\text{if } (X_2 - X_1) \leq 0 \\
&\qquad i_{min} = N_x - \left[X_{plane}(N_x) - \alpha_{max}(X_2 - X_1) - X_1\right]/d_x, \\
&\qquad i_{max} = 1 + \left[X_1 + \alpha_{min}(X_2 - X_1) - X_{plane}(1)\right]/d_x,
\end{aligned} \tag{5.12}$$

and with similar expressions for j_{min}, j_{max}, k_{min}, and k_{max}. Note that values when $(X_2 - X_1) = 0$, $(Y_2 - Y_1) = 0$, and $(Z_2 - Z_1) = 0$ had been excluded from these calculations. The indices are rounded towards nearest integers, though care must be taken when calculating the indices near the object surface planes. In execution, both the upper and lower bound integers were calculated, and the actual indices were selected based on the values of α_{min} and α_{max}. This was done to avoid errors that may occur in execution because the calculations were done using floating-point

precision. The corresponding parametric values to each index are computed using,

$$\begin{aligned} \alpha_x(i) &= [X_{plane}(i) - X_1]/(X_2 - X_1) \\ &= \alpha_x(i-1) + d_x/(X_2 - X_1) \end{aligned} \tag{5.13}$$

with similar expressions for α_y, and α_z.

Once the parametric values $\{\alpha_x\}$, $\{\alpha_y\}$, and $\{\alpha_z\}$ for the ray are calculated, we can then determine the length of the ray that passed through a voxel by first merging the parametric values into one large set as, $\{\alpha\} = \{\{\alpha_x\}, \{\alpha_y\}, \{\alpha_z\}\}$, and sorting $\{a\}$ in ascending order from the lowest to the highest value. The path length through a voxel can then be calculated using,

$$l(m) = d_{12}\left[\alpha(m) - \alpha(m-1)\right] \qquad (m = 1, ..., n), \tag{5.14}$$

where the quantity d_{12} is the distance between P_1 and P_2, and is determined by,

$$d_{12} = \left[(X_2 - X_1)^2 + (Y_2 - Y_1)^2 + (Z_2 - Z_1)^2\right]^{1/2}, \tag{5.15}$$

and n is the number of elements in the set $\{a\}$,

$$n = (i_{max} - i_{min} + 1) + (j_{max} - j_{min} + 1) + (k_{max} - k_{min} + 1) + 1. \tag{5.16}$$

This calculation is graphically represented in Fig. 5.9 in two-dimensions.

To locate the particular voxel index, $i(m), j(m), k(m)$, bounded by α_{m-1} and α_m, we can use the following equation,

$$\begin{aligned} i(m) &= 1 + \left[X_1 + \alpha_{mid}(X_2 - X_1) - X_{plane}(1)\right]/d_x, \\ j(m) &= 1 + \left[Y_1 + \alpha_{mid}(Y_2 - Y_1) - Y_{plane}(1)\right]/d_y, \\ k(m) &= 1 + \left[Z_1 + \alpha_{mid}(Z_2 - Z_1) - Z_{plane}(1)\right]/d_z, \end{aligned} \tag{5.17}$$

where α_{mid} is,

$$\alpha_{mid} = \left[\alpha(m) + \alpha(m-1)\right]/2. \tag{5.18}$$

Finally, the total radiological path, d, for one ray may be calculated using,

$$\begin{aligned} d &= \sum_{m=1}^{m=n} l(m)\rho\left[i(m), j(m), k(m)\right] \\ &= d_{12} \sum_{m=1}^{m=n} \left[\alpha(m) - \alpha(m-1)\right]\rho\left[i(m), j(m), k(m)\right], \end{aligned} \tag{5.19}$$

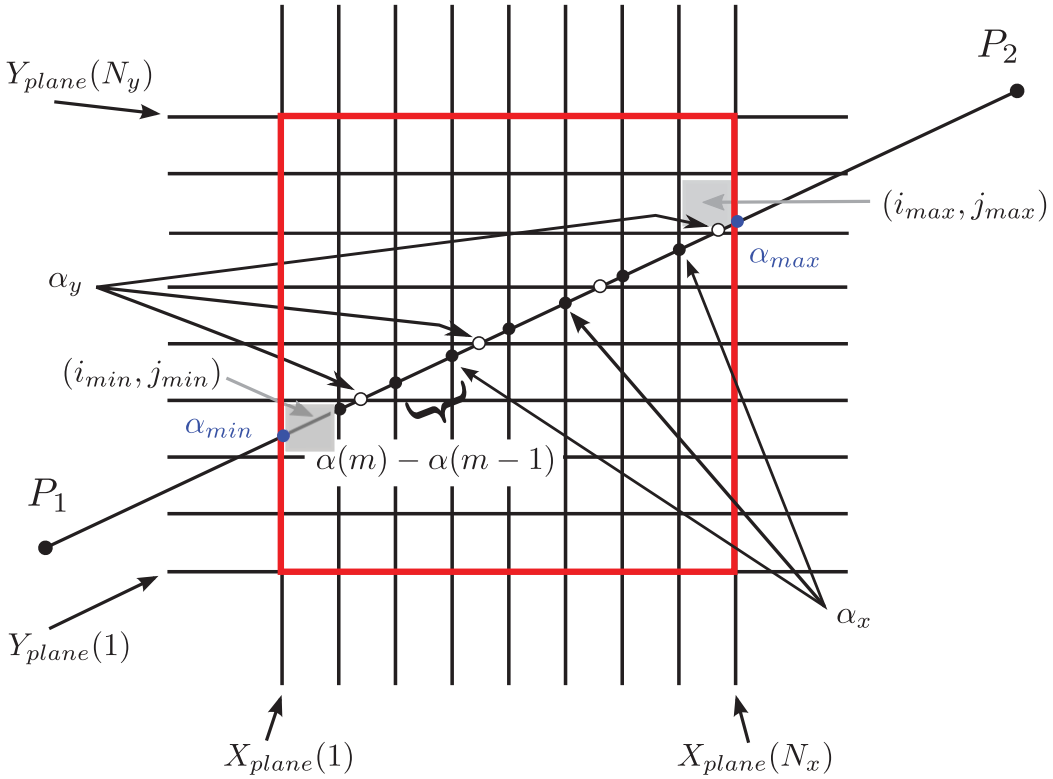

Figure 5.9: A detailed view of the variables for the Siddon's algorithm in 2-dimensions.

where $\rho\,[i(m), j(m), k(m)]$ is the voxel value of the object volume at voxel index $i(m), j(m), k(m)$.

Normally, d is calculated using a loop until a desired number of rays are reached. However, each ray corresponds to one detector element and is independent of each ray. We can utilize the GPU's parallel computing capability to trace all rays simultaneously by assigning one CUDA thread per ray.

The ray-trace process can be accomplished by following the Siddon's algorithm up until Eq. 5.12. Since each ray is traced simultaneously, we cannot calculate and presort the entire set, $\{\alpha\}$, for each ray on the GPU. Instead we opted to calculate and sort $\{\alpha\}$ on-the-fly, where parametric values α_x, α_y, and α_z are calculated simultaneously and independently on the GPU device memory for each ray starting with $\alpha_x(1)$, $\alpha_y(1)$, $\alpha_z(1)$. A loop is used to trace the rays from beginning to end.

Each time the loop executes, the minimum of the three values is found, we then increment the alpha index by 1 only for the parametric value of the corresponding plane. This minimum value is set to $\alpha(m)$ and is used to calculate for d along with the value from the previous loop, $\alpha(m-1)$. The loops are carried out until all values in the set, $\{\alpha\}$, were computed because we know both α_{min} and α_{max} from previous calculations and all the indices of the object planes for all rays. In addition, because the number of elements, n, in the set, $\{\alpha\}$, can be calculated using Eq. 5.16, we can also set the loop to run for a fixed number of iterations equal to the ray with the maximum n while setting a proper terminating condition for all other rays in the loop so the extra loops does not effect rays that have already completed the trace process. As a result, α is not computed all at once, but rather computed and sorted on-the-fly where only the most current of the two values, $\alpha(m)$ and $\alpha(m-1)$ are stored in device memory. Figure 5.10 shows a diagram of the Siddon's algorithm implementation in CUDA.

5.4.2 Forward and backward projector calculation

The forward projector was implemented following Siddon's algorithm and Fig. 5.10, where each x-ray originates from the x-ray point source and travels to the pixel center of each detector element. The object voxel contribution to the ray was calculated using Eq. 5.19. The treatment for the backward projector is very similar to the forward projector, with exception to an added CUDA function, `atomicAdd()`. In the forward projection, each voxel index is calculated from the ray intersections with the planes of the object volume, and the contribution of voxel values to each ray is independent of other rays (i.e. the voxel values were read by the CUDA threads via read-only access, and tracing rays only involved reading the object voxel values). However, in the backward projection the CUDA threads require that the object voxels need to have both read and write access, but since different ray needs access to the same voxel and the voxel value changes depending on the access sequence of the threads. This requires an additional step of using `atomicAdd()` function that

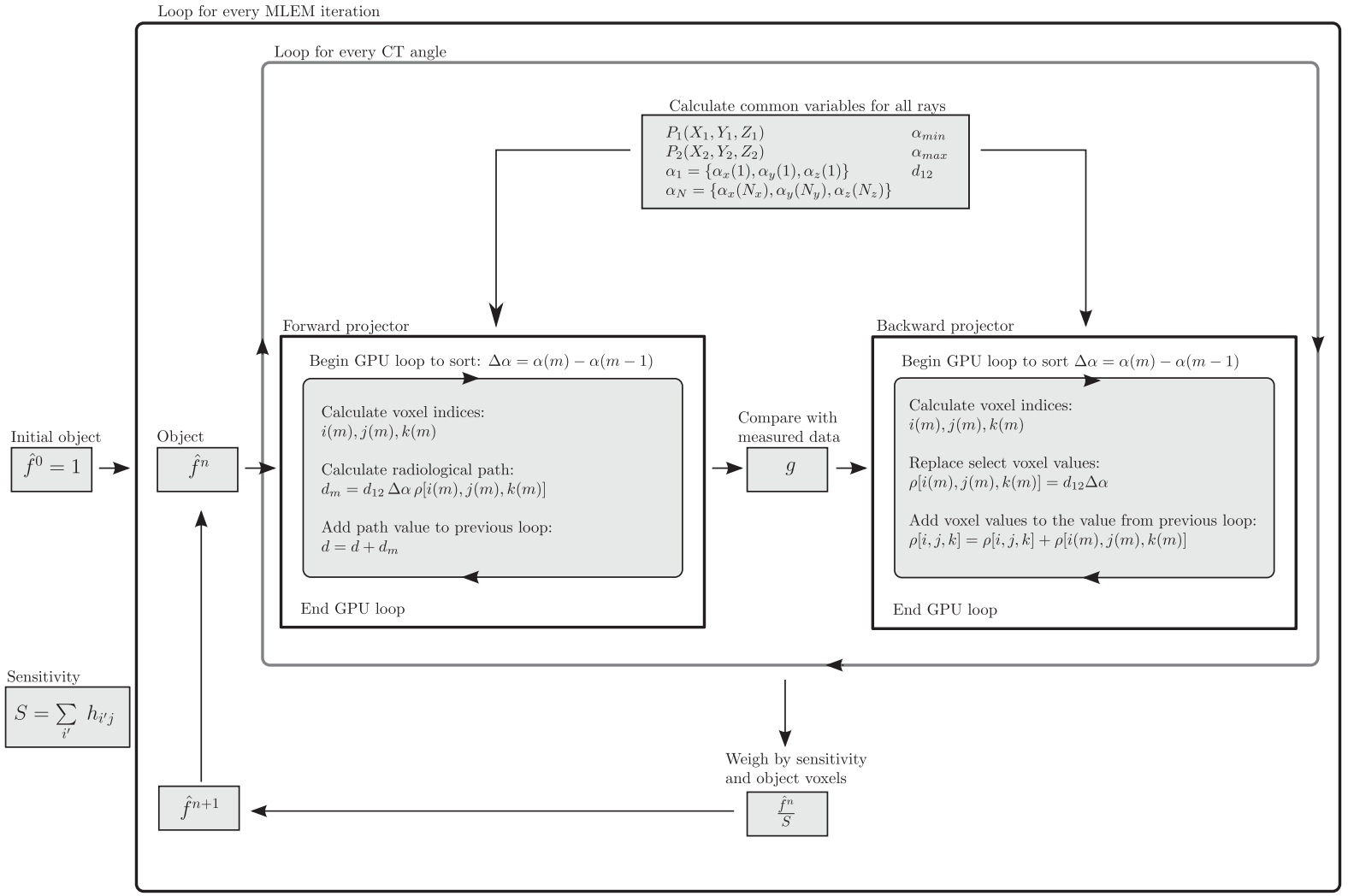

Figure 5.10: The algorithm for Siddon's implementation on CUDA.

guarantees access to the voxel value is sequential and without interference from other threads. In other words, no other thread can access this address until the operation is complete. For further information about this function refer to the CUDA toolkit documentation (NVIDIA, 2014). Note because of this additional function, most of the bottleneck to the MLEM algorithm occurs here. Another bottleneck occurs when $\{\alpha\}$ is being sorted.

5.4.3 Sensitivity calculation

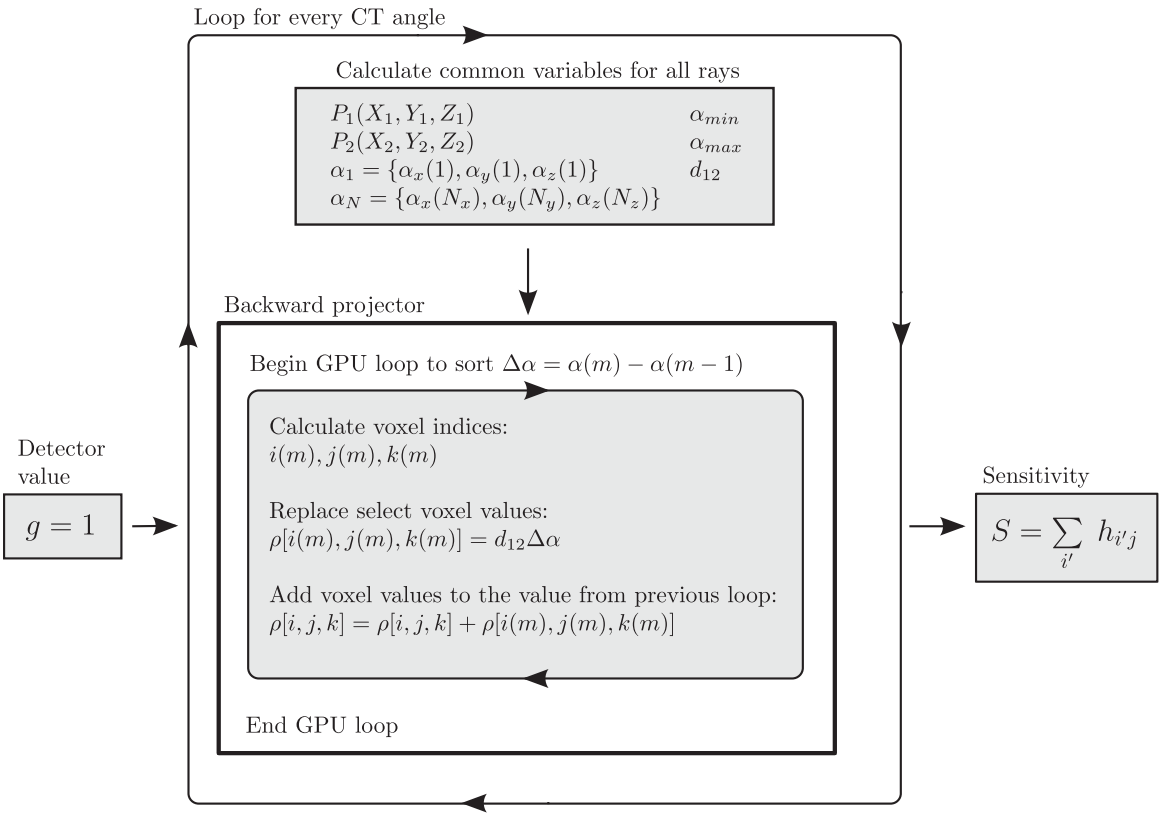

Figure 5.11: Algorithm for sensitivity calculation.

The sensitivity voxels, $\sum_{i'} H_{i'j}$ in Eq. 5.4, represents the contribution of all detector values at all projection angles on the object volume. The procedure to compute the sensitivity volume is to first set all detector values to one, then back filling the object voxel values using the back projector for all scanned angles, $S = H^t 1$. The

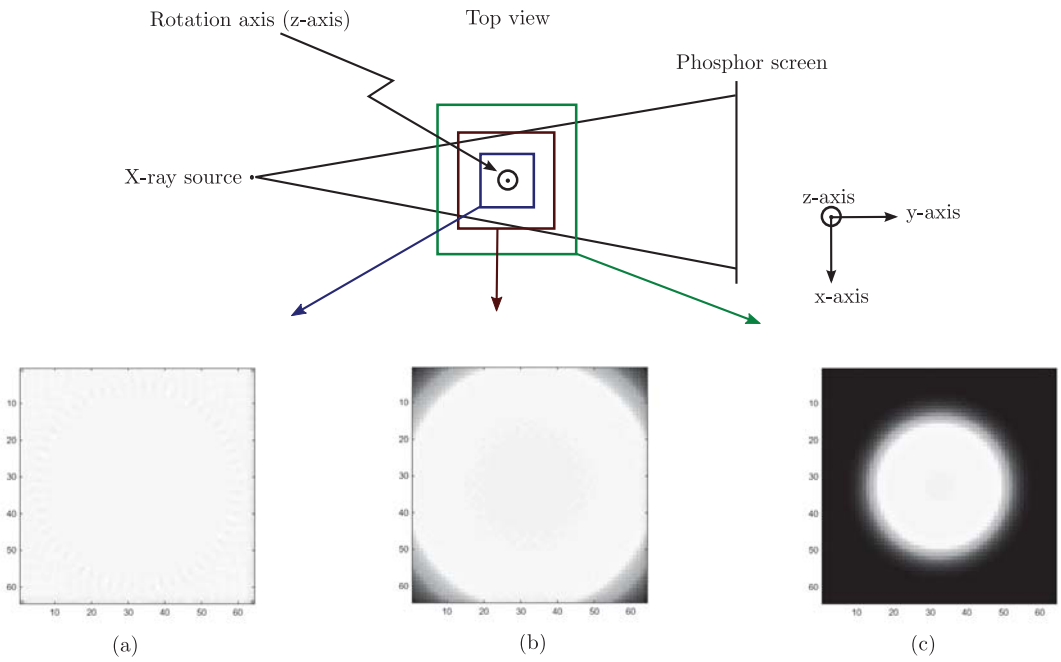

Figure 5.12: A Central slice of the sensitivity volume calculated using a fixed CT geometry and scan angles for three different object volume setup.

values in the sensitivity volume depends on the geometry of the CT system, number and size of the object volume, number of detector pixels, and scan routine. As a result, it is always computed in the beginning of every reconstruction event. However if one were to use a different data set while keeping geometry, object volume, and detector pixels constant, then sensitivity volume does not need to be recalculated and can speed up the reconstruction process.

The actual sensitivity of the CT system depends only on the CT geometry. The sensitivity volume that is calculated in the reconstruction algorithm requires both the CT geometry, scan routine and object voxel parameters that are defined in the parameter sheet. When setting up the parameter sheet for reconstruction, the voxel volume parameters specify the region of space that will be reconstructed. Ideally, we want the targeted regions of the object to lie within the sensitive regions of the CT system so all rays traced from the x-ray source to the detector pixels will pass through the targeted region at every single projection angle. Sometimes it

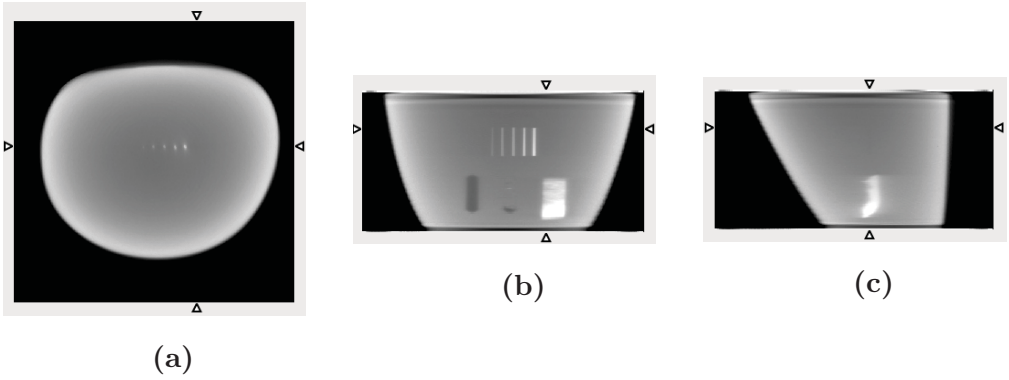

Figure 5.13: A slice of the reconstructed phantom in the (a) x-y plane (b) x-z plane, and (c) y-z plane, calculated using 512 × 512 × 128 voxels after 10 iterations, where each voxel size is 0.25 mm × 0.25 mm × 0.5 mm in the x, y, and z direction.

is advantageous to perform a test run by calculating only the sensitivity volume before calculating multiple reconstruction iterations to ensure that the size of the object volume is within the sensitive region. Figure 5.12 shows a central slice of the sensitivity volume for three different object volume setups with a fixed CT geometry and scan routine. Figure 5.12a shows that the object volume is smaller and is within the sensitive region of the CT system. Figure 5.12c shows that much of the object volume lies outside the region, so much of the GPU memory and processing power is wasted in this setup. Figure 5.12c shows that majority of the object lies within the region. This is the optimum setup for reconstruction because we are not wasting GPU memory and processing power by computing voxels that do not lie inside the CT field of view defined by the detector and CT geometry. We are also not restricting ourselves to a smaller field of view than necessary, as in Fig. 5.12a.

5.4.4 Reconstruction results

We took CT projection images of the breast phantom that was used in the DR system. Figure 5.13 shows a few slices of the reconstructed object after 10 iterations using 512 × 512 × 64 voxels. Each voxel is 0.25 mm × 0.25 mm in the x-y plane,

and 1 mm in the z-axis.

We have noticed that, d_x and θ_y are the two parameters in the CT system that are most critical for obtaining accurate reconstruction images. To demonstration this, we have calculated projection images of a thin rectangular box in simulation using the same CT geometry as the breast phantom used in Fig. 5.13. The box is 32 mm long and the cross section of the box is 0.75 mm $\times$ 1.75 mm oriented so its long axis is parallel and centered on the z-axis (rotation axis). Reconstruction slices are shown in in Fig. 5.14 with small amount of deviation introduced to d_x, d_z, θ_x, θ_y, and θ_z to simulate mis-calibration. We can see that even if d_x is perturbed by 0.5 mm, the resulting reconstruction slices present a ring structure around the object. When θ_y is changed by 1°, then the resulting reconstruction image slices also present a ring-structures, however, the size of this ring structure changes in different slices. A shift in d_z is similar to moving the object in the z-axis, so the reconstruction slice is located at a different vertical position on the object. A change in either θ_x and θ_z are less noticeable. In fact, even when θ_x or θ_z are perturbed by as much as 10°, the reconstruction slice shows little change. The length of R and R_f specify the x-ray magnification, so a mis-calibration in either one of the values results in the reconstructed object size to change. The size of the reconstructed object is also affected by the optical magnification. So when the object size is wrong in the reconstruction, it is difficult to know whether the error is due to a mistake in optical magnification or mis-calibration in R and R_f. For more on how to use the reconstruction program, refer to Appendix B.

5.5 Summary

In this chapter we have described the reconstruction method used for the prototype CT system. We first began by providing an overview of different types of reconstruction techniques. Then, we described the MLEM method that was used in our system. The forward and backward projectors were calculated based on Siddon's

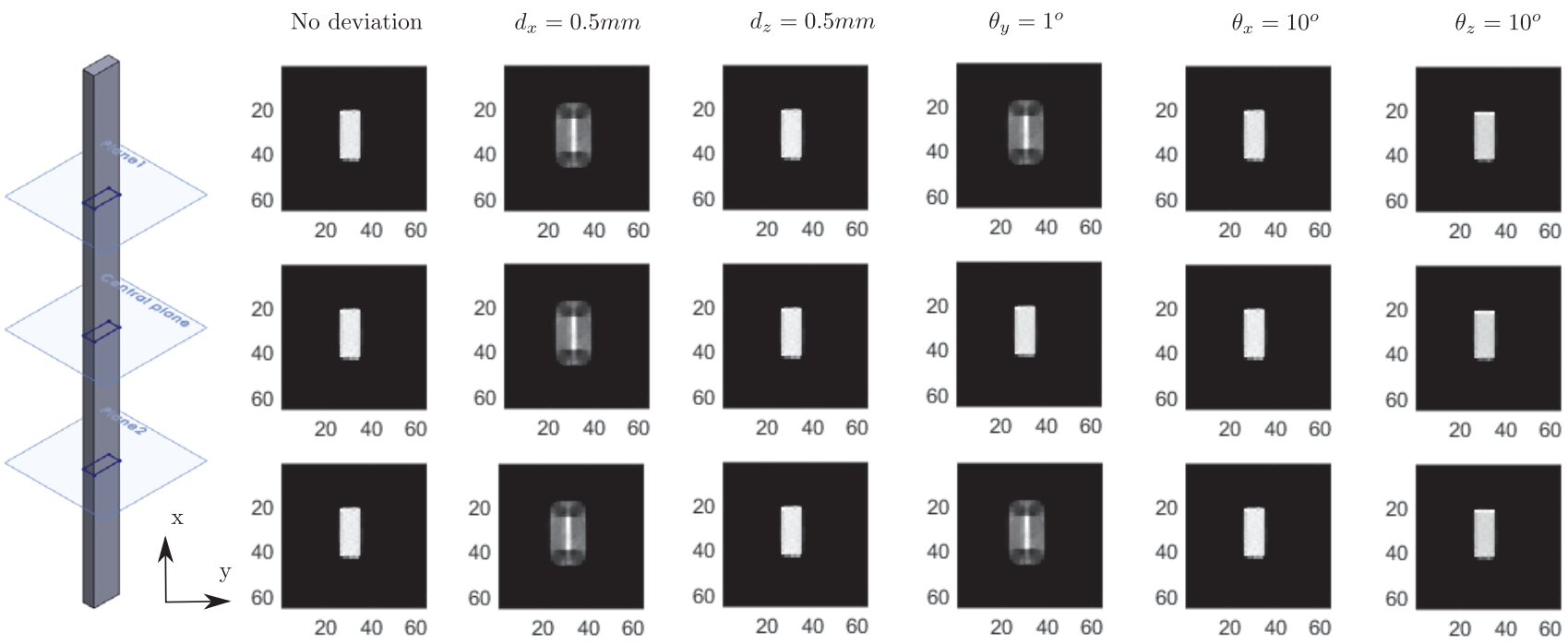

Figure 5.14: Reconstruction slices of a thin rectangular box when small deviations were presented at various parameters.

method and the entire reconstruction algorithm was implemented on the GPU. We have shown a reconstructed object and noted some of the artifacts that can be created by mis-calibrating the system. The reconstruction code is sourced controlled using git, and a copy of the reconstruction code can be pulled from a public repository at: `https://hxfan@bitbucket.org/hxfan/ct_reconstruction.git`.

CHAPTER 6

CONCLUSIONS AND FUTURE WORK

The introduction chapter gave a brief overview of the two types of digital radiography systems used in the market today. In both types of systems, the size of the detector panel is equal to the size of the x-ray image. We have discussed a type of DR system where a lens is used to image an x-ray phosphor screen onto a digital camera. In order to cover a large field of view, the lens demagnifies the visible-light image created by the phosphor onto the camera sensor. One motivation behind the lens-coupled digital x-ray detector system was that it can be used in countries where access to modern medicine can be difficult. We provided the equations to calculate the collection efficiency for the lens-coupled system in chapter 1.

In chapter 2, we demonstrated this idea by building a low-cost portable digital radiography unit (with special thank you to Brian Miller, Jared Moore, Stephen Moore, Heather Durko, and Lars Furenlid). Pictures taken in Nepal using the hospital x-ray source were compared to images taken with our system and their the film-screen technique. We observed that the method used to develop x-ray films was less controlled in the Nepalese villages compared to the methods that were used in the US. As a result, spots was observed in the x-ray film. These spots are non-existent in the image acquired using our system.

In chapter 3, we simulated a computed-tomography system to calculate the performance of a lens-coupled detector system using the channelized-Hotelling observer. We found that the angular correlation information in the data can be used to calculate signal detectability. This method can be very useful in optimizing an imaging system.

In the planar imaging system, we have observed the effect of blur by the phosphor

screen and the camera lens by measuring the system resolution and the noise power spectrum. The noise power spectra were measured for the three different cameras described in chapter 2, and for three different magnifications. These experiments were described in Appendix D. In the near future, we would like to look at the effect of the blur by comparing the three cameras for a signal detection task with different number of incident x-ray photons and with different number of photoelectrons per x-ray photons. We would also like to observe the effect of blur for a camera by comparing its performance in uniform and lumpy background for a range of x-ray photons.

The planar imaging system worked very well, and we were also interested in applying the same concept to a computed tomography (CT) system. The construction of this system was shown in chapter 2. This prototype CT system can be used to test the performance of the lens-coupled concept using different cameras. It is capable of acquiring projection images by rotating an object over 360 degrees. Once the system was built and the hardware units were integrated in LabView, the calibration of the system was described in chapter 4. An iterative reconstruction algorithm for the system was written using CUDA. This reconstruction algorithm and results of the CT reconstruction using a DSLR camera were presented in chapter 5.

While we were constructing the CT system, both Nikon and Leica released newer cameras using large sensors that do not have color filters. The one by Nikon is a CMOS senor while the Leica uses a CCD. The specification of the Nikon camera indicated that it has a much higher quantum efficiency in the Gd_2O_2S:Tb's emission spectrum. It will be very interesting to test the camera and compare its performance with the Princeton and Andor camera. It will also be interesting to test the performance of these cameras using columnar CsI instead of Gd_2O_2S:Tb to see if spatial resolution can be improved. However a large CsI will be expensive. The ability to scan in helical orbit can be implemented to improve the CT system. Finally the detective quantum efficiency of the detector system can be measured and compared to other commercial DR systems.

APPENDIX A

PARTS LIST

A.1 CT system-shutter

Component	**Manufacturer/Vendor**	**Part NO.**
Rotary solenoid	Ledex	H-2995-025
Shutter plate	Tungsten Heavy Powder & Parts	custom
Optical switch	Digikey	OPB-981-T51Z

Table A.1: Main components used for the shutter.

Symbol	Part Number/Value	Description
U1	SN74AHC1G04	Single schmitt-trigger inverter gate
U2	LM556	Dual timer
U3	SN74ACT08	Quadruple 2-input positive-AND gates
C1	10 nF	Capacitor
C2	680 nF	Capacitor
C3	10 nF	Capacitor
C4	10 nF	Capacitor
R1	100 kΩ	Resistor
R2	51 kΩ	Resistor
R3	24 kΩ	Resistor
R7	100 Ω	Resistor
R8	100 Ω	Resistor
R9	510 Ω	Resistor
R10	510 Ω	Resistor
D1-D3	1N4148W-TP	General Purpose diodes
N/A	100 nF	Capacitors for the back of the board

Table A.2: Components used for the solenoid board

APPENDIX B

RECONSTRUCTION CODE

The reconstruction code can be pulled from a public repository at: `https://hxfan@bitbucket.org/hxfan/ct_reconstruction.git`.

The main class used to calculate image reconstruction is called: siddon_recon. This class has three main functions, a1_FORWARD_PROJECTION(), a1_RECON_MLEM(), and a1_BACKWARD_PROJECTION. The function that is used to for image reconstruction is called a0_RECON_MLEM, which is an iterative MLEM algorithm. The forward and backward projection functions can be used for simulation. The forward projection function can be used to calculate projection images of a simulated phantom. This function can be very helpful in diagnosing problems occurred in the reconstruction due to a mis-calibration especially when the simulated phantom can be printed using a rapid prototype printer. Phantoms designed in SolidWorks can be used as input in the forward projection function. For detail converting SolidWorks models to binary file is found in Jared Moore's dissertation (Moore, 2011).

The input for all three functions is a configuration text file, which sets the geometry of the CT system, detector size, object volume, and scan parameters. This text file is used to modified the parameter values without recompiling the reconstruction code. The configuration file also includes the file paths of the projection images for the reconstruction and backward projection function, and the object volume file name for the forward projection function. The file paths were setup so the images used in the backward projection and reconstruction function do not need to be loaded into the computer's RAM all at once, which saves a lot of the computer's memory since the projection images can be quite large.

Once the reconstruction code is compiled, the program will first check for data files and size consistencies against the values in the configuration file before proceeding to do any calculations. However, it will not check for the memory size so one must make sure both the host and device has enough RAM for the calculation. As a default setting, after each MLEM iteration, the reconstruction function will write the reconstructed object to a file in the folder set in the configuration file, if the folder is left empty, then folder that house the projection images will be used. A configuration file will also be written to the same file location as the reconstructed object at the end of the execution to record the values that was used in reconstruction algorithm. This file has the extension, ".info" to differentiate between the input configuration file that normally has the extension ".cfg". All outputs of the functions are written in binary in "little-endian" as floats. The inputs used in the functions are also required to be saved in the same format.

The origin, (0, 0, 0), is located at the center of the object volume. A shift can be added to the object volume under "object parameters". The default detector center is calculated with respect to the number of transaxial and axial pixels, a shift can be added to indicate that the projection images on detector are shifted. This can be useful if the projection images from the camera are cropped with a shift off-center.

The version control software, git, can be downloaded at: `http://git-scm.com/`. It can be used for any types of files, such as LabView vis, MatLab scripts, C++/C files, and tex files. A quick tutorial can be found at `http://git-scm.com/docs/gittutorial`.

APPENDIX C

MOFFITT MULTI-MODALITY IMAGING SYSTEM

C.1 Introduction

The Moffitt box is a multi-modality imaging system that was built to image tumor cells grown within the window chambers on mice. In addition to white light, the system can be used to detect and track cell growth by imaging the red and green fluorescent proteins that were transfected on the tumor cell lines in mice. The system can also be used to image positrons and electrons emitted from radiopharmaceuticals, which are injected into mice to track cancer cells and their growth. The system has also been shown to image Cherenkov radiation. The design of the system was inspired by Dr. Katherine Creath. This imaging system was built and later delivered to the Moffitt Cancer Center in Florida on 2/7/2011.

C.2 Design and Construction

The exterior chamber of the system is constructed by welding 1/16″ steel plates to avoid light leaks at the corners and edges of the enclosure. The exterior of the chamber was powder coated to create a black matte finish. The welding and powder coating was provided by R&R Electrical Manufacturing Co. in Tucson. The interior of the chamber was spray painted in-house using Nextel Suede-coating 3101 and 5523 primer to minimize reflection with the inner chamber surfaces. A copper plate and a grounding cable were attached to the outside of the chamber to avoid static charges from building up on the chamber surfaces. Ten individual openings located in a small unit at the back of the chamber allow various cables to be fed through. The front and back of the system are shown in Fig. C.1.

Figure C.1: The (a) front and (b) back of the Moffitt imaging system.

(a) **(b)**

Figure C.2: (a) The light source used on the Moffitt box and (b) a light pipe supported by a flexible arm and magnetic base inside the chamber.

The Moffitt imaging system uses a powerful Xenon white light source (MAX-302, 300W Asahi Spectra). The light source can house up to eight 25 mm color filters, which can be used to adjust the spectrum of the output light. These filters are used to excite the tumor cells within the window chamber that were transfected with fluorescence protein. Filters for both red fluorescent and green fluorescent proteins were purchased for the Moffitt imaging system. The output of the light source is connected to dual-head light pipes (purchased from Asahi Spectra), and are inserted through the top of the chamber. Light-tight seals are applied at the entrances using pipe grommets and black silicone caulk. Black heat-shrink tubes are used to cover the light pipes to avoid reflection with the pipe's surfaces inside the chamber. Two flexible and adjustable arms with magnetic-base are used to hold the light pipe tips, and are used to adjust the illuminations on the window chamber. These were purchased from McMaster-Carr. The light source and one of the flexible arms are shown in Fig. C.2.

The images are captured using an ultra-sensitive CCD camera that is mounted to the top of the chamber with an opening for the CCD sensor. The camera used is the PIXIS 2048B from Princeton Instruments. A rubber gasket is placed between the front surface of the camera and the chamber's top surface to create a light-tight seal. Typically, two F/1.2 50mm lenses are mounted in a snout-to-snout fashion with

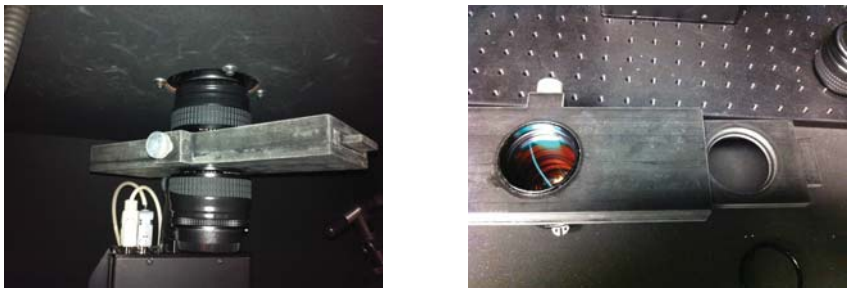

(a) **(b)**

Figure C.3: (a) The filter slide can be mounted between two 50 mm lens and can accommodate up to three emission filters.

both lenses set to focus at infinity in order to achieve unit image magnification. The Moffitt system also includes a telephoto lens, which allow images to be taken under different magnifications. Various magnifications can be adjusted by changing the focal length of the telephoto lens. The focal lengths ratio between the two lenses provides the magnification of the imaging system. A filter slide was designed and printed using rapid prototype printer. This slide contains two pieces, an outer housing that is used to attach the lenses at the front snout, and an inner tray so emission filters can be placed inside. For red fluorescent protein (RFP), we excited the protein with a filter centered at 561 nm (bandwidth = 14 nm), and collected the light emission using a filter centered at 609 nm (bandwidth 54 = nm). For green fluorescent protein (GFP), we used a filter centered at 482 nm (18 nm) for excitation, and a filtered at 525 nm (45 nm) for emission. The filter selection can be adjusted by pulling the plunger and sliding the inner tray to the target filter position. The lens and filter slide are shown in Fig. C.3.

The mouse with window chamber can be secured by a plastic holder. The plastic holder is machined with three small holes so screws from the window chamber can be placed inside to ensure the mouse does not move during experiments. The plastic holder is placed on a horizontal platform that is connected to a vertical translation stage. During experiments, the window chamber is adjusted into the focus of the camera and lens system by moving the vertical stage (Newmark NLS8 500 mm).

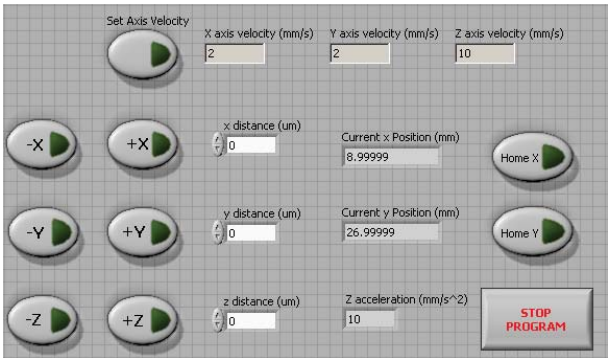

Figure C.4: Program front panel to control horizontal and vertical stages.

Two horizontal stages each controlled with a linear actuator are used to change the lateral positions of the window chamber on the platform. The vertical and horizontal stages are communicated through their respective motion controllers using a program written in LabView. The front panel of the LabView program is shown in Fig. C.4. A modification was made to the vertical motion controller so the LED limit switches that were used on the stage can be turned off during image acquisition. The modification was done by toggling the power to the LEDs using an unused serial cable pin on the motion controller. The voltages to the serial pin were used to turn the limit switch LEDs on and off. This modification was done with helps from Dr. Lars Furenlid.

For fluorescence imaging, the appropriate excitation and emission filters are selected for the target protein labeled on the cells. For electron or positron imaging, a thin scintillator film is placed on top of the window chamber with the glass covering removed so the visible photons emitted from the scintillator film by incident charged particles are collected onto the camera sensor. For more information regarding the imaging techniques, refer to Liying's work (Chen et al., 2009). Images of a mouse's window chamber taken under white light, fluorescence from RFP, and electrons from 18-F are shown in Fig. C.5.

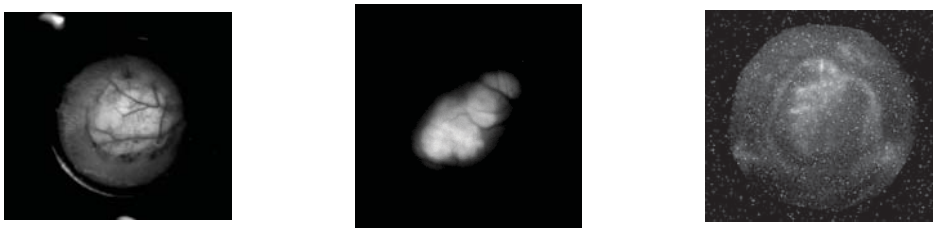

(a) **(b)** **(c)**

Figure C.5: The image acquired with a window chamber using (a) white light, (b) fluorescence from RFP, and (c) visible light emitted from the scintillator film created by incident electrons, which are released by the injected FDG-18F.

APPENDIX D

NOISE POWER SPECTRUM COMPARISON

We have acquired x-ray images using three different digital cameras, the Andor Neo, the Princeton PIXIS 2048B and the Nikon D700 that were described in chapter 2. Each camera was placed behind an x-ray screen (Lanex Gd_2O_2S:Tb) and a commercial lens (Nikkor F1.4G 50 mm) was used to couple the image from the x-ray phosphor screen onto the camera sensor. Each lens-camera system was placed at three different distances behind the phosphor screen, and uniform x-ray flood images were acquired at different magnification settings. The highest magnification was 1, where a 1 mm sized image at the x-ray screen produces a 1 mm sized image on the camera sensor. This was done by using two identical lenses so the entrance pupil of one lens is adjacent to the other, with both lenses set to focus at infinity, as shown in Fig. D.1. The images acquired with the two magnifications less than one were performed using only one lens, and the cameras were placed away from the screen so the magnfication equals to 1/6.5 and 1/13.5 (i.e. a 1 mm object at the screen produces a 1/6.5mm and 1/13.5mm image at the detector respectively). All images were acquired using the same camera integration time (5 seconds) and x-ray tube setting (90 kVp 0.4 mA).

We have demonstrated previously that the lens itself is capable of stopping majority of direct x-rays without any damage to the camera sensor. However, scattered x-ray photons can still enter the camera sensor. For the highest magnification (m = 1), the lens pairs and camera were placed inside a lead-lined box with an open entrance for the lens. This box was used to prevent scattered x-rays from hitting the camera sensors. Images taken at the latter two magnifications were acquired by placing a 45° folding mirror between the x-ray screen and the camera to avoid direct

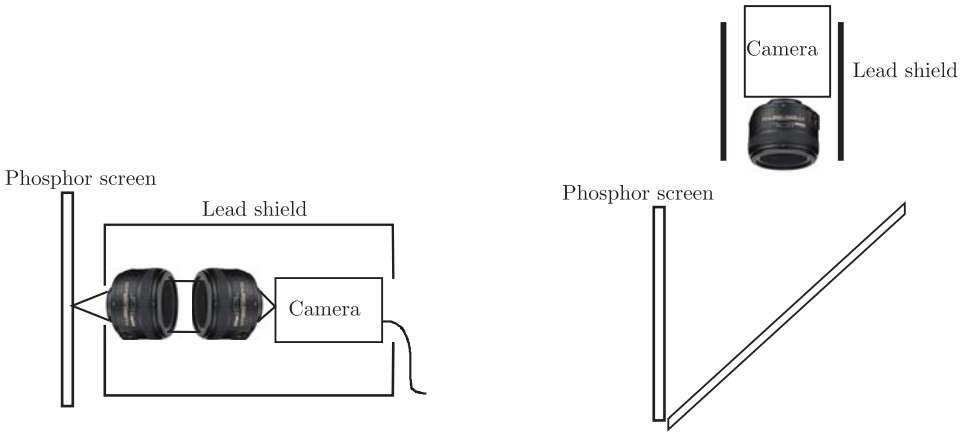

Figure D.1: The setups to acquire images for magnifications = 1, 1/6.5 and 1/13.5.

x-rays. Additional lead shields were placed around the camera to reduce scattered x-rays from hitting the sensor.

D.1 Measuring noise power spectra

The typical way of measuring noise power spectrum (NPS) is to use one x-ray flood image and divide it into smaller non-overlapping regions. Each smaller region is then de-trended to eliminate background non-uniformity in the image before a two-dimensional Discrete Fourier Transform (DFT) is applied to each region (Dobbins III et al., 2006; Samei and Flynn, 2003; Zhou et al., 2011). The two-dimensional noise power spectrum image is calculated by computing the variance over the number of image regions from the same x-ray image. The assumption is that after de-trending, the remaining noise in each image region is due to the noise in the detector. The second assumption is that there are no correlations between opposite ends of each image region. Since the DFT only diagonalizes a circulant matrix, while the continuous Fourier tranform diagonalizes a Toeplitz matrix. This method ignores any wrap-around effect the DFT can contribute and any-off diagonal component in the covariance matrix is assumed to be zero.

A more tedious method of measuring NPS, but one that requires fewer assump-

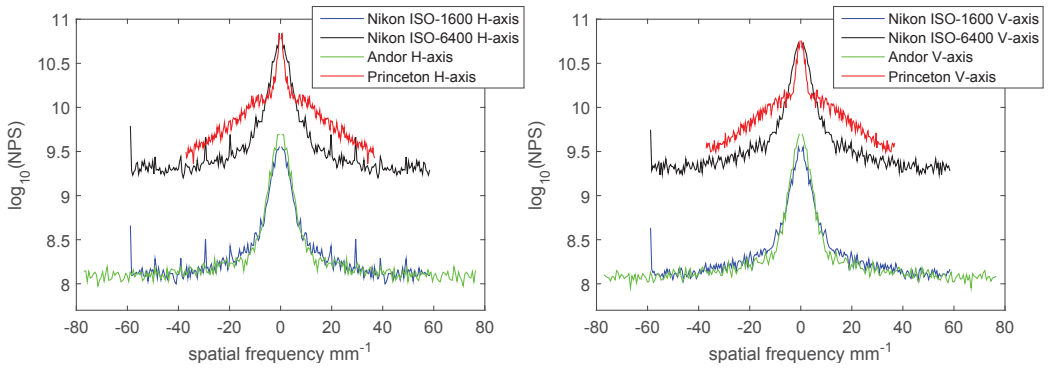

Figure D.2: The central horizontal and vertical axis of the 2-D NPS measured at m = 1.

tion, is to repeat the same x-ray measurement multiple times and extract only one uniform region from each image. The NPS is then calculated over a succession of images rather than smaller regions of the same image. This was done in all of our noise power spectrum measurements.

The NPS for each camera is calculated using two sets of data acquired while the x-ray tube was turned on. One set of 100 repeated x-ray flood images, and one set of 100 repeated dark images taken with the lens cap in place. A smaller uniform section of 256 × 256 pixels was extracted from each full-sized x-ray flood image and the variance of the DFT coefficients were computed across the 100 images. This calculation was also performed on the same section of 256 × 256 pixels extracted from the set of dark images. The one-dimensional NPS is then plotted in log scale at the central axis of the two-dimensional NPS image in both the horizontal and vertical directions.

D.2 Results

The horizontal and vertical axis of the two-dimensional NPS measured at magnification = 1, 1/6.5 and 1/13.5 are shown in Fig. D.2 - D.4, where the log of the noise power spectrum is plotted against spatial frequency.

The NPS for each camera cuts off at different frequencies because they were

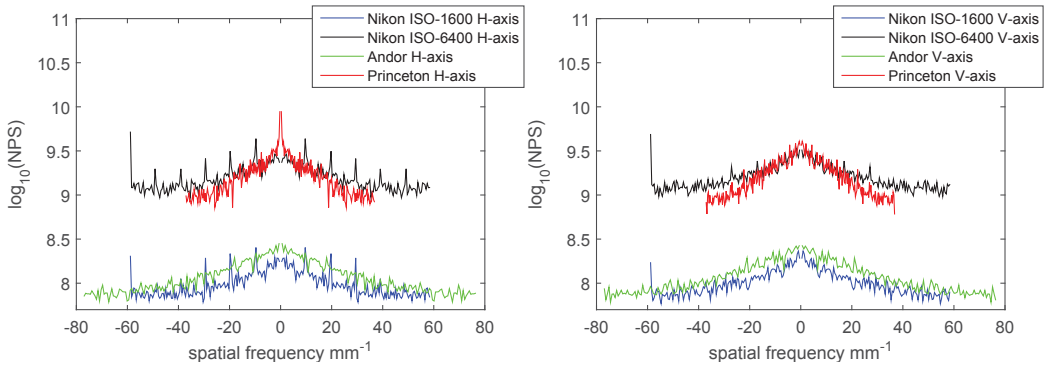

Figure D.3: The central horizontal and vertical axis of the 2-D NPS measured at m = 1/6.5.

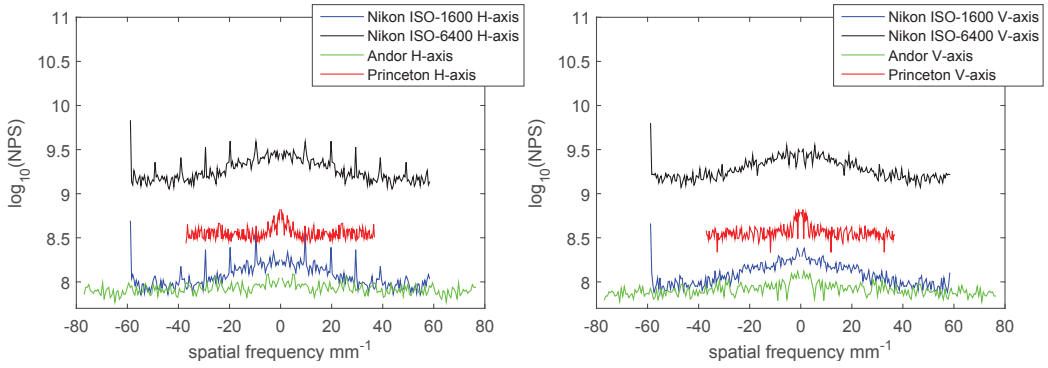

Figure D.4: The central horizontal and vertical axis of the 2-D NPS measured at m = 1/13.5.

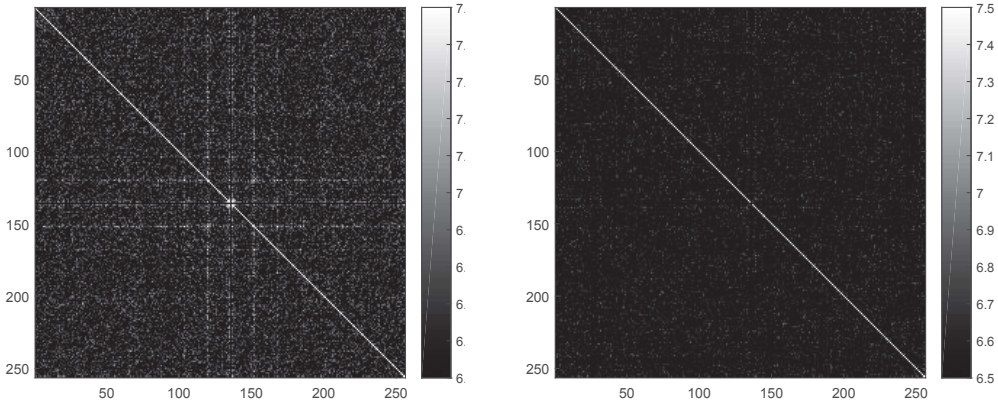

Figure D.5: Covariance matrices calculated using 100 images taken with the Andor Neo camera at magnification = 1 and 1/13.5. Each image region is 16×16 pixels.

all calculated using image regions with the same number of pixels (256 × 256), but each camera has a different pixel size. The sampling cut-off frequency for the camera with largest pixel size (Princeton) is lower than for the D700 and the Neo that have smaller pixel sizes.

The NPS measured at magnification = 1 for all three cameras exhibit a Gaussian peak centered at the zeroth spatial frequency. These were not seen at the two lower magnifications. The Gaussian peak is due to the spatial blur created by interacting x-ray photons at the phosphor screen and the effect of the point spread function by the lens.

The diagonal elements of the covariance matrix calculated using the DFT coefficients are the two-dimensional NPS, while the off-diagonal elements are often ignored. Fig. D.5 - D.7 show the covariance matrices calculated using 100 images each with 16 × 16 pixels taken at magnification = 1 and magnification = 1/13.5. The off-diagonal elements can clearly be seen in the images taken at unit magnification compared to images taken at lower magnification.

There was little difference between the horizontal and vertical axis of the NPS

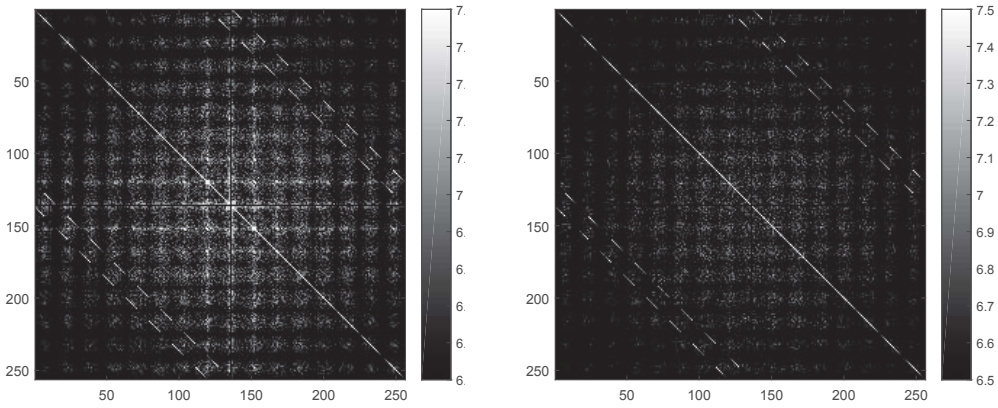

Figure D.6: Covariance matrices calculated using 100 images taken with the Nikon D700 at magnification = 1 and 1/13.5. Each image region is 16×16 pixels.

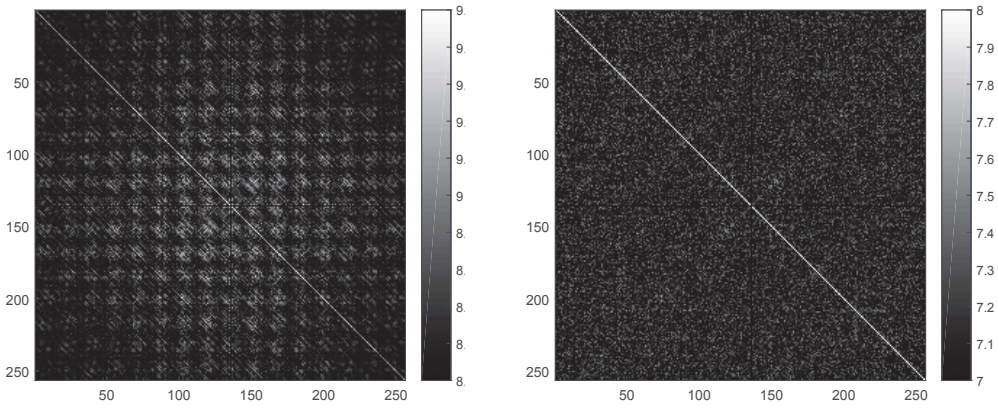

Figure D.7: Covariance matrices calculated using 100 images taken with the Princeton PIXIS camera at magnification = 1 and 1/13.5. Each image region is 16×16 pixels.

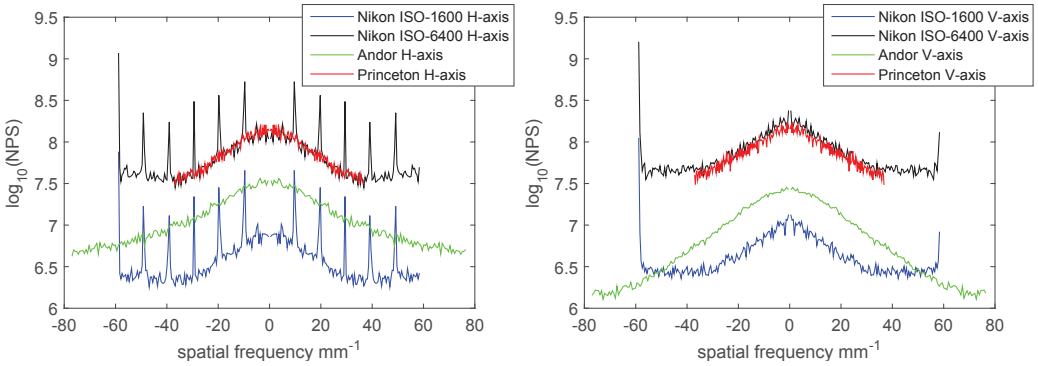

Figure D.8: The central horizontal and vertical axis of the 2-dimensional NPS measured using dark frames acquired with the x-ray tube turned on.

measured in both the Princeton and the Andor cameras under all three magnification settings. The Nikon D700 has 12 parallel high-speed readout channels that allows the voltage signals from multiple columns to be read out simultaneously. The parallel readout process shows up on the NPS in the horizontal axis as periodic sharp peaks. This effect can be seen more clearly in the NPS calculated using the set of dark images, shown in Fig. D.8.

The noise power spectra of the dark images for all three cameras are not flat, which can be caused by scattered x-rays interacting directly with the camera sensors. Although the majority of direct and scattered x-rays are stopped by either the lens or the lead shields, a few scattered x-rays photons will inevitably land on the sensor. Each scattered x-ray photon shows up in the image as a small cluster of high-valued pixels. In order to account the effects of these scattered x-ray photons on the overall noise power spectrum, a set of dark images were taken using a lens cap while the x-ray tube is turned on so the scattered x-rays are also present in the dark frames. The noise power spectra shown in Fig. D.2 - D.4 were the final result after subtraction with the NPS calculated using these dark images.

We verified the effects of scattered x-rays on the noise power spectrum by taking another set of dark images without turning on the x-ray tube. These plots are shown in Fig. D.9. In both the Andor and the Princeton cameras, the noise power

spectra are flat, which indicates that only white noise is present in the dark frames. The Nikon D700's NPS indicates that there is inherent noise pattern on the sensor. Contrary to both scientific cameras, we noticed that the effects of scattered x-ray photons were not present in the images taken with the Nikon D700. Also, the values in the dark images from the D700 were close to zero although there is no cooling capability. We credit these differences and the patterns shown in the dark NPS to the proprietary on-board image processing algorithm used by the camera. This algorithm, which actively suppresses noise and thresholds each image before it is read out, cannot be turned off. The use of this algorithm also explains why there are few differences between the NPS of the dark images taken with the x-ray tube turned on and the images acquired with the x-ray tube turned off using the D700 camera. A smaller difference in the magnitude of the noise is observed between the two sets of dark images taken with the Andor camera compared to the Princeton CCD camera. This is because the Andor camera also has an on-board noise suppressing filter that corrects hot pixels by replacing the noisy pixels with the mean values of the neighboring pixels. However, the filter used in the Andor camera is not as robust as the one used in the D700, so the effects of scattered x-ray photons are still seen in images acquired with the Andor camera . The Princeton CCD does not have noise suppressing capability, so the effects of scattered x-ray photons are much more prominent. As a result, the NPS of the dark images taken with the Princeton camera is higher than both the Andor and Nikon cameras.

The NPS level on the horizontal axis is higher than on the vertical axis for the Andor camera. This level is shown in the NPS of the dark images taken with and without x-rays, Figs. D.8 and D.9. We have noticed that the dark frames of the Andor camera exhibit striping patterns in the column direction as shown in Fig. D.10. We contribute this to the fact that each column in the Andor sensor uses a different amplifiers so small variations between these column amplifier cause small differences in the horizontal and vertical axis of the NPS. We verify this presence by looking at one dark image. When the dark image is summed over columns and rows,

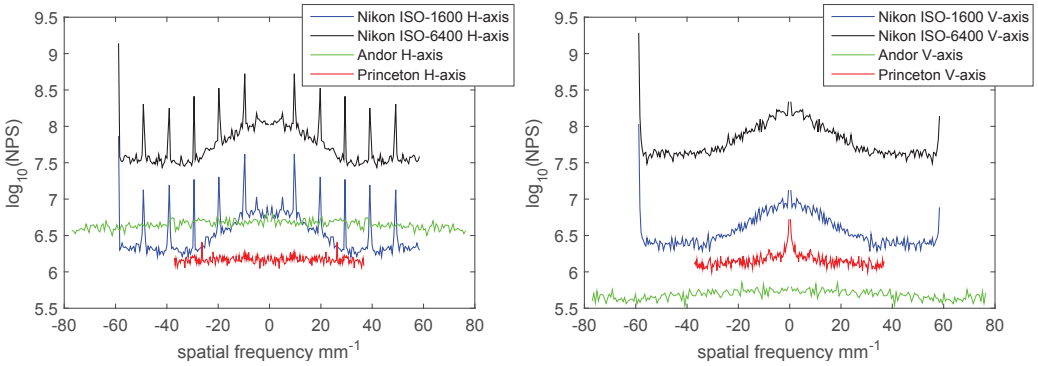

Figure D.9: The central horizontal and vertical axis of the 2-D NPS measured using dark frames acquired without x-rays.

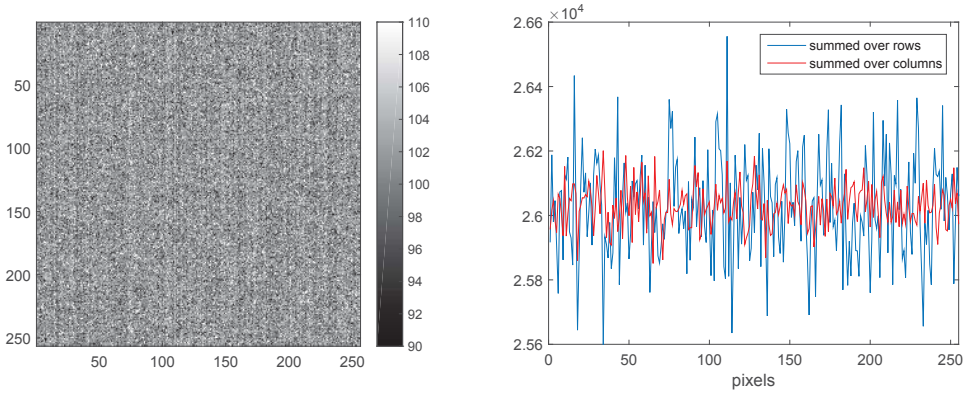

Figure D.10: Left: a dark image taken with the Andor sCMOS camera, showing the stripping pattern. Right: The result of the same dark image when summed over rows and columns.

the noise variance across columns is higher than the noise variance across rows, seen in Fig. D.10.

In traditional film photography, the ISO-number indicates the sensitivity of the film to light level, often referred as the speed of the film. Bright scenes are taken using low speed films and darker environments are taken with films that have a higher ISO-number. This concept is carried over to consumer-grade digital cameras even though they do not employ film. The ISO-number on a DSLR indicates that the sensor will behave in a way similar to a film with the same ISO at the same light level. While changing the ISO in a film camera involves switching to a different film,

the sensor used in a DSLR cannot be changed. The sensitivity of the detector, the number of photoelectrons produced at a particular light level, does not change under different ISO settings in a DSLR camera. The variations in ISO setting is achieved by selecting different reference voltages used by the gated integrator. The same number of photoelectrons produced at different ISO settings are assigned to different output values by the analogue-to-digital converter (ADC) after amplification. This method produces a nosier image at higher ISO settings because the small amount of noise present in the electronic circuit that would otherwise be assigned to values closer to zero at low ISO is amplified and assigned to much larger values. The result is seen in the difference between the noise spectra calculated using images taken by the Nikon D700 at ISO-1600 and at ISO-6400. The NPS differ by a factor of 16, which translates to signal gain of 4 from images taken at ISO-1600 to those taken at ISO-6400.

REFERENCES

AAPM (2006). Acceptance Testing and Quality Control of Photostimulable Storage Phosphor Imaging Systems. Technical report, American Association of Physicists in Medicine.

Abbey, C. K. (1998). *Assessment of reconstructed images*. Ph.D. dissertation, University of Arizona, Tucson, AZ.

Abbey, C. K. and F. O. Bochud (2000). *Handbook of Medical Imaging*, volume I. Physics and Psychophysics, chapter 11. Modeling Visual Detection Tasks in Correlated Image Noise with Linear Model Observers, pp. 630–654. SPIE Press.

Azevedo, S. G., D. J. Schneberk, J. P. Fitch, and H. E. Martz (1990). Calculation of the rotational centers in computed tomography sinograms. *IEEE Trans. Nucl. Sci.*, **37**, pp. 1525–1540.

Barrett, H. H. and C. K. Abbey (2001). Human- and model-observer performance in ramp-spectrum noise: effects of regularization and object variability. *J. Opt. Soc. Am. A Opt. Image. Sci. Vis.*, **18**(3), pp. 473–488.

Barrett, H. H., M. A. Kupinski, S. Müeller, H. J. Halpern, J. C. Morris III, and R. Dwyer (2013). Objective assessment of image quality VI: imaging in radiation therapy. *Phys. Med. Biol.*, **58**, pp. 8197–8213.

Barrett, H. H. and K. J. Myers (2004). *Foundations of Image Science*. John Wiley & Sons, Inc.

Beister, M., D. Kolditz, and W. A. Kalender (2012). Iterative reconstruction methods in X-ray CT. *Physica Medica*, **28**, pp. 94–108.

Burgess, R. E. (1959). Homophase and heterophase fluctuations in semiconducting crystals. *Discuss. Faraday Soc.*, **28**, pp. 151–158.

Busemann-Sokole, E. (1987). Measurement of collimator hole angulation and camera head tilt for slant and parallel hole collimators used in SPECT. *J. Nucl. Med.*, **28**, pp. 1592–1598.

Bushberg, J. T., J. A. Seibert, E. M. Leidholdt Jr., and J. M. Boone (2002). *The essential physics of medical imaging*. Lippincott Williams & Wilkins.

Chen, G. H. (2003). A new framework of image reconstrution from fan beam pprojections. *Med. Phys.*, **30**, pp. 1151–1161.

Chen, L., L. S. Gobar, N. G. Knowles, D. W. Wilson, and H. H. Barrett (2009). Direct Charged-Particle Imaging System Using an Ultra-Thin Phosphor: Physical Characterization and Dynamic Applications. *IEEE Trans. Nucl. Sci.*, **56(5)**, pp. 2628–2635.

Cherepy, N., S. A. Payne, S. J. Asztalos, F. Hull, J. D. Kuntz, T. Niedermayr, S. Pimputkar, J. J. Roberts, R. D. Sanner, T. M. Tillotson, E. van Loef, C. M. Wilson, K. S. Shah, U. N. Roy, R. Hawrami, A. Burger, L. A. Boatner, W. S. Choong, and W. W. Moses (2009). Scintillators with Potential to Supersede Lanthanum Bromide. *IEEE Trans. Nucl. Sci.*, **56(3)**, pp. 873–880.

Cho, Y., D. J. Moseley, J. H. Siewerdsen, and D. A. Jaffray (2005). Accurate technique for complete geometric calibration of cone-beam computed tomography systems. *Med. Phys.*, **32**, pp. 968–983.

Clark, R. N. (2014). Digital Camera Reviews and Sensor Performance Summary. http://www.clarkvision.com/imagedetail/digital.sensor.performance.summary/.

CNET (2004). Sigma SD10 review. `http://www.cnet.com/products/sigma-sd10/`.

Crawford, C. R., G. T. Gullberg, and B. M. Tsui (1988). Reconstruction for fan beam with an angular-dependent displaced center-of-rotation. *Med. Phys.*, **15**, pp. 67–71.

Digicams, S. (2003). SIGMA SD10 FOVEON, Steve's Conclusion. `http://www.steves-digicams.com/2003_reviews/sigma_sd10_pg7.html`.

Dobbins III, J. T., J. Sain, N. T. Ranger, and Y. Chen (2006). Intercomparison of methods for image quality characterization. II. Noise power spectrum. *Med. Phys.*, **33(5)**, pp. 1466–1475.

Fahrig, R., A. Ganguly, P. Lillaney, J. Bracken, J. A. Rowlands, Z. Wen, H. Yu, V. Rieke, J. M. Santos, K. B. Pauly, D. Y. Sze, J. K. Frisoli, B. L. Daniel, and N. J. Pelc (2008). Design, performance, and applications of a hybrid X-Ray/MR system for interventional guidance. *Proc. IEEE*, **96**, pp. 468–480.

Feldkamp, L. A., L. C. Davis, and J. W. Kress (1984). Practical cone-beam algorithm. *J. Opt. Soc. Am. A*, **1**(6), pp. 612–619.

Foveon (2010). X3 Technology. `http://www.foveon.com`.

Gagne, R. M., J. S. Boswell, and K. J. Myers (2003). Signal detectability in digital radiography: Spatial domain figures of merit. *Med. Phys.*, **30**(8), pp. 2180–2193.

Gallas, B. D. and H. H. Barrett (2003). Validating the use of channels to estimate the ideal linear observer. *J. Opt.Soc. Am. A*, **20**, pp. 1725–1738.

Graham, L. E., M. Zimmerman, K. J. Vassallo, V. Patterson, P. Swinfen, R. Swinfen, and R. Wootton (2003). Telemedicine–the way ahead for medicine in the developing world. *Trop. Doct.*, **33**, pp. 36–38.

Grangeat, P. (1991). Mathematical framework of cone beam 3D reconstruction via the first derivative of the radon transform. In Herman, G. T., L. A. K., and N. F. (eds.) *Mathematical Methods in Tomography*, volume 1497 of *Lecture Notes in Mathematics*, pp. 66–97. Springer Berlin Heidelberg.

Greivenkamp, J. E. (2004). *Field Guide to Geometrical Optics*. SPIE Press.

Gullberg, G. T., B. Tsui, C. R. Crawford, J. G. Ballard, and J. T. Hagius (1990). Estimation of geometric parameters and collimator evaluation for cone beam tomography. *Med. Phys.*, **17**, pp. 264–272.

Gullberg, G. T., B. M. W. Tsui, C. R. Crawford, and E. R. Edgerton (1987). Estimation of geometric parameters for fan beam tomography. *Phys. Med. Biol.*, **32**, pp. 11581–1594.

Hajdok, G., J. Yao, J. J. Battista, and I. A. Cunningham (2006). Signal and noise transfer properties of photoelectric interactions in diagnostic x-ray imagign detectors. *Med. Phys.*, **33(10)**, pp. 3601–3620.

Hejazi, S. and D. P. Trauernicht (1997). System considerations in CCD-based x-ray imaging for digital chest radiography and digital mammography. *Med. Phys.*, **24**, pp. 287–297.

Hesterman, J. Y., L. Caucci, M. A. Kupinski, H. H. Barrett, and L. R. Furenlid (2010). Maximum-likelihood estimation with a contracting-grid search algorithm. *IEEE Trans. Nucl. Sci.*, **57**(3), pp. 1077–1084.

Hsieh, J. (1999). Three-Dimensional Artifact Induced by Projection Weighting and Misalignment. *IEEE Trans. Med. Imag.*, **18**, pp. 364–368.

Hsieh, J., B. Nett, Z. Yu, K. Sauer, J. B. Thibault, and C. A. Bouman (2013). Recent Advances in CT Image Reconstruction. *Curr. Radiol. Rep.*, **1**, pp. 39–51.

Hu, H. (1996). An improved cone-beam reconstruction algorithm for the circular orbit. *Scanning*, **18**, pp. 572–581.

ImPACT (2002). Four Slice CT Scanner Comparison Report. Technical report, Imaging Performance Assessment of CT Scanners.

Kachelrieß, M., S. Schaller, and W. A. Kalender (2000). Advanced single-slice rebinning in cone-beam spiral CT. *Med. Phys.*, **27**, pp. 754–772.

Kandaraks, I. and D. Cavouras (2001). Experimental and theoretical assessment of the Performance of Gd_2O_2S:Tb and La_2O_2S:Tb phosphor and Gd_2O_2S:Tb-La_2O_2S:Tb Mixtures for X-ray imaging. *Eur. Radiol.*, **11**, pp. 1083–1091.

Kasap, S. O. and J. A. Rowlands (2002). Direct-conversion flat-panel x-ray image detectors. *IEE Proc.-Circuits Devices Syst.*, **149**, pp. 85–96.

Kasap, S. O., M. Zahangir Kabir, and J. A. Rowlands (2006). Recent advances in X-ray photoconductors for direct conversion X-ray image detectors. *Curr. Appl. Phys.*, **6**, pp. 288–292.

Kato, H. (1994). *Specification, acceptance testing and quality control of diagnostic x-ray imaging equipment*. AAPM.

Katsevich, A. (2002). Theoretically exact filtered backprojection type inversion algorithm for spiral CT. *SIAM J. Appl. Math.*, **62**, pp. 2012–2026.

Katsevich, A. (2003). A general schedule for constructing inversion algorithm for cone beam CT. *Internat. J. Math. Math. Sci.*, **21**, pp. 1305–1321.

Katsevich, A. (2004). Improved exact FBP algorithm for spiral CT. *Adv. Appl. Math*, **32**, pp. 681–697.

Kieranmaher (2015). Basic Physics of Digital Radiography/The Patient. `http://en.wikibooks.org/wiki/Basic_Physics_of_Digital_Radiography/The_Patient`.

Kim, H. K., J. K. Ahn, and G. Cho (2005). Development of a lens-coupled CMOS detector for an X-ray inspection system. *Nucl. Instr. Meth. Phys. Res. A*, **545**, pp. 210–216.

Knoll, G. F. (2010). *Radiation detection and measurement*. Wiley.

Kudo, H. and T. Saito (1991). Helical-scan computed tomography using cone-beam projections. *IEEE Nucl. Sci. Symp. Med. Imaging Conf.*, **3**, pp. 1958–1962.

Lee, S. W., H. K. Kim, G. Cho, Y. H. Shin, and Y. Y. Won (2001). A 3-D X-Ray Microtomographic System With a CMOS Image Sensor. *IEEE Trans. Nucl. Sci.*, **48**, pp. 1503–1505.

Li, J., R. J. Jaszczak, K. L. Greer, and R. E. Coleman (1994a). A filtered backprojection algorithm for pinhole SPECT with a displaced center of rotation. *Phys. Med. Biol.*, **38**, pp. 165–176.

Li, J., R. J. Jaszczak, H. Wang, G. T. Gullberg, K. L. Greer, and R. E. Coleman (1994b). A cone-beam SPECT reconstruction algorithm with a displaced center of rotation. *Med. Phys.*, **21**, pp. 145–152.

Madden, T. J., W. McGuigan, M. J. Molitsky, I. Naday, A. McArthur, and E. M. Westbrook (2006). Lens-Coupled CCD Detector for X-ray Crystallography. *IEEE Trans. Nucl. Sci.*, **2**, pp. 729–734.

Magnan, P. (2003). Detection of visible photons in CCD and CMOS: A comparative view. *Nucl. Instr. Meth. Phys. Res. A*, **504**, pp. 199–212.

MaxMax.com (2014). B&W Conversion. `http://www.maxmax.com/b&w_conversion.htm`.

Moore, J. W. (2011). *Adaptive x-ray computed tomography*. Ph.D. dissertation, University of Arizona.

Mort, J. (1989). *The Anatomy of Xerography - Its Invention and Evaluation*. Jefferson, N.C. : McFarland.

Myers, K. J. (1985). *Visual perception in correlated noise*. Ph.D. dissertation, University of Arizona, Tucson, AZ.

Myers, K. J. and H. H. Barrett (1987). The addition of a channel mechanism to the ideal-observer model. *J. Opt. Soc. Am. A*, **4**, pp. 2447–2457.

Nagarkar, V., T. Gupta, S. Miller, Y. Klugerman, and M. Squillante (1997). Structured CsI(Tl) scintillators for X-ray imaging applications. *IEEE Nucl. Sci. Conf. Rec.*, **1**, pp. 226–230.

Nikl, M. (2006). Scintillation detectors for x-rays. *Meas. Sci. Technol.*, **17**, pp. R37–R54.

Noo, F., R. Clackdoyle, C. Mennessier, T. A. White, and T. J. Roney (2000). Analytic method based on idenficiation of ellipse parameters for scanner calibration in cone-bean tomography. *Phys. Med. Biol.*, **45**, pp. 3489–3508.

Noo, F., M. Defrise, and R. Clackdoyle (1999). Single-slice rebinning method for helical cone-beam CT. *Phys. Med. Biol.*, **44**, pp. 561–570.

NVIDIA (2014). *CUDA toolkit documentation*. NVIDIA, docs.nvidia.com/cuda/index.html, 5.5 edition.

Panetta, D., N. Belcari, A. D. Guerra, and S. Moehrs (2008). An optimization-based method for gegeometric calibration in cone-beam CT witwith dedicated phantoms. *Phys. Med. Biol.*, **53**, pp. 3841–3861.

Rougee, A., C. Picard, C. Ponchut, and Y. Trousset (1993). Geometrical calibration of x-ray imaging chains for three-dimensional reconstruction. *Comput. Med. Imaging Graph.*, **17**, pp. 295–300.

Rowlands, J. A. (2002). The physics of computed radiography. *Phys. Med. Biol.*, **47**, pp. R123–R166.

Rowlands, J. A. and J. Yorkston (2000). *Handbook of Medical Imaging, Volume 1. Physics and Psychophysics*, chapter Chapter 4. Flat panel detectors for digital radiography, pp. 223–329. SPIE Press.

Sain, J. and H. H. Barrett (2003). Performance Evaluation of a Modular Gamma Camera Using a Detectability Index. *J. Nucl. Med.*, **44**, pp. 58–66.

Samei, E. and M. J. Flynn (2003). An experimental comparison of detector performance for direct and indirect digital radiography systems. *Med. Phys.*, **30(4)**, pp. 608–622.

Siddon, R. L. (1985). Fast calculation of the exact radiological path for a three-dimensional CT array. *Med. Phys.*, **12(2)**, pp. 252–255.

Smekal, L., M. Kachelrieß, E. Stepina, and W. A. Kalendar (2004). Geometric misalignment and calibration in cone-beam tomography. *Med. Phys.*, **31**, pp. 2342–3266.

Smith, B. D. (1985). Image Reconstruction from Cone-Beam Projections: Necessary and Sufficient Conditions and Reconstruction Methods. *IEEE Trans. Med. Imag.*, **4**, pp. 14–25.

Smith, B. D. and J. X. Chen (1992). Implementation, investigation, and improvement of a novel cone-beam reconstruction method. *IEEE Trans. Med. Imag.*, **11**, pp. 260–266.

Tam, K. C., S. Samarasekera, and F. F. (1998). Exact cone beam CT with a spiral scan. *Phys. Med. Biol.*, **43**, pp. 1015–1024.

Tang, X., J. N. R. A. Hsieh, D. Sandeep, S. Dmitry, and H. Akira (2006a). A three-dimensional-weighted cone beam filtered backprojection (CB-FBP) algorithm for image reconstruction in volumetric CT - helical scanning. *Phys. Med. Biol.*, **51**, pp. 855–874.

Tang, X. Y. and J. Hsieh (2004). A filtered backprojection algorithm for cone beam reconstruction using rotation filtering under helical source trajectory. *Med. Phys.*, **31**, pp. 2949–2960.

Tang, X. Y., J. Hsieh, R. A. Nilsen, and S. M. McOlash (2006b). Extending three-dimensional weighted cone beam filtered backprojection (CB-FBP) algorithm for image reconstruction in volumetric CT at low helical pitches. *Int. J. Biomed. Imaging*, **2006**, pp. 1–8.

Tate, M. W., D. Chamberlain, and S. M. Gruner (2005). Area x-ray detector based on a lens-coupled charge-coupled device. *Rev. Sci. Instrum.*, **76**.

Tuy, H. K. (1983). An Inversion Formula for Cone-Beam Reconstruction. *SIAM J. Appl. Math.*, **43**, pp. 546–552.

Ulzheimer, S. and T. Flohr (2009). Multislice CT: Current Technology and Future Developments. In Reiser, M. F., C. R. Becker, K. Nikolaou, and G. Glazer (eds.) *Multislice CT*, Medical Radiology, pp. 3–23. Springer Berlin Heidelberg.

VIDISCO (2014). NDT Wiki X-ray - the Digital X-ray Encyclopedia. `http://www.vidisco.com/ndt_solutions/ndt_info_center/ndt_wiki_x_ray`.

Wagner, R. F., D. G. Brown, and M. S. Pastel (1979). Application of information theory to the assessment of computed tomography. *Med. Phys.*, **6**(2), pp. 83–94.

Wang, G. and M. Jiang (2004). Ordered-subset simultaneous algebraic reconstruction techniques (OS-SART). *J. Xray Sci. Technol.*, **12**, pp. 169–177.

Wang, G., T. H. Lin, P. Cheng, and S. D. M. (1993). A general cone-beam reconstruction algorithm. *IEEE Trans. Med. Imag.*, **12**, pp. 486–496.

Wang, G., T. H. Lin, P. C. Cheng, D. M. Shinozaki, and H. G. Kim (1992). Scanning cone-beam reconstruction algorithms for x-ray microtomography. *Proc. SPIE*, **1556**, pp. 99–112.

Wang, G., Y. Ye, and H. Yu (2007). Approximate and exact cone-beam reconstruction with standard and non-standard spiral scanning. *Phys. Med. Biol.*, **52**, pp. R1–R13.

Wang, G., H. Yu, and B. De Man (2008). An outlook on x-ray CT research and development. *Med. Phys.*, **35**, pp. 1051–1064.

Wang, H., M. F. Smith, C. D. Stone, and R. J. Jaszczak (1998). Astigmatic single photon emission computed tomography imaging with a displaced center of rotation. *Med. Phys.*, **25**, pp. 1493–1501.

Wang, Y., G. Baldoni, W. H. Rhodes, C. Brecher, A. Shah, U. Shirwadkar, J. Glodo, N. Cherepy, and S. Payne (2012). Transparent Garnet Detection Scintillators for Gamma-ray Detection. *Proc. SPIE 8507, Hard X-Ray, Gamma-Ray and Neutron Detector Physics XIV*, **857017**, pp. 1–8.

Wernick, M. N. and J. N. Aarsvold (eds.) (2004). *Emission Tomography - The Fundamentals of PET and SPECT*. Elsevier Academic Press.

Wikipedia (2006). Bayer filter. `http://en.wikipedia.org/wiki/Bayer_filter`.

Wikipedia (2007). Foveon X3 sensor. `https://en.wikipedia.org/wiki/Foveon_X3_sensor`.

Wootton, R., N. G. Patil, R. E. Scott, and K. Ho (eds.) (2009). *Telehealth in the Developing World*. Royal Society of Medicine Press Ltd.

Yan, X. H. and R. M. Leahy (1992). Cone beam tomography with circular, elliptic and spiral orbits. *Phys. Med. Biol.*, **37**, pp. 493–506.

Yang, K., A. L. Kwan, D. F. Miller, and J. M. Boone (2006). A geometric calibration method for cone beam CT systems. *Med. Phys.*, **33(6)**, pp. 1695–1706.

Yu, H., C. Ji, and G. Wang (2011). SART-Type image reconstruction from overlapped projections. *Int. J. Biomed. Imaging*, pp. 1–7.

Zhou, Z., F. Gao, H. Zhao, and L. Zhang (2011). Techniques to improve the accuracy of noise power spectrum measurements in digital x-ray imaging based on background trends removal. *Med. Phys.*, **38(3)**, pp. 1600–1610.